Influence of cloudy/clear-sky partitions, aerosols and geometry on the recent variability of surface solar irradiance's components in northern France

Gabriel Chesnoiu[1], Nicolas Ferlay[1], Isabelle Chiapello[1], Frédérique Auriol[1], Diane Catalfamo[1], Mathieu Compiègne[2], Thierry Elias[2], and Isabelle Jankowiak[1]

[1]Université de Lille, CNRS, UMR 8518 - LOA, Lille F-59000, France
[2]HYGEOS, Euratechnologies, Avenue de Bretagne, 59000 Lille, France

Correspondence: Nicolas Ferlay (nicolas.ferlay@univ-lille.fr)

Abstract. The surface solar irradiance (SSI) is a fundamental parameter whose components (direct and diffuse) and variabilities are highly influenced by changes in atmospheric content and scene's parameters. The respective importance of cloudy sky conditions and atmospheric aerosols on SSI evolutions is region dependent and only partially quantified. Here we provide a comprehensive analysis of SSI variabilities recorded in northern France, a region with extensive variabilities of sky conditions and aerosol loads. Through the application of automatic filtering methods on 1 min resolution SSI ground-based measurements over Lille, sky conditions are classified as clear-sky, 11 %, clear-sun-with-cloud, 22 %, and cloudy-sun situations, 67 %, over 2010 to 2022, for which we analyze the statistics and variabilities of the global horizontal (GHI), direct (BHI) and diffuse (DHI) solar irradiances. Coincident photometric measurements of aerosol properties and radiative transfer simulations provide the mean to conduct a multivariate analysis of the SSI observed trends and year-to-year evolutions, and to estimate aerosol and cloud forcings under clear-sun conditions. The analysis of the record value of all-sky GHI in spring 2020 attributes 89 % of the changes to the exceptional sunlight conditions (57 % of clear-sun situations). It highlights also for that season the importance of solar zenithal angle's changes whose positive effect on clear-sun conditions surpasses those due to aerosols. Our results show all-sky GHI and BHI positive trends of around +4.0 and +4.4 W/m^2/year respectively, both in spring and summer, that are explained at more than 60 % by an increase of clear-sun occurrences of +1 % per year. Additional significant BHI~~'s~~ increases under clear-sun conditions are mainly explained in spring by the negative trend in aerosol optical depth (-0.011 per year), and partly by angular effects in summer. Moreover, we find that clear-sun with cloud situations are frequently marked by irradiance enhancement due to clouds, with on monthly-average 13 % more GHI and 10 % additional diffuse proportion than in clear-sky situations. Under such conditions, clouds add on average 25 W/m^2 of diffuse irradiance that set the GHI~~amount of solar irradiance~~ at the remarkable level of pristine (aerosol and cloud free) conditions, or even higher by more than +10 W/m^2 in summer and for low aerosol loads. Overall, our results highlight the dominant and complex influence of cloudy conditions on SSI, which precedes or combines with that of aerosols and geometrical effects, and leads to remarkable global level of SSI in clear-sun with-clouds situations.

1 Introduction

The amount of solar energy that reaches the Earth's surface plays a critical role in the Earth's energy balance and governs a wide range of key physical processes, including evaporation and associated hydrological components, snow and glacier melt, plant photosynthesis and related terrestrial carbon uptake, as well as the diurnal and seasonal course of surface temperatures. Furthermore, the amount of solar irradiance incident at the surface (SSI) has significant implications for solar energy production technologies and agricultural productivity.

Studies conducted in recent decades, both through observations and modeling, suggest that surface solar radiation is not necessarily constant on a decadal time scale. Instead, it exhibits significant decadal variations with a worldwide decreasing (dimming) trend until the 1990^{s}, followed by an increasing (brightening) trend from then onwards (Wild et al., 2005; Wild, 2009; Liepert, 2002; Norris and Wild, 2007).

Determining the cause of the observed trends in SSI has proven to be a challenging task. However, an increasing number of studies indicate that the aerosol-radiation interaction is likely responsible for an increase in all-sky radiation since 1985 (Philipona et al., 2009; Manara et al., 2016; Ruckstuhl et al., 2008; Wild et al., 2021). It should be noted that the timing and intensity of the minimum cannot be accurately simulated using current aerosol emission inventories, as reported by Liepert and Tegen (2002); Romanou et al. (2007); Ruckstuhl and Norris (2009); Turnock et al. (2015). This is due to the high temporal and spatial variability of clouds and aerosols, which is particularly difficult to represent in models.

Regional studies that record changes in surface radiation while taking into account atmospheric parameters that can impact such changes are crucial, as they provide more insight on the relationship between the variations of these parameters and the changes in surface radiation. A few studies were recently conducted in the Benelux region, especially over the Netherlands (Boers et al., 2017, 2019; Heerwaarden et al., 2021), and over larger European areas (Pfeifroth et al., 2018; Schwarz et al., 2020) characterized by substantial proportions of clouds (Hahn and Warren, 2007), as well as a high population density, which results in elevated levels of atmospheric particulate pollution. Most of these studies have so far primarily focused on the analysis of the impact of clouds and aerosols on the evolution of the global surface solar radiation ~~trends~~, and did not consider the variability of the direct and diffuse components. However, depending on their optical properties, aerosols and clouds influence incident radiation by reducing the direct component while enhancing the diffuse component. Although the impact on photovoltaic production depends mainly on the total amount of solar irradiation reaching the surface, the performances of all solar conversion systems~~technologies~~ are also sensitive to the partition between diffuse and direct components (Kirn et al., 2015; Lindsay et al., 2020; Sengupta et al., 2021).

The study of incident direct and diffuse radiations is particularly important in the context of climate change as significant changes in the composition of the atmosphere are expected by the end of the century, with varying magnitudes depending on the corresponding SSP (Shared Socioeconomic Pathways) and RCP (Representative Concentration Pathway) scenario (Moss et al., 2010; Hauglustaine et al., 2014; Drugé et al., 2021), leading to potentially very different solar environments. Moreover, it is now established that mitigating the impact of greenhouse gas emissions on climate change requires the development of alternative methods of energy production. Currently, photovoltaic technologies represent one of the most important and

promising technologies, in addition to energy produced by wind turbines. Several studies have investigated the future resilience of renewable installations (Tobin et al., 2018), especially photovoltaic ones (Gutiérrez et al., 2020; Hou et al., 2021; Jerez et al., 2015). These studies show that the future evolution of the solar environment and of the surface temperature, will have a significant impact on the future development of these technologies and their production.

In the current study, we analyze the variability of the global surface solar irradiance and its direct and diffuse components in northern France over the years 2010-2022 as measured at the ATOLL (ATmospheric Observations in LiLle) platform, as well as the variability of coincident sub-hourly measurements of aerosol optical properties. Our analysis relies, in particular, on the development of a classification of the sky conditions based on automated processing of irradiance measurements by cloud filters and identification of aerosol's class. Beside obtaining climatologies at our site, our objective is to disentangle and quantify the influence of the different parameters that contribute to year-to-year irradiance variabilities observed in Lille over the period 2010-2022. These classifications allow us to distinguish the influence of the occurrence of cloudy and clear-sky situations from the influence of the atmospheric content (aerosols and gases) and other parameters, such as the solar zenith angle, on the variability of the SSI and its direct and diffuse components. The effect of atmospheric parameter's variability is quantified with radiative transfer simulations in clear-sky conditions.

Section 2 provides a brief overview of the data and methods used to identify cloudy and clear sky moments. A classification of the aerosol content based on the optical properties measured coincidentally as part of the AERONET network is also introduced. The aim of this classification is two-fold. On the one hand, it enables a more precise characterization of the radiative impact of aerosols observed in Lille through the definition of new models of aerosol optical properties which are used to perform simulations using the radiative transfer code SOLARTDECO. On the other hand, it facilitates the study of the variability of the aerosol content in Lille. In particular, used in tandem with the classification of the sky conditions and radiative transfer~~SOLARTDECO~~ simulations it enables the quantification of the contribution of the different atmospheric and geometric parameters to the variability of the surface solar irradiance over the period 2010-2022, as described in Section 3. An analysis of the ~~direct~~ radiative effect of ~~atmospheric particles,~~ aerosols and clouds on the downwelling solar radiation at the surface~~,~~ over 2010-2022 is also presented in Section 4, with the objective of quantifying the mean aerosol non-net direct radiative effect in clear-sky conditions and analyzing the combined effects of aerosols and clouds under irradiance enhancement conditions (Pecenak et al., 2016)~~for various sky conditions~~. Finally, Section 5 synthesizes the results of our study~~provides the concluding remarks~~ and outlines the possible directions for future works.

2 Data and methods

In this section, the measurement datasets, algorithms and methods used in this study are described. Information on the data availability is given separately at the end of the article.

2.1 Ground-based measurements from the ATOLL platform

2.1.1 Description of the site

This study relies on the coincident aerosol optical properties and surface solar irradiance measurements routinely performed at the ATOLL platform located in the North of France (50.61°N, 3.14°E, 70 m a.s.l), 6 km southeast of Lille downtown area, on the rooftop of a building of the University of Lille in Villeneuve d'Ascq. As the metropolitan area of Lille is characterized by a high population density and more than 1.1 million inhabitants, the ATOLL site can be considered as suburban. As shows Figure 1, with the Belgian border at a distance of roughly 15km, the site is located very close to the Benelux region, one of the most densely urbanized and industrialized area of northwestern Europe. It is thus influenced by many anthropogenic emission sources, both regional and trans-boundary, with strong contributions from the residential and industrial sectors, as well as transport and agriculture, which contribute to relatively frequent particulate pollution episodes (Potier et al., 2019; Favez et al., 2021; Velazquez-Garcia et al., 2023). It should be noted that the site is also subject to a significant maritime influence due to its proximity with the English Channel and the North Sea~~, located less than 80 km away~~. According to the Köppen-Geiger climate classification (Beck et al., 2018) the climate is described as Cfb, meaning it is mostly temperate (C) with a warm summer (b) and an absence of dry season (f). The typical precipitation's amount is of about 600 to 800 mm/yr and is related to a relatively high frequency of clouds throughout the year with average cloud fraction values ranging between 60 to 80% depending on the time of year (Warren et al., 2007).

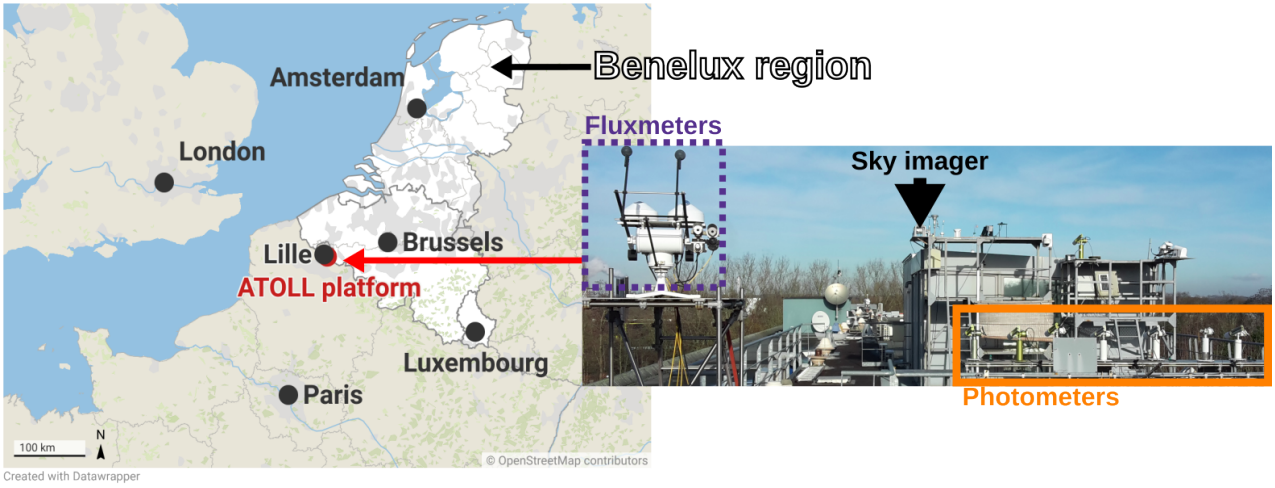

Figure 1. This figure was modified to reduce superfluous information and size. The copyright statement was added. Map representing the location of the ATOLL platform (red marker). The white area represents the Benelux region~~ and the black hatches the English Channel~~. Adjacent to the map is a picture of the platform including the main instruments used in this study, i.e. the set of pyronameter and pyrheliometer on a Sun-tracking device (purple box), the AERONET sunphotometers (orange box) and the sky imager (black arrow). Map created with Datawrapper. ©OpenStreetMap contributors 2024. Distributed under the Open Data Commons Open Database License (ODbL) v1.0.

2.1.2 SSIIrradiance measurements

A Kipp & Zonen CHP1 pyrheliometer, mounted on a sun-tracking device, measures the Direct (or beam) Normal Irradiance (DNI) incident at the surface in the direction of the Sun with a field of view of 5±0.2°. The Beam Horizontal Irradiance (BHI) is then derived from these measurements using the cosine of the solar zenith angle ($\mu_0 = \cos(\mathrm{SZA})$) as $\mathrm{BHI} = \mathrm{DNI} \times \mu_0$. In addition to the pyrheliometer, a Kipp & Zonen CMP22 pyranometer is also placed on the sun-tracker. The pyranometer is paired with a shading sphere that blocks the incoming direct irradiance, allowing for coincident measurements of the Diffuse Horizontal Irradiance (DHI). The Global Horizontal Irradiance (GHI) is then computed as the sum of the BHI and DHI. Such a procedure has the advantage of reducing cosine errors at low sun angles compared to measurements obtained with a single pyranometer (Michalsky et al., 1999). Both instruments measure radiation in the broadband range between 200-3600 nm for the CMP22, and 200 to 4000 nm for the CHP1~~210 and 3600 nm covering most of the solar spectrum (200 - 4000 nm)~~. Therefore, we have access to instantaneous measurements (50 ms) of the incoming surface solar irradiance and its direct and diffuse components on an horizontal plane sampled at a 1-minute time resolution since February 2009. To guarantee the smooth operation of the system, regular maintenance is performed, including daily cleanings. Moreover, both instruments were calibrated in 2012, 2017, and 2022 and new calibration factors were applied after each calibration, with differences in calibration factors lower than 3%.~~and their sensitivities have remained relatively stable throughout the period.~~ Under such operational conditions, the uncertainties in the measurements are expected to be of the order of 2 to 3% for the GHI and DHI, and 1.5% for the BHI, as typically reported in the literature (Derimian et al., 2008, 2012; Vuilleumier et al., 2014; Wild et al., 2021). It is worth noting that there are some missing values in the measurement series for winter months of several years, particularly in January and February. This gap occurs because the instruments are~~were~~ regularly sent either in M'Bour (Senegal), for calibration of local instruments, or in Delft (Netherlands), for a recalibration by the manufacturer.

2.1.3 Aerosol measurements

A CIMEL sun/sky photometer from the PHOTONS (PHOtométrie pour le Traitement Opérationnel de Normalisation Satellitaire) network, which is the French part of AERONET (Aerosol Robotic Network) (Holben et al., 2001) is used to characterize and monitor aerosol optical and columnar microphysical properties in Lille. The photometer provides direct measurements of the Aerosol Optical Depth (AOD) at six different wavelengths (340, 380, 440, 500, 870 and 1020 nm) along with their corresponding Angström Exponents (AE). In addition, Precipitable Water Vapor content (PWV in cm) is derived from measurements at 940 nm. AERONET almucantar inversions (Dubovik and King, 2000; Dubovik et al., 2002) of aerosol size distribution, complex refractive index (m = n + ik), and single scattering albedo (SSA) were also used in this study. However, as it requires a relatively important optical air mass (SZA > 50°) and a perfectly cloudless sky, the amount of available inversions is small (less than 500 data points). Their climatological weight is thus relatively limited. Therefore, they have been mainly used to compute site-specific aerosol optical properties through Mie calculations, as described in Section 2.3.1. In this study, mostly level 2.0 (cloud-screened and quality controlled) data has been used, except for the measurements from September to December 2022, for which only level 1.5 (cloud-screened only) data was~~were~~ available at the time of writing. The uncertainty in measured

AOD is estimated to be of approximately 0.02 for the UV channels (340 and 380 nm) and 0.01 otherwise (Giles et al., 2019). The reported uncertainty in the PWV measurements is around 10-15 % (Pérez-Ramírez et al., 2014; Smirnov et al., 2004), with a dry-bias of around 5-6 % (Pérez-Ramírez et al., 2014). The retrieval of complex refractive index and volume size distribution is a challenging task, and the associated uncertainties are highly variable depending on the observing conditions. For example, the uncertainty in the volume size distribution ranges from 15 to 100 %, depending on the size of the particles, while for the imaginary part of the refractive index (k), it varies between 30 and 50 % for strongly and weakly absorbing aerosols, respectively (Dubovik et al., 2000; Dubovik and King, 2000; Nakajima et al., 1983, 1996).

2.1.4 Coincidence of aerosol and SSI~~irradiance~~ measurements

For this study, we chose to analyze the period from 2010 to 2022, as it represents the longest period of continuous coincident aerosol and irradiance measurements available. The number of coincident data points is mainly determined by the frequency of AERONET direct observations. In the absence of clouds in the direction of the Sun~~Prior to 2016~~, the standard time resolution of the photometric measurements was 15 minutes prior to 2016, and~~which~~ was later increased to 3 minutes due to a change in the instrument's model. ~~This temporal resolution can be considered a maximum, as it is often reduced by the presence of clouds in the direction of the Sun.~~ Overall, t~~T~~he complete dataset of synchronous aerosol and irradiance measurements comprises approximately 82 000 coincident observations in clear-sun conditions.

2.1.5 Other measurements

In addition to aerosol optical properties and irradiance measurements, other coincidental observations from the ATOLL platform have been used. Notably, sky images captured by a sky-imager (CMS Schreder VIS-J1006) since 2009, with a time resolution of 3 minutes, have been visually examined to assess the cloud cover state over short periods of time. This manual evaluation of the sky images helped validate more systematic cloud-screening methods based on irradiance measurements, as described in Section 2.2.1. Meteorological observations of relative humidity (RH)~~,wind speed, and wind direction~~ have also been used to perform simulations of the surface solar irradiance in clear-sky conditions, as described in Section 2.3.1, while wind speed, and wind direction measurements were used ~~and~~to complete the climatological study of the aerosol content and irradiance measurements in Section 3.1~~, as described in Sections 2.3.1 and 3.1~~.

2.2 Classification of atmospheric conditions in Lille~~Classification of the sky conditions over Lille~~

2.2.1 Sky conditions

The presence of clouds, in and off the sun's direction, leads to situations with contrasting levels and characteristics of SSI, for which the sensivity to atmospheric conditions varies widely. Most notably, the sensitivity of the SSI to aerosol properties is low when clouds are present, aside from some exceptions characterized by thin cirrus or isolated clouds. In order to describe and study the variabilities of the SSI, and to analyze differences in its characteristics between different periods or identify the origin of observed temporal trends, we chose to divide sky conditions between three possible categories with contrasted levels

of irradiance: clear-sky (CSKY), i.e. no clouds in the sky; clear-sun with clouds (CSWC), i.e. presence of clouds but not in the Sun's direction; and cloudy-sun (CLOS) situations. The first two categories are characterized by high levels of surface solar irradiance and its direct component, but they differ in their diffuse contributions. In contrast, the third situation is characterized by much lower levels of SSI with a predominant contribution from diffuse radiation. Although AERONET measurements are cloud cleared, they only allow the distinction between clear-sun and cloudy-sun moments. Additionally, their time resolution is lower than that of our irradiance measurements. Therefore, two cloud-screening methods based on the available 1-minute irradiance measurements were selected from the literature. The method of Batlles et al. (2000) is used to distinguish clear-sun moments from cloudy-sun situations, while a revised method of the algorithm of García et al. (2014) is used to isolate clear skies (no clouds, i.e. CSKY) from situations with clouds. These two binary distinctions allow for the intended classification of the sky conditions into three categories: CLOS, CSKY and CSWC. Both methods were evaluated in Gueymard et al. (2019) and were found to perform particularly well for these distinctions on a 1-minute basis. Moreover, the method of García et al. (2014) relies on the popular detection scheme developed by Long and Ackerman (2000), and does not require parallel clear-sky simulations. It also relies on collocated AOD information, which should improve the detection of clear skies under higher aerosol loads compared to the initial method of Long and Ackerman (2000). Both methods used in this study are described in more details in Appendix A.~~To analyze the variability of surface solar irradiance and understand its underlying causes, it is necessary to first assess the sky conditions. Indeed, the presence of clouds, particularly in the direction of the Sun, leads to situations with very contrasting levels and characteristics of surface solar irradiance. The aim is thus to distinguish these different situations in order to adapt the analysis of the sensitivity of the surface solar irradiance. Clear-sun (CSUN) situations, when the Sun is visible with (clear-sun with clouds, CSWC) or without (clear-sky, CSKY) clouds in the sky, are characterized by high levels of surface solar irradiance with a predominant contribution of the direct component. They are more sensitive to the aerosol content than cloudy-sun (CLOS) situations, i.e. when the Sun is masked by clouds, for which the sensitivity of the SSI to the aerosol content can be considered negligible aside from a few exceptions characterized by thin cirrus or isolated clouds. As only AERONET level 1.5 data or more is used in this study, some knowledge is already available on the state of the cloud cover as these datasets are automatically cloud cleared through the study of the variability of triplets of photometric measurements. However, there are some drawbacks. On the one hand, this method exclusively detects the presence of clouds in the direction of the Sun which means that it only distinguishes clear-sun moments from cloudy-sun moments. Thus, in clear-sun with clouds conditions, the effect of residual clouds on the diffuse and global irradiances cannot be distinguished from that of aerosols. On the other hand, as the time resolution of the photometric measurements is lower than that available for irradiance measurements, it is less relevant for the intended climatological study. Hence two cloud-screening methods based on the available 1-minute irradiance measurements were selected for this study based on the performance analysis of Gueymard et al. (2019). The method of Long and Ackerman (2000) is used to distinguish clear-sun moments from cloudy-sun situations, while the algorithm of García et al. (2014) isolates clear skies (no clouds, i.e. CSKY) from cloudy situations (CSWC and CLOS). This allows for the classification of the sky conditions in three distinct categories (cloudy-sun, clear-sun with clouds, and clear-sky) with contrasting levels of irradiance as described in Section 3.1.~~

Section 2.2.1 was moved to the Appendices.

~~Finally, for the sake of simplification, in what follows, the method of García et al. (2014) will be labelled simply as «clear-sky» (CSKY) and the method of Batlles et al. (2000) as «clear-sun» (CSUN). Furthermore, situations qualified as CSUN but not CSKY will be referred to as CSWC (clear-sun with clouds) as they should correspond to moments when the sky is (partially) cloudy without clouds in the Sun aureole.~~

In the present study, ~~To validate~~ the performances of the cloud-screening methods have been evaluated, by ~~,a~~ comparison ~~was made~~ with ground observations of the sky conditions based on the manual inspection of coincident sky images from ATOLL at a 3-minute time resolution for the months of January and May 2018. The~~se~~ images were individually analyzed to determine the presence or absence of clouds in the sky and in the vicinity of the Sun. In the latter case, the assessment of clouds in the direction of the Sun was purposefully strict in order to account for the rather large field of view of the pyrheliometer (5°), which is larger than the Sun's viewing angle (0.5°). The potential motion of clouds in or out of the pyrheliometer's field of view was also considered to account for any time delay between the irradiance measurements and the sky images. Since the output of both manual and irradiance-based estimates is binary, i.e. clear or cloudy, there are only four possible outcomes. This allows the definition of a confusion matrix as follows :

- True Positive (TP), the sky (Sun) is clear in both manual and filter-based estimates,
- True Negative (TN), the sky (Sun) is correctly identified as cloudy,
- False Positive (FP), the sky (Sun) is identified as clear by the cloud-screening method but~~while it~~ is manually assessed as cloudy,
- False Negative (FN), the sky (Sun) is wrongly assessed as cloudy by the algorithm.

The results are presented in Table 1 for both clear-sun and clear-sky conditions simultaneously. For the clear-sky detection, the revised method of García et al. (2014) gives satisfying results with a low FP score (2.7%) compared to the TP score (12.5%) which leads to an overall good precision ($\frac{TP}{TP+FP}$) of 82%. The latter score highlights that 82% of the time the sky is correctly identified as clear by the algorithm. This method also presents a relatively low FN score (2.6%), suggesting that it is also able to accurately isolate cloudy moments (either CSWC or CLOS). This leads to overall satisfactory performances for the distinction of clear-sky and cloudy conditions, with a risk ($\frac{FP+FN}{FP+FN+TP+TN}$) of only 5% to misidentify sky conditions.~~For the clear-sky detection, the revised method of García et al. (2014) gives satisfying results with a very low FP score (2.7%) compared to the TP score (12.5%) which leads to an overall good precision of 82%. The latter score highlights that 82% of the time the sky is correctly identified as clear by the algorithm. The risk is also quite low as the identification of the sky condition only fails 5% of the time. For the identification of clear-sun conditions the results are also satisfactory although the method of Batlles et al. (2000) is less successful with a relatively high FP score (10.9%) compared to the TP score (21.8%). The precision is thus lower (67%) and the risk higher (12%) which might lead to a slight overestimation of the proportion of clear-sun situations.~~

For the identification of clear-sun conditions, the method of Batlles et al. (2000) produces satisfactory but less optimal results. The method shows a strong ability in identifying cloudy-sun moments (FN score of 0.8%) and shows an overall satisfactory risk of only 12% for the distinction between clear-sun and cloudy-sun conditions. However, its FP and TP scores are closer

		TP	TN	FN	FP	Precision	Risk
	Definition	Filter → Clear Obs → Clear	Filter → Cloudy Obs → Cloudy	Filter → Cloudy Obs → Clear	Filter → Clear Obs → Cloudy	$\frac{TP}{TP+FP}$	$\frac{FP+FN}{FP+FN+TP+TN}$
Clear-sky (Garcia)	Nb of cases	1549 (12.5%)	10186 (82.1%)	328 (2.6%)	340 (2.7%)	82%	5%
Clear-sun (Batlles)	(% of cases)	2702 (21.8%)	8247 (66.5%)	98 (0.8%)	1356 (10.9%)	67%	12%

Table 1. Confusion matrix for the estimation of the sky conditions between SSI~~irradiance~~ based filters and manual ground observations from sky images for January and May 2018 in Lille.

compared to the Garcia method and thus its precision in correctly identifying clear-sun conditions is lower (67%), which might lead to a slight overestimation of the proportion of clear-sun situations. Nonetheless, further analysis indicates that the Batlles FP cases are often due to the presence of cloud edges or clouds of low atmospheric optical depth in the Sun's direction, such as Cirrus scenes or small isolated clouds, and that most of the time, 1352 out of 1356 FP cases, DNI values are greater than 120 W/m^2. These FP cases, while not clear-sun cases, are thus almost entirely sunny moments (sunshine threshold defined by the WMO) and can be considered as quasi clear-sun. In addition, a similar analysis of the performances of the AERONET cloud-screening method over January and May 2018 further comforts the results of the Batlles method, as it highlights comparable performances in distinguishing clear-sun and cloudy-sun conditions, with a satisfactory risk of 13%.

It should be noted that both methods perform quite well under almost any aerosol load. Both algorithms properly transcribe the global probability density function (PDF) of AOD_{440} over 2010 - 2022 as from the unfiltered AERONET observations. Comparisons were~~was~~ made with the initial algorithm of Long and Ackerman (2000). The overall precision of this method is higher (90%) in link with a much lower FP score (1.0%). However, the corresponding AOD probability density function suggests that this algorithm is less representative of the variability of the aerosol content in Lille, as it tends to misidentify clear skies for AOD values greater than 0.3.

Finally, note that irradiance measurements considered in this study were limited to times between sunrise + 30 minutes and sunset - 30 minutes in order to reduce the bias observed in Long and Ackerman (2000) for large solar zenith angles as such situations tend to be systematically classified as cloudy by the algorithm. This limitation was chosen to eliminate as many measurements in winter as in summer, which would not have been the case for a criterion based on the solar zenith angle. For the sake of simplification, in what follows, the method of García et al. (2014) will be labelled simply as «clear-sky» (CSKY) and the method of Batlles et al. (2000) as «clear-sun» (CSUN). Furthermore, situations qualified as CSUN but not CSKY will be referred to as CSWC (clear-sun with clouds) as they should correspond to moments when the sky is (partially) cloudy without clouds in the Sun aureole.

2.2.2 Aerosol conditions

This section replaces Section 2.3.2.

The description of the classes, previously in the text, has been added to Table 2.

Figure 2 has been moved to the supplements.

Table 2b has been removed.

For the present study, in addition to the classification of sky conditions, a specific classification of aerosol optical properties, inspired by the work of Toledano et al. (2007), has been defined. The aim of this classification is twofold. On the one hand, it enables the definition of the new models of aerosol optical properties, which represent typical aerosol conditions encountered in Northern France, and can then be used for radiative transfer simulations as described in Section 2.3. On the other hand, it also serves a climatological purpose as it facilitates the characterization of the nature and variability of the aerosol content and type present in the Lille area over the period 2010 - 2022. This classification represents a rough categorization of the aerosols properties in Lille among 6 classes of measured AOD_{440} and $AE_{440-870}$. The definition of each class as well as the corresponding AOD_{440} and $AE_{440-870}$ thresholds and their respective proportions are summarized in Table 2. A graphical illustration of the classification is also available Figure S1 of the supplements, which represents the scatter plot of AOD_{440} against $AE_{440-870}$ for all AERONET level 2.0 measurements acquired in Lille from 2010 to 2022.

Class	Definition	$\mathbf{AOD_{440}}$	$\mathbf{AE_{440-870}}$	Proportion (%)
Continental	Mostly fine (anthropogenic) particles ($AE_{440-870} \geq 1$) with low to medium aerosol loads ($AOD_{440} < 0.21$)	$[0, 0.10[$ $[0, 0.21[$	$[1.00, 1.34[$ $[1.34, 2.10[$	38
Continental polluted	Same as continental with stronger AOD values ($0.21 \leq AOD_{440} < 0.85$)	$[0.21, 0.85[$	$[1.34, 2.30[$	20
Maritime	Mostly coarse particles ($AE_{440-870} < 1$) with low to medium aerosol loads ($AOD_{440} < 0.19$)	$[0, 0.19[$ $[0, 0.12[$ $[0, 0.1[$	$[-0.04, 0.17[$ $[0.17, 0.82[$ $[0.82, 1.00[$	14
Desert dust	Mainly coarse particles with higher AOD_{440} values than maritime aerosols ($AOD_{440} > 0.12$)	$[0.12, 2.4[$	$[0.17, 0.82[$	5
Mixed	Situations with important contributions of both fine and coarse particles	$[0.10, 0.85[$	$[0.82, 1.34[$	22
Strong event	Events characterized by very high AOD values ($AOD_{440} \geq 0.85$) and dominated by fine particles	$[0.85, 2.90[$	$[0.82, 2.30[$	0.3
Total number of associated photometric measurements in Lille over 2010-2022				95 923

Table 2. Definition of the aerosol classes in Lille and associated AOD_{440} and $AE_{440-870}$ thresholds. The last column of the table represents the respective proportion of each aerosol class measured in Lille over the period 2010-2022.

2.3 Radiative transfer simulations with SOLARTDECO

This section describes the SOLARTDECO radiative transfer code ~~and the related aerosol optical properties models~~used in this study. An evaluation~~validation~~, over the period 2010-2022, of SOLARTDECO radiative transfer simulations in clear-sky conditions is also presented in Section 2.3.2 to ensure their good transcription of the ~~direct~~ radiative effect of aerosols in Lille.

2.3.1 Description ~~of the SOLARTDECO code~~

The radiative transfer code SOLARTDECO is a "solar" version of ARTDECO (Atmospheric Radiative Transfer Database for Earth Climate Observation), a toolbox comprising data of the properties of atmospheric components as well as several radiative transfer models intended for the simulation of atmospheric radiances and radiative fluxes (Dubuisson et al., 2016). The scientific numerical core is written in Fortran90 while the configuration files and libraries are defined through python and ASCII formats. It is thus flexible and highly portable, hence its selection for this study. The overall operating scheme of SOLARTDECO described below is also represented Figure 2.

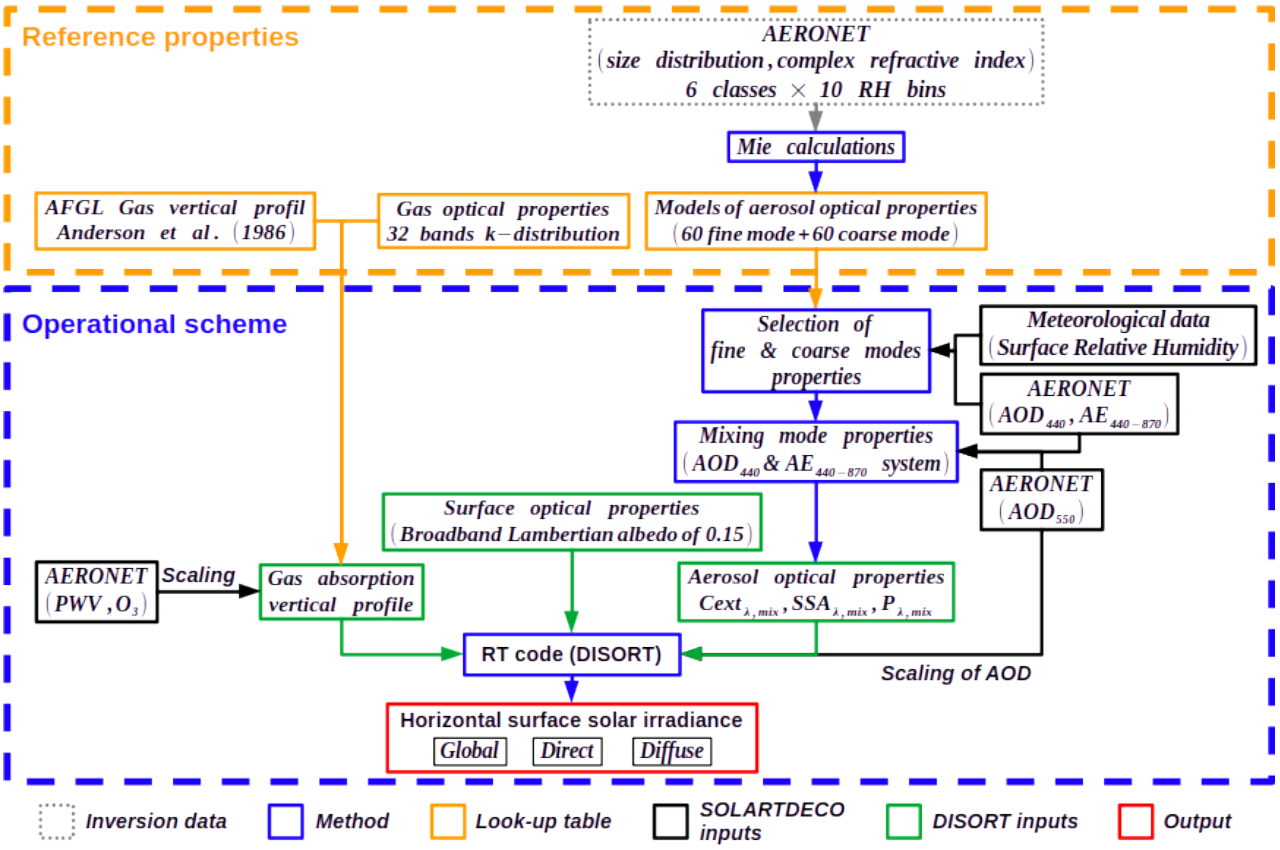

Figure 2. Schematic description of SOLARTDECO simulations.

Initially, ARTDECO wasis designed for radiative transfer simulations over the whole ultraviolet (UV) to thermal infrared (IR) range. It works for specific channels (monochromatic mode) as well as for more general spectra through the use of k-distributions (Lacis and Oinas, 1991). SOLARTDECO, on the other hand, is dedicated to the study of the incoming surface solar radiation in clear-sky conditions. The spectral resolution of the simulations iscan be defined using thetwo different k-distribution ofs initially implemented in ARTDECO. The first one was defined by Kato et al. (1999), which is composed of and has a relatively low resolution with only 32 spectral bands spanning the solar range (0.24 - 4.0 μm) and. It is well suited for the computation of spectrally integrated irradiances however its depiction of the spectral variability is somewhat limited. Therefore another k-distribution, with more than 200 spectral bands, is also available for refined spectral simulations (Dubuisson et al., 2004, 2005). ThisThese k-distributions isare coupled with the gas concentration vertical profiles from Anderson et al. (1986) for a mid-latitude summer to represent the gaseous absorption of the atmosphere. The profiles of O_3 and H_2O are scaled for each simulation with respect to the total ozone (Dobson units) and precipitable water vapor (cm) columnar contents available in the AERONET datasets. Note that SOLARTDECO also accounts for the absorption of CO_2 and O_2 with homogeneous concentrations of respectively 407 and 209 000 ppmv. In what follows and unless stated otherwise, the k-distribution from Kato et al. (1999) is used.

The description of the aerosol optical properties has been reworked and detailed.

The description of the mixing of aerosol fine and coarse modes has been moved to the appendices.

Regarding the absorption and scattering of solar radiation by aerosols, SOLARTDECO uses a look-up table of extinction coefficients ($Cext_\lambda$), single scattering albedo (SSA_λ) and components of the phase function (P_{11}, P_{21}, P_{34} and P_{44}), which are used as inputs for radiative transfer simulations. The idea is to limit time-consuming Mie calculations and to allow the definition of aerosol optical properties at a higher resolution than that of AERONET inversions, which are quite rare (less than 500 data points over 2010-2022) due to requirements regarding the optical air mass, AOD and need for a perfectly cloudless sky (Dubovik et al., 2002). This look-up table relies on the AOD_{440} and $AE_{440-870}$ classification defined in Section 2.2.2, as well as surface relative humidity measurements from ATOLL, which are used to split AERONET inversions of volume size distribution and refractive index into several subsets. Note that level 2.0 inversions were used for classes which present AOD values greater than 0.4 (i.e. Continental polluted, Desert dust, Strong events and Mixed), while level 1.5 data was used otherwise, provided that apart from the AOD threshold, all the other criteria were met. For each subset of the look-up table, the size distribution is divided between two modes (fine or coarse). Then, datasets of $Cext_\lambda$, SSA_λ and phase function components are computed for each mode through Mie calculations, based on the normalized mean number size distributions (i.e. number size distribution of each mode divided by the corresponding number concentration) and the total mean complex refractive index. Overall, the look-up table includes 120 datasets, divided between the two modes, six classes and ten relative humidity bins. These datasets are used to compute the total aerosol optical properties needed for each radiative transfer simulation at the resolution of AERONET direct-sun measurements by mixing the pre-computed properties of the fine and coarse modes selected based on AOD_{440}, $AE_{440-870}$ and surface relative humidity measurements. The methodology adopted in the present study to compute the total aerosol optical properties is described in details in Appendix B. It involves solving a system of two equations with two unknowns, for each simulation, based on the measured values of AOD_{440} and $AE_{440-870}$ with the

additional use of AOD_{550} data. The two coefficients derived from this system are then used, jointly with the mean number concentrations of the fine and coarse modes derived from AERONET size distributions, to mix the pre-computed optical properties of the two modes specifically for each simulation. It is worth mentioning that the chosen system of two equations with two unknowns involving AOD_{440} and $AE_{440-870}$ measurements was chosen as it shares inputs with the look-up table of aerosol optical properties. Furthermore, proxy simulations were also conducted with another parameterization, based on a more common system involving the measured AOD_{440} and AOD_{870}. Comparisons with ground-based measurements, similar to those presented for the chosen system in the following section, show very comparable results (Figure S2). Note that following the mixing of the two modes, the total columnar aerosol extinction for the simulation is scaled using the corresponding measured AERONET $AOD_{550,meas}$ as follows:

$$AOD_{\lambda,mix} = AOD_{550,meas} \times \frac{Cext_{\lambda,mix}}{Cext_{550,mix}} \quad (1)$$

where $AOD_{\lambda,mix}$ represents the total columnar aerosol optical depth at wavelength λ used for the simulation and $Cext_{\lambda,mix}$ the new extinction coefficients computed by mixing the corresponding fine and coarse modes. Although, this equation only represents the total columnar AOD, i.e. from the surface to the top of the atmosphere, AOD at other altitudes can be derived given the vertical profile of the aerosol layer. In this study, the aerosol layer was defined as an exponential decay of the aerosol density with a 2 km scale height (i.e. $AOD_{\lambda,mix}(z) = AOD_{\lambda,mix} \times e^{-z/2}$, with z the altitude in km). As only surface solar irradiance outputs were analyzed in this study, our results do not greatly depend on the vertical profile of the aerosol layer.

Finally, t~~T~~he remaining inputs of SOLARTDECO include the solar zenith angle and surface optical properties. For simplicity, this study assumes a~~as well as AOD_{440} and AOD_{550}, the $AE_{440-870}$ and the relative humidity at the ground level. This allows the determination of the geometry of the simulations and corresponding aerosol optical properties. For the present study, new models of aerosol optical properties were defined, for all k-distribution bands, using the available AERONET inversions of the aerosol volume size distribution and complex refractive index in Lille over the period 2010 - 2020. For each radiative transfer simulation a particular model is chosen and its properties adjusted relative to the inputs of AOD_{440}, AOD_{550}, $AE_{440-870}$ and RH as described in the following Section 2.3.2. SOLARTDECO also accounts for reflections at the surface which is defined as~~ lambertian surface with a spectrally homogeneous albedo arbitrarily set at 0.15~~in the present study~~. The aforementioned properties of the atmosphere (gaseous absorption and~~,~~ aerosol extinction) and surface reflectivity~~)~~ then allow for computations of the incoming and outgoing spectral solar irradiances in clear-sky conditions between the top of the atmosphere and the surface through the use of the radiative transfer model DISORT (Tsay et al., 2000). ~~Finally, although the present study focuses on the analysis of the horizontal irradiances, SOLARTDECO can also compute radiance fields for specific viewing geometries by providing viewing zenith and azimuth angles as additional inputs. Hence, it is possible to simulate the solar irradiances over titled surfaces for any orientation. This is of particular interest for solar related technologies which are usually placed on sun-tracking devices or present specific tilts and orientations to maximize their output.~~

2.3.2 Validation of SSI~~SOLARTDECO irradiance~~ simulations over 2010 - 2022

Figures 3a-c represent the scatter plots between SOLARTDECO simulations and measurements of (a) GHI, (b) BHI and (c) DHI over the period 2010-2022 in Lille for all AERONET observations performed between sunrise plus 30 minutes and sunset minus 30 minutes in clear-sky situations over the period 2010-2022 (44 239 comparisons). The identification of clear-sky situations is issued from the algorithm presented in Section 2.2.1. Simulated and measured mean flux values and associated standard deviations are plotted on the axes. Comparison statistics such as the mean bias (MBD), mean absolute bias (MAD), root mean square error (RMSD) are also shown on each figure in a beige box.

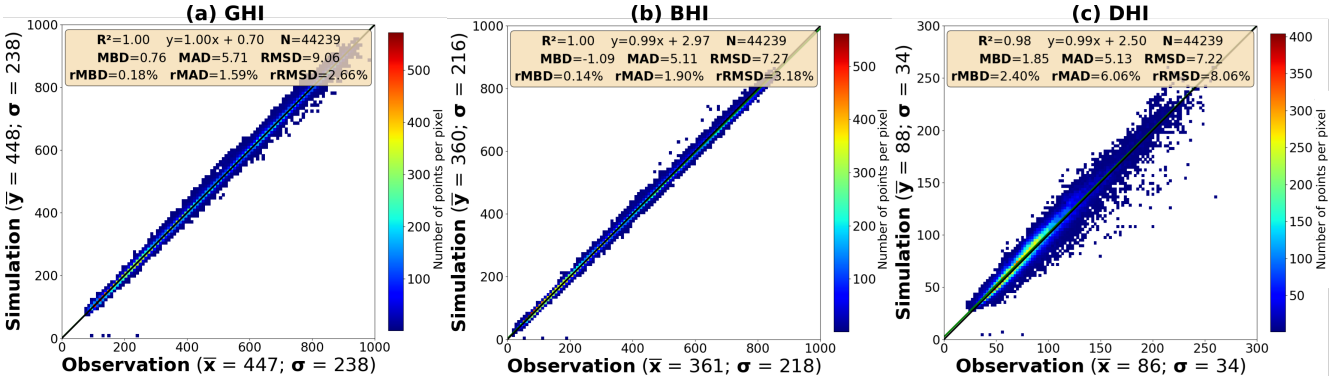

Figure 3. Scatter plot of SOLARTDECO simulations, based on level 2.0 AERONET inputs, against corresponding measurements of (a) GHI, (b) BHI and (c) DHI performed in Lille over the period 2010-2022. The black line represents the 1:1 line. Mean SSI~~irradiance~~ values and associated standard deviations are shown for both simulations and observations on their respective axes. Absolute and relative values of MBD (Mean Bias Difference), MAD (Mean Absolute difference) and RMSD (Root Mean Square Difference) are also displayed in the beige box included in the different figures. Only observations that coincide with clear-sky flux measurements (identified by the algorithm presented in Section 2.2.1) and performed between sunrise plus 30 minutes and sunset minus 30 minutes are considered for these comparisons.

Overall, the performances of SOLARTDECO simulations are satisfactory for all irradiance components with RMSD values lower than 10% for the DHI (8.06%) and 5% for the BHI (3.18%) and GHI (2.66%), which are comparable to the results of the best performing clear-sky irradiance models assessed in the latest studies of Sun et al. (2019) for the GHI and Sun et al. (2021) for the BHI and DHI. Note however that Sun et al. (2019, 2021) validations were obtained using reanalysis atmospheric data from MERRA2 (instead of AERONET here) and based on a larger number of worldwide stations of ground-based irradiance observations. Moreover, the performances of SOLARTDECO are well within the error margins expected for network-operational instruments (Meteorological Organization, 2008) as ~~the~~ mean absolute differences (MAD) are close to the resolution of network instruments (5~~lower than 3~~ W/m^2) for all irradiance components and more than 95% of the comparisons have mean ~~an absolute~~ differences lower than $\pm$20 W/m^2.

A focus on the years 2018 and 2019 shows that the performances of SOLARTDECO are also comparable to those of the radiative transfer tool SOLARES under clear-sky conditions (also identified using the modified Garcia algorithm~~identified using~~

~~the same filter as in the present study~~) in Lille over the same period (Elias et al., 2024)~~, which shows relative mean biases in GHI/BHI/DHI of -0.08/-0.41/+3.34% (compared with 0.18/0.14/2.40% for SOLARTDECO) and relative RMSD values of 1.83/2.29/8.01%~~.

However, SOLARTDECO does appear~~s~~ to slightly overestimate the DHI. This discrepancy could be linked to the circumsolar contribution, i.e. the diffuse part of the incident solar irradiance located in the vicinity of the Sun direction (0.6° to 8°). Indeed, the circumsolar contribution is measured by the instruments as part of the direct irradiance incident at the surface, while it is generally accounted for as part of the diffuse irradiance in radiative transfer simulations. This difference between simulations and ground measurements, which represents at most 2 to 3% of the DNI in the majority of cloud-free events (Gueymard, 2001, 2010; Blanc et al., 2014), usually leads to an underestimation of the BHI and overestimation of the DHI in radiative transfer simulations. This is in accordance with the overestimation of the diffuse irradiance by SOLARTDECO. However, no underestimation of the BHI is reflected by the mean biases, which could indicate the existence of other biases with opposite effects.

~~Most comparisons (94%) of the GHI show relative biases of less than 5% in absolute terms, in line with the relatively low RMSD values presented in Figures 3a-c. Thus, overall, we can consider that SOLARTDECO simulations are satisfactory and that the aerosol optical property models used for these simulations effectively capture the optical properties of aerosols observed in Lille. Therefore, in the following sections, we have chosen to utilize estimates of optical properties derived from SOLARTDECO, particularly of the Single Scattering Albedo (SSA), asymmetry parameter (g), and fine fraction (ff), to supplement the analysis of solar radiation variability presented in Section 3.~~

2.4 Multivariate analysis of SSI variability

In the present study, we undertake a multivariate analysis of the variability of the surface solar irradiance in Lille over the period 2010-2022. The objective is to disentangle the contributions of the change in sky's conditions (presence or absence of clouds, aerosol class and loading, atmospheric parameters) and geometrical conditions to the observed variabilities of the SSI. This section presents the methodology for the multivariate analysis (Section 2.4.1), as well as the sensitivity study of the SSI to input parameters that is used to perform the multivariate analysis (Section 2.4.2). For the purpose of this study, this methodology has been applied to analyze trends and year-to-year variability of the SSI over the period 2010-2022 (Section 3.2) in spring (i.e. March-April-May) and summer (i.e. June-July-August). Nonetheless, it is worth mentioning that it could also be applied at other temporal resolutions, including monthly and intra-daily scales.

Sections 3.2.1 and 3.2.2 have been moved in the present section for clarity (Sections 2.4.1 and 2.4.2).

2.4.1 Methodology

The seasonal mean all-sky solar irradiance can be written as a weighted sum of the observed irradiances per sky condition:

$$F_{ASKY} = \sum_{k} F_k \times freq_k \tag{2}$$

where k represents the sky's condition (CLOS, CSWC or CSKY), F_k corresponds to the associated measured seasonal mean irradiances (GHI, BHI or DHI), and $freq_k$ represents the yearly mean frequency of the «k-th» sky condition for the corresponding season.

With this approach it is possible to isolate the contributions of the change in frequency of occurrence of sky conditions and of the change in irradiance under each sky conditions to both inter-annual variability and trends of all-sky irradiances. Indeed, this decomposition allows the analysis of the observed differences between the year "y" and the overall mean over the period 2010-2022:

$$\Delta F_{ASKY,\,y} = \sum_k (\Delta F_{k,\,y} \times freq_{k,\,y} + F_{k,\,y} \times \Delta freq_{k,\,y}) \tag{3}$$

where $F_{k,\,y}$ and $freq_{k,\,y}$ represent the mean seasonal irradiances and frequencies of the various sky conditions for the year "y", and the terms $\Delta F_{k,\,y}$ and $\Delta freq_{k,\,y}$ correspond, respectively, to the observed differences in irradiance and frequency of sky conditions between the seasonal averages for the year "y" and over the whole period of interest. With this framework, the term $F_{k,\,y} \times \Delta freq_{k,\,y}$ represents the contribution of the change of the sky's frequency of occurrence to the variability $\Delta F_{ASKY,\,y}$, while the term $\Delta F_{k,\,y} \times freq_{k,\,y}$ corresponds to the contribution of the change of irradiance observed under each sky conditions.

A similar approach can be used to decompose the eventual observed trends under all-sky conditions over the period 2010-2022 following Equation 4:

$$\frac{dF_{ASKY}}{dt} = \sum_k \left(\frac{dF_k}{dt} \times freq_k + F_k \times \frac{dfreq_k}{dt} \right) \tag{4}$$

where F and $freq_k$ are the same as in Equation 3 while $\frac{dF}{dt}$ and $\frac{dfreq}{dt}$ correspond, respectively, to the slopes of the observed seasonal trends in irradiances and frequencies of the various sky conditions. Again, the terms $F_k \times \frac{dfreq_k}{dt}$ and $\frac{dF_k}{dt} \times freq_k$ represent the influence of the trends in the occurrences of the sky conditions and the trends in other atmospheric parameters, respectively.

This analysis of the different contributions to the observed irradiance variabilities can be extended by further decomposing the terms related to the variability of the irradiances observed under each sky conditions, that we note here CSKY, CSWC and CLOS. We describe here a second and third step, for which we decompose the irradiances variability, only in the case of CSKY and CSWC (i.e. CSUN) situations, by accounting for changes in the occurrence of the five main aerosol class and changes in solar irradiances per aerosol class. Note that for CSWC conditions, this is only valid for the BHI which is not influenced by clouds.

As in the previous paragraph, the seasonal mean solar irradiance for CSKY and CSWC conditions can be written as a weighted sum of the observed mean irradiances per aerosol class:

$$F_{clear} = \sum_i F_i \times freq_i \tag{5}$$

where F_{clear} represents the mean seasonal irradiances measured under clear-sky or clear-sun with clouds conditions, and the terms $freq_i$ and F_i correspond to the mean frequencies and irradiances of the "i-th" aerosol class[1] (i.e., "Continental," "Continental polluted," "Mixed," "Maritime," "Desert dust") for the same conditions (CSKY or CSWC). Then, similarly to the approach used under all-sky conditions, it is possible to isolate the contribution of the change of aerosol class' frequency and the change of irradiance per aerosol class, both for the inter-annual variability (Equation 6) and trends (Equation 7) :

$$\Delta F_{clear,\,y} = \sum_i (\Delta F_{i,\,y} \times freq_{i,\,y} + F_{i,\,y} \times \Delta freq_{i,\,y}) \tag{6}$$

$$\frac{dF_{clear}}{dt} = \sum_i \left(\frac{dF_i}{dt} \times freq_i + F_i \times \frac{dfreq_i}{dt} \right) \tag{7}$$

where $\Delta F_{i,\,y}$ and $\Delta freq_{i,\,y}$ represent the observed differences in irradiances and frequencies of the different aerosol classes between the seasonal averages for the year "y" and over the period 2010-2022, and the terms $\frac{dF_i}{dt}$ and $\frac{dfreq_i}{dt}$ correspond to the slopes of the observed seasonal linear trends in irradiances and frequencies of the various aerosol classes. In this writing, $\Delta F_{i,\,y}$ and $\frac{dF_i}{dt}$ results from the variabilities of every scene's parameter (AOD, SSA, SZA, PWV, etc.) to which the irradiances are sensitive. In order to isolate and identify the impacts of each parameter, it is possible~~necessary~~ to further decompose these terms following Equations 8 and 9 :

$$\Delta F_{i,\,y} = \sum_x \left[\frac{\partial F}{\partial x} \right]_{i,\,y} \times \Delta x_{i,\,y} \tag{8}$$

$$\frac{dF_i}{dt} = \sum_x \left[\frac{\partial F}{\partial x} \right]_i \times \frac{dx_i}{dt} \tag{9}$$

where $\left[\frac{\partial F}{\partial x}\right]$ corresponds to the seasonal sensitivity of the irradiances to the various parameters "x" (AOD, SZA, SSA, etc.), and the terms $\Delta x_{i,\,y}$ and $\frac{dx_i}{dt}$ represent the temporal variations (for a given season) of the considered parameter for the "i-th" aerosol class. Note that the comparisons between SOLARTDECO simulations, based on AERONET measurements, and irradiance measurements from ATOLL in clear-sky conditions in Lille showed satisfactory results (Section 2.3.2). This validates both the modelling of the aerosol optical properties and the radiative transfer processes. Hence, we use with confidence SOLARTDECO simulations to compute the sensitivities of irradiances to the various atmospheric parameters, as described in Section 2.4.2.

2.4.2 Sensitivity study of clear-sky SSIirradiances ~~to atmospheric parameters~~

The sensitivity of clear-sky irradiances, «F», to each input of SOLARTDECO, «x», is quantified by the computation of partial derivatives, which are obtained by imposing a small perturbation «δx» to the value of x as in Equation 10:

$$\frac{\partial F}{\partial x} \approx \frac{\delta F}{\delta x} = \frac{F(x+\delta x,\, y_1,\, \ldots,\, y_n) - F(x,\, y_1,\, \ldots,\, y_n)}{\delta x} \tag{10}$$

where $y_1, \ldots, y_n$ are the other parameters, beside the variable of interest x, needed to compute the clear-sky irradiances F (i.e. GHI, BHI or DHI). As in Thorsen et al. (2020), the perturbation of the parameter x is taken as an arbitrary increase of

[1]The "Strong events" class is not considered for the decomposition of the clear-sun irradiances as it represents less than 1% of observations in Lille.

1% of the base value, which should be simultaneously small enough to induce a linear impact on the irradiances and large enough to avoid noise from numerical truncation errors. The analysis of these sensitivities is interesting in itself as it provides understanding about the importance of each parameter, and how accurately they should be defined. It also shows how different the sensitivities of the direct and diffuse irradiances can be, and how they can lead to reduced sensitivities of GHI through compensation mechanisms. It indicates also the possible importance of aerosol's nature that interact differently with solar radiation over the solar spectrum. As the values of the scene's pertaining parameters have different magnitudes (e.g. SZA versus AOD), we chose to provide here values of the logarithmic sensitivity:

$$\frac{\partial ln(F)}{\partial ln(x)} = \frac{\partial F/F}{\partial x/x} \tag{11}$$

where F represents the irradiances (GHI, BHI or DHI) and «x» the parameter of interest. The logarithmic sensitivities thus represent the response of the irradiances (in %) to a relative variation in the input parameter (here an increase) of 1 %.

	GHI	**BHI**	**DHI**
SZA (°)	-2.47e+00	-2.80e+00	-1.18e+00
$\mathbf{AOD_{550}}$	-4.92e-02	-1.67e-01	4.08e-01
$\mathbf{SSA_{550}}$	1.71e-01	0.00e+00	8.38e-01
ff	1.59e-03	2.18e-02	-7.69e-02
$\mathbf{H_{aer}}$ (km)	-2.12e-04	0.00e+00	-1.04e-03
RH (%)	2.81e-03	-3.98e-04	1.53e-02
PWV (cm)	-5.68e-02	-6.68e-02	-1.78e-02
$\mathbf{O_3}$ (DU)	-2.74e-02	-2.41e-02	-4.01e-02
$\mathbf{O_2}$ (ppmv)	-7.55e-03	-8.03e-03	-5.69e-03
$\mathbf{CO_2}$ (ppmv)	-2.64e-03	-3.25e-03	-2.55e-04
α	1.30e-02	0.00e+00	6.34e-02

(a)

	GHI	**BHI**	**DHI**
SZA (°)	-58.6	-66.5	-28.0
$\mathbf{AOD_{550}}$	-3.0	-10.3	25.1
$\mathbf{SSA_{550}}$	0.6	0.0	2.7
ff	0.0	0.5	-1.9
RH (%)	0.1	-0.0	0.5
PWV (cm)	-2.6	-3.0	-0.8
$\mathbf{O_3}$ (DU)	-0.3	-0.2	-0.4

(b)

Table 3. Logarithmic sensitivities of global (GHI), direct (BHI) and diffuse (DHI) SSI~~irradiances~~ to SOLARTDECO input parameters (the parameters related to aerosol properties are grouped) in the case of the continental aerosol class. Results are given in % and equal the relative variation of irradiances for (a) a 1 % variation and (b) a variation of the order of the coefficient of variation, of each input parameter. Computations were carried out for the continental aerosol class using a fixed set of parameters based on average properties observed under clear-sky conditions and over 2010-2022. The parameter ff represents the aerosol fine mode fraction, RH the relative humidity, PWV the precipitable water vapor content, H_{aer} the aerosol layer height (fixed at 2 km), and α the surface albedo.

Table 3a presents the logarithmic sensitivities of the clear-sky irradiances to the input parameters of SOLARTDECO (aerosol-related parameters are grouped) in the case of the most frequent aerosol class in Lille, i.e. the continental class. The sensitivities are calculated with, as the reference, a fixed set of properties that correspond to mean values observed in clear-sky conditions over the period 2010-2022 (Table S1). Note that for the aerosol layer height (H_{aer}) we used the fixed input value

(2 km) from SOLARTDECO described in Section 2.3.1. The mean value of fine fraction «ff» used in this study comes from AERONET estimates based on the method of O'Neill et al. (2003). Moreover, as the number of available AERONET inversions of SSA is relatively small and thus less representative, the mean single scattering albedo is based on the aerosol optical properties computed by mixing the fine and coarse modes (Equation B9) for each clear-sky simulations over 2010-2022. This is valid as the satisfactory results of SOLARTDECO simulations suggest a good transcription of aerosol optical properties derived for the mixing of the fine and coarse modes. Overall, our sensitivity results show that the most important parameter is the solar zenithal angle whose 1 % increase (0.6°) induces a 2.5 % decrease of the GHI. The second most significant parameter is the single scattering albedo that affects only the diffuse component. The third most important parameter is the aerosol optical depth, although the compensation between two opposite in sign effects on BHI and DHI leads to an overall effect on GHI on the order of the effects of PWV variation. It is to be noticed that an increase of the fine fraction, for a constant AOD_{550}, does increase BHI and decrease DHI, which results from an overall decrease of the aerosol extinction over the solar spectrum, consequence of a higher Angström exponent. Sensitivity's results in the case of larger particles, e.g. maritime, not shown here, show sensitivities to AOD 5 to 10 % higher in magnitude. It shows also a sensitivity to ff two of three times higher in magnitude. Both differences can be attributed to a modification of the aerosol's optical properties over the whole solar spectrum.

It is nevertheless biased to compare the irradiance's sensitivities to all parameters as in Table 3a, as these parameters have actually different ranges of variation. It is thus more pertaining to account for these different ranges by multiplying each logarithmic sensitivities by the coefficient of variation of each parameter, defined as the ratio between the standard deviation and the associated mean value of this parameter observed in Lille. Table 3b provides the sensitivities of the irradiances (in %) to the various parameters for changes of the order of the coefficient of variation, still in the case of the aerosol's continental class. Note that the sensitivities to the surface albedo (α), oxygen (O_2), carbon dioxide (CO_2) concentrations, and aerosol layer height (H_{aer}) are not represented, as these parameters are constant in our simulations. Accounting for the variation of the input parameters, the clear sky irradiance's sensitivities in Lille are thus, in decreasing order, related to the solar zenith angle, the aerosol optical thickness, the precipitable water vapor content, the single scattering albedo and the fine fraction, with relatively weak impacts (<1% for all irradiance components) of the relative humidity and ozone content. The ordering of the sensitivities to SSA and PWV are inverted when considering only the diffuse irradiance. These results indicate the primary importance of the SZA: a temporal change of a clear-sky condition can lead to a significant change of the solar irradiance, through modification of both the optical air mass and the horizontal projection of radiances, that affect more the direct than the diffuse horizontal irradiance. Also, a typical increase of aerosol loading ($\overline{\text{AOD}} + \sigma$) would lead to a 10 % decrease of BHI, a 25 % increase of DHI, and a 3 % decrease of GHI. A more thorough analysis of the global non-net direct radiative impact of aerosols on the solar irradiance in Lille over 2010-2022, based on SOLARTDECO simulations as well as ATOLL irradiance measurements, is presented in Section 4 for clear-sun conditions, with seasonal and yearly averages, and a distinction per aerosol class.

Finally, it is important to note that the sensitivities presented in this section are only for the continental class and over the entire period 2010-2022. Specific sensitivities, which vary according to the considered time period as well as the aerosol class, have been computed in order to perform the multivariate analysis of inter-annual variability and trends presented in Sections 3.2.1 and 3.2.2.

3 Analysis of SSIthe surface solar irradiance's variability over 2010-2022

In this section, the results of the joint analysis of the simultaneous measurements conducted in Lille over the period 2010-2022 are presented. This analysis relies on both classifications of the sky conditions and aerosol optical properties introduced in Section 2, as well as on the radiative transfer simulations (in clear-sky conditions) of SOLARTDECO. The objective is to obtain a climatology of the solar environment in Lille over the past decade (Section 3.1) and examine the influence of clouds, aerosols, and gases on the variability of surface radiation in northern France (Section 3.2).

Firstly, in Section 3.1.1, the seasonal variability of solar irradiance, aerosol optical properties, and sky conditions is examined. Then we focus in Section 3.1.2 on their inter-annual variability in spring (i.e. March-April-May) and summer (i.e. June-July-August) over the period 2010-2022. Finally, SIn section 3.2 presents the results of the multivariate analysis of the year-to-year variability and trends in surface solar irradiances in spring and summer, based on the methodology described in Section 2.4. , we develop a framework that allows to make the distinction between the different variabilities of the scenes, atmospheric components and geometries, that contribute to the variabilities and trends recorded for surface solar irradiance.

3.1 Recorded variabilities of sky conditions, aerosols and SSI

3.1.1 Mean climatology and sSeasonal cycle

Figures 4a-h present the average monthly variations during daytime over the 13-year period 2010-2022 of different measured and derived atmospheric quantities associated to the solar environment in Lille: (Figure 4a) sky conditions identified with the irradiance-based cloud-screening methods described in Section 2.2.1, (Figures 4b-d) aerosol properties from AERONET measurements, and (Figures 4e-h) irradiances measured for the different sky conditions.

The results of our cloud-screening approach confirm the significant influence of clouds in Lille observed by Warren et al. (2007). Over the 13-year period considered, we find that, on average, the Sun is obscured by clouds (CLOScloudy-sun situations) in nearly 67% of cases, while completely clear skies are observed only 11% of the time, and intermediate conditions of partly cloudy skies with a visible Sun (CSWC clear-sun with clouds conditions) represent only an average of 22% of observed situations. Thus, the sun is clear of clouds 33% of the time (CSUNclear-sun conditions). Note that CLOScloudy-sun situations also encompass instances characterized by thin clouds or clouds partially covering the Sun (cloud edges), which have a limited impact on incident solar radiation, with Direct Normal Irradiance (DNI) values exceeding 120 W/m^2 (sunshine criterion defined by the World Meteorological Organization [WMO (2003)]). On average over the period 2010-2022, these situations, which can be considered as "sunny", represent 9% of observed conditions, and account for about 13% of "cloudy-sun" situations. The maximum (resp. minimum) of CSKYclear-sky (resp. CLOScloudy-sun) occurrence happens in March-April. Clear-sky conditions are minimum in winter, with average occurrences of only around 5%, associated with a maximum of cloudy-sun conditions of around 80%. A relatively stable plateau of minimum (resp. maximum) cloudy-sun (resp. clear-sun) monthly proportions, with values consistently lower (resp. greater) than 65% (11 and 24% for clear-sky and clear-sun with clouds conditions), is also noticeable from March to September, i.e. spring (March-April-May) and summer (June-July-August).

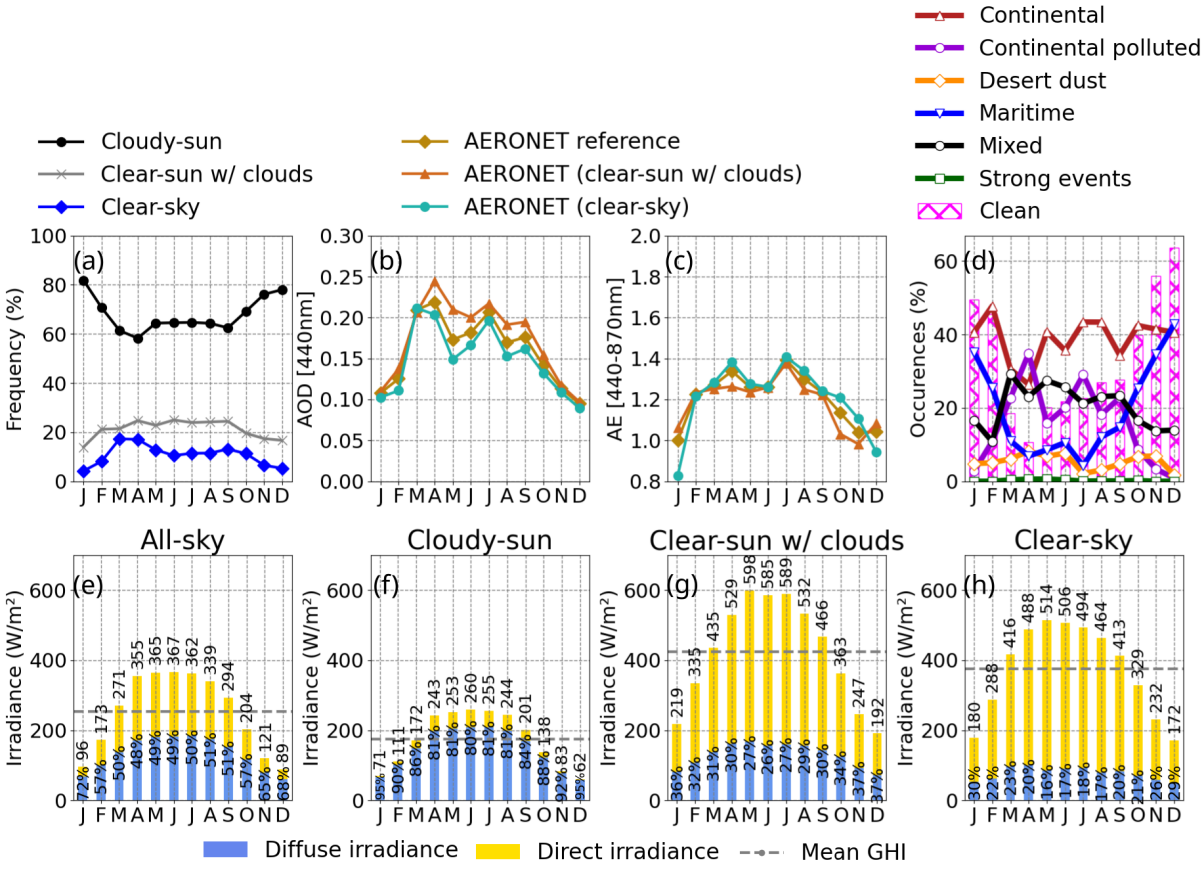

Figure 4. Monthly variations in Lille over the period 2010-2022 of several quantities derived from ATOLL measurements. (a) Frequencies of cloudy-sun (black line), clear-sun with clouds (grey line) and clear-sky moments (blue line) in percentages. (b) Monthly mean values of AOD_{440} for all AERONET measurements~~overall~~ (i.e. AERONET reference, brown line) and for different sky conditions: clear-sun with clouds (orange line) and clear-sky (green line). (c) Same as (b) but for the $AE_{440-870}$. (d) Proportions of the different classes presented in Table 2: continental (red line), continental polluted (purple line), desert dust (orange line), maritime (blue line), mixed (black line) and strong events (green line). The proportion of clean situations ($AOD_{440} \leq 0.1$) for all coincident AERONET measurements is also represented as pink columns. (e-h) Mean monthly SSI~~irradiances~~ for different cloud cover states: (e) all-sky, (f) cloudy-sun, (g) clear-sun with clouds and (h) clear-sky. Only values during daytime between [sunrise + 30 minutes; sunset - 30 minutes] are considered. The GHI is represented as columns with the lower blue part corresponding to the DHI and the upper yellow part to the BHI. The grey dashed lines represent the mean GHI over 2010-2022. Note that the percentages reflect the contribution of the DHI to the overall mean yearly GHI which values are reported above each column.

Figures 4b-d illustrate the monthly variability of aerosol optical properties in Lille over the period 2010-2022. Panels (b) and (c) respectively represent the mean values of AOD and AE for all AERONET measurements, as well as individually for situations coincident with clear-sky and clear-sun with clouds observations. In addition, panel (d) illustrates the monthly variability in the occurrences of the six aerosol classes defined in Section 2.2.2, as well as the monthly proportions of clean situations ($AOD_{440} \leq 0.1$), considering all AERONET measurements. Overall, Lille appears to be a fairly polluted site as only 27% of AOD_{440} measurements show values lower than 0.1. Table 2 shows that the main contribution is from the Continental class (38%), followed by Mixed cases (22%) and Continental polluted events (20%). Hence, aerosols observed in Lille are mostly related to anthropogenic activities as fine particles prevail at least 58% of the time. However, a non negligible contribution of coarse particles is observed as the Maritime and Desert dust classes represent 14% and 5% of the observations, respectively (Table 2). Note that the proportion of desert dust influence obtained from our aerosol classification in clear-sun conditions in Lille is consistent with that previously provided by Putaud et al. (2010), based on particulate matter measurements in all-sky conditions, as these authors estimate a mean proportion of desert dust particles in the range of 5 to 12% in the North of Europe. Moreover, Figures 4b-d show that the period from March to September, characterized by a higher proportion of clear-sun conditions, is also significantly influenced by aerosols, with monthly mean AOD_{440} values greater than 0.15 (Figure 4b). The stability of the associated Angström exponents (values greater than 1.2, Figure 4c) indicatessuggest a significantstrong influence of fine particles, primarily from anthropogenic emissions, reaching a maximum in April (monthly mean values of AOD_{440} exceeding 0.2), with an minimum proportion of AOD measurements below 0.1 (clean conditions) of only 11% (Figure 4d). SIt can be noted that spring is indeed characterized by a significant increase in agricultural activity, including fertilizer spreading in open fields that, which releases substantial amounts of ammonia into the atmosphere, which contribute to the formation of secondary aerosols (Hauglustaine et al., 2014). Moreover, the predominantly northeast wind flow observed in spring in Lille (Figure S4b), could be the result ofmay indicate a higher frequency of anticyclonic conditions during this season. Overall, this wecould explain the overall lower frequency of cloudy moments and the accumulation of anthropogenic particles originating partly from the Benelux region. The accumulation of anthropogenic particles is consistent with the strong influence of the "Continental Polluted" aerosol class, reaching a maximum monthly average of about 35% around April (Figure 4d). Conversely, in winter, when cloudy conditions are more frequent (Figure 4a), the monthly mean values of AOD generally remain below 0.12, reaching a minimum of 0.09 in December (Figure 4b). This winter drop in AOD is associated with a decrease in the monthly mean AE (Figure 4c). These two decreases result from a higher proportion, which suggests an increased influence of coarse particles. The generally lower AOD and AE values result in a more significant impact of the "Maritime" aerosol class, with monthly proportions exceeding 35% for winter months (Figure 4d). This finding aligns with surface wind direction and speed measurements from the ATOLL platform, which highlight prevailing westerly windsa prevailing influence from the southwest (Figure S4a), that are less influenced by continental anthropogenic activitiesparticularly from the English Channel region.

Figures 4e-h represent the monthly variability of the incident global surface flux in Lille over the period 2010-2022, as well as the partitioning between direct and diffuse components for (e) all-sky (ASKY), (f) cloudy-sun (CLOS), (g) clear-sun with

clouds (CSWC) and (h) clear-sky (CSKY) conditions. Note that only measurements performed between [sunrise + 30 minutes; sunset - 30 minutes] are considered, as the identification of the sky state performs better during this period.

Overall, the climatological yearly mean value of global irradiance (GHI) is minimum in cloudy-sun conditions (192~~174~~ W/m^2), when the Sun is obscured by clouds. In comparison, the measured surface flux in clear-sky conditions is twice as high, with an average value around 375~~435~~ W/m^2. The maximum irradiance is observed for clear-sun with clouds conditions, which, due to the cloud side effects on the diffuse component, show a mean value around 424~~484~~ W/m^2 (13~~1~~% more than clear-sky). Thus, in conjunction with the frequency of each sky condition (Figure 4a), the average solar radiation incident in Lille under all-sky conditions is approximately 253~~285~~ W/m^2. In addition to the discrepancies in GHI, it is worth mentioning that each sky condition is associated with varying proportions of direct and diffuse irradiance. In particular, the yearly mean diffuse ratio observed in Lille over the period 2010-2022 vary between a minimum of 22~~25~~% in CSKY~~clear-sky~~ conditions and a maximum of 87~~93~~% in CLOS~~cloudy-sun~~ situations, with intermediate values of 32~~34~~ and 56~~72~~% in CSWC~~clear-sun with clouds~~ and ASKY~~all-sky~~ conditions. This broad range of values highlights the predominant effects~~significant influence~~ on the measured surface global irradiance in Lille of ~~the presence of~~ clouds and their position relative to the Sun and the observer.

Figures 4e-h show that the seasonal variations of the mean measured irradiances for all sky states display almost symmetrical inverted U-shapes over the year, that are linked to changes in solar zenith angle (Figures S3a-d) and thus optical air mass, which are greater in winter (minimum GHI) than in summer (maximum GHI). Moreover, the variability of the optical air mass has a great influence on the proportion of diffuse irradiance, which varies, under all-sky conditions, between 51~~69~~% in summer to more than 65~~85~~% in winter. Note that in all-sky conditions, the influence of the optical air mass is enhanced by changes in occurrence of the sky conditions as the frequency of cloudy-sun conditions (Figure 4a) is greater (resp. lower) in winter (resp. summer), leading to overall lower (resp. greater) mean ASKY GHI values. The influence of clouds is particularly important under CSWC~~clear-sun with clouds~~ conditions, as clouds, through 3D effects, enhance the amount of diffuse radiation reaching the surface. Most notably, our results highlight that, due to the additional contribution of clouds, the monthly averages of global flux are, throughout the year, consistently higher for CSWC~~clear-sun with clouds~~ conditions (Figure 4g) than for CSKY ~~clear-sky~~ situations (Figure 4h), with relative differences varying between +4% in March and +21% in January, and a absolute maximum difference of 95 W/m^2 in July. I~~t is worth noting that i~~n CSWC conditions, the gain from clouds results in diffuse flux values around 170 W/m^2 on average in summer, which are relatively comparable to those observed in CLOS conditions, reaching around 200 W/m^2 on average for the same season. In relative terms, the contribution of diffuse radiation is however significantly lower in CSWC conditions, with an average proportion of DHI around 28~~30~~% in summer, compared to 81~~80~~% in CLOS conditions. CLOS conditions thus typically offer a very low direct radiation and a moderate amount of diffuse radiation, leading to global surface radiation levels that are two to three times lower, depending on the month, compared to other situations.~~The presence of a cloud in the Sun's direction thus significantly reduces incident direct radiation without truly increasing diffuse radiation. The incident global surface radiation in CLOS conditions is thus much lower than in clear-sun with clouds situations.~~

To conclude, our joint analysis of the seasonal variability of the solar environment suggests that the period covering spring and summer is characterized by relatively high amounts of incident radiation and surface energy, linked to smaller solar zenith

angles and longer day lengths. Both seasons are thus particularly interesting in terms of solar energy exploitation, as the period from March to September represents nearly 80% of the total energy accumulated over a year (approximately 1 MWh/m^2, Figure S3a). Hence, we chose to focus our study of the inter-annual variability of the solar environment in Lille over the period 2010-2022 (Section 3.1.2) on spring and summer seasons. Note that as these two seasons are generally characterized by a lower influence of clouds and relatively high levels of AOD, they are of great interest for the study of the impact of aerosols on the ~~solar irradiance incident at the surface, as the impact of aerosols on the~~ SSI and its direct/diffuse partition ~~should be maximum in spring and summer under both clear-sun and all-sky conditions. A more thorough analysis of the direct radiative effect (DRE) of aerosols is presented in Section 4~~.

3.1.2 Year-to-year evolution~~variability~~ in spring and summer

Figures 5 and 6 represent the year-to-year evolution from 2010 to 2022 of daytime sky conditions (5a and 6a), aerosol properties obtained from AERONET measurements (5b-d, 6b-d), and surface solar irradiances measured for the different sky conditions (5e-h, 6e-h), in Lille in spring and summer respectively. Figures 5 and 6 show some local extrema of interest for these quantities, such as the maximum of irradiance and clear-sky occurrence of spring 2020. They show also some interesting trends over the past decade, part of which are statistically significant.

The 2010-2022 yearly averaged occurrence of clear-sky (CSKY) conditions represents 15% of the observations in spring, whereas in summer it is substantially lower, corresponding to ~~only~~ 11% ~~of the measurements~~. T~~Consistently, t~~he Sun is on average obscured by clouds (cloudy-sun, CLOS) 62% of the time in spring, and 65% ~~of the time~~ in summer. The Sun is clear and surrounded by clouds (clear-sun with clouds, CSWC) 23% and 24% of the time in spring and summer, respectively. For both seasons, the year-to-year variabilities~~y~~ reported in Figures 5a and 6a show~~suggest~~ decreasing linear trends in the frequency of CLOS~~cloudy-sun~~ conditions of about -0.9% per year, and inversely increasing trends in the frequency of CSWC and CSKY conditions of about +0.4 to 0.5% per year. Precise values of the trends are given in Table 4a. As highlighted in bold in Table 4a, and with solid green lines in Figures 5a and 6a, these seasonal trends are statistically significant (application of Mann-Kendall trend tests (Mann, 1945; Kendall, 1990) with a significance level of 5%) only in summer concerning the occurrences of CLOS and CSWC situations. These trends are issued from only 13 years of data, and rely on the imperfect filtering of sky conditions. Their scope should thus be considered with caution as they are quite sensitive to year-to-year variability, and as uncertainty in the occurrences of sky conditions impact their validity. However, it is worth noticing that the strongest (significantly decreasing) trend in CLOS situations was found to be associated with a high confidence in the related occurrences (1.2% of misidentifications) and that this observation is consistent with results from CM SAF data (C3S, 2024) that show since 2010 repeated negative annual anomalies in cloud cover and positive ones in sunshine duration, over European land areas and relative to the reference period 1991-2020. It does encourage a multivariate analysis that includes the observed variabilities in the observed occurrences' trends as in Equation 4.~~, more pronounced in summer (-0.9 ± 0.4% per year) than in spring. In summer, our analysis suggests significant increasing trends in both clear-sun with clouds (+0.5 ± 0.2% per year) and clear-sky (+0.4 ± 0.3% per year) frequencies. As indicated in Table 4a, seasonal Mann-Kendall trend tests (Mann, 1945; Kendall, 1990), with a significance level of 5%, validate only the decrease in the frequency of cloudy-sun situations in summer~~

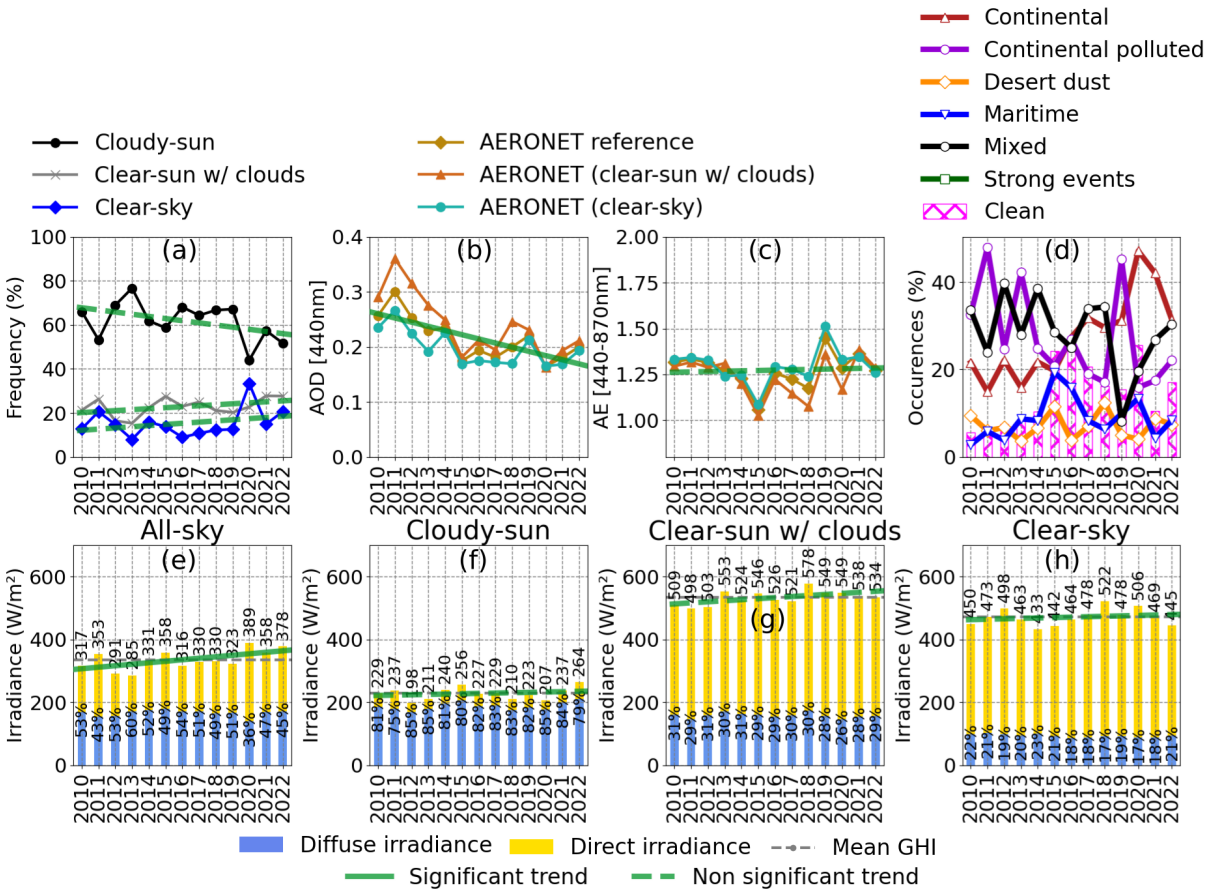

Figure 5. Same as Figure 4 but for yearly variations in spring between 2010 and 2022.

and the opposite increase in clear-sun with clouds conditions. In spring, the trends in sky conditions, although consistent with those reported in summer, are not statistically significant (Table 4a), possibly due to the higher year-to-year variabilities recorded for this season. The spring of 2020 is particularly exceptional with 35% of CSKY occurrences, and only 43% of CLOS situations. Indeed, the proportion of clear-sky moments in spring oscillates between a minimum of around 8% in 2013 (compared to a minimum of 7% in summer 2011) and a maximum in 2020 of 35% (compared to a maximum of 20% in summer 2018), which can be considered as an extremely high value in Lille. Note that correspondingly, spring 2020 presents the lowest proportion of cloudy-sun moments with a mean frequency of 43%, compared to a minimum of 51% in summer 2022. An anomaly withoverall very low cloud fraction was also observed in Cabauw (Netherlands) in spring 2020 by Heerwaarden et al. (2021). This study showed, in particular, that the particular anticyclonic meteorological conditions of that spring were associated with record-breakingunique meteorological conditions of spring 2020, especially the low observed cloud fraction, led to record all-sky global irradiance measurements in Cabauw. These conditions were also characterized by a relatively low contribution of diffuse radiation, accounting for 38%, as opposed to over 50% on average in spring in Cabauw. Similarly, in

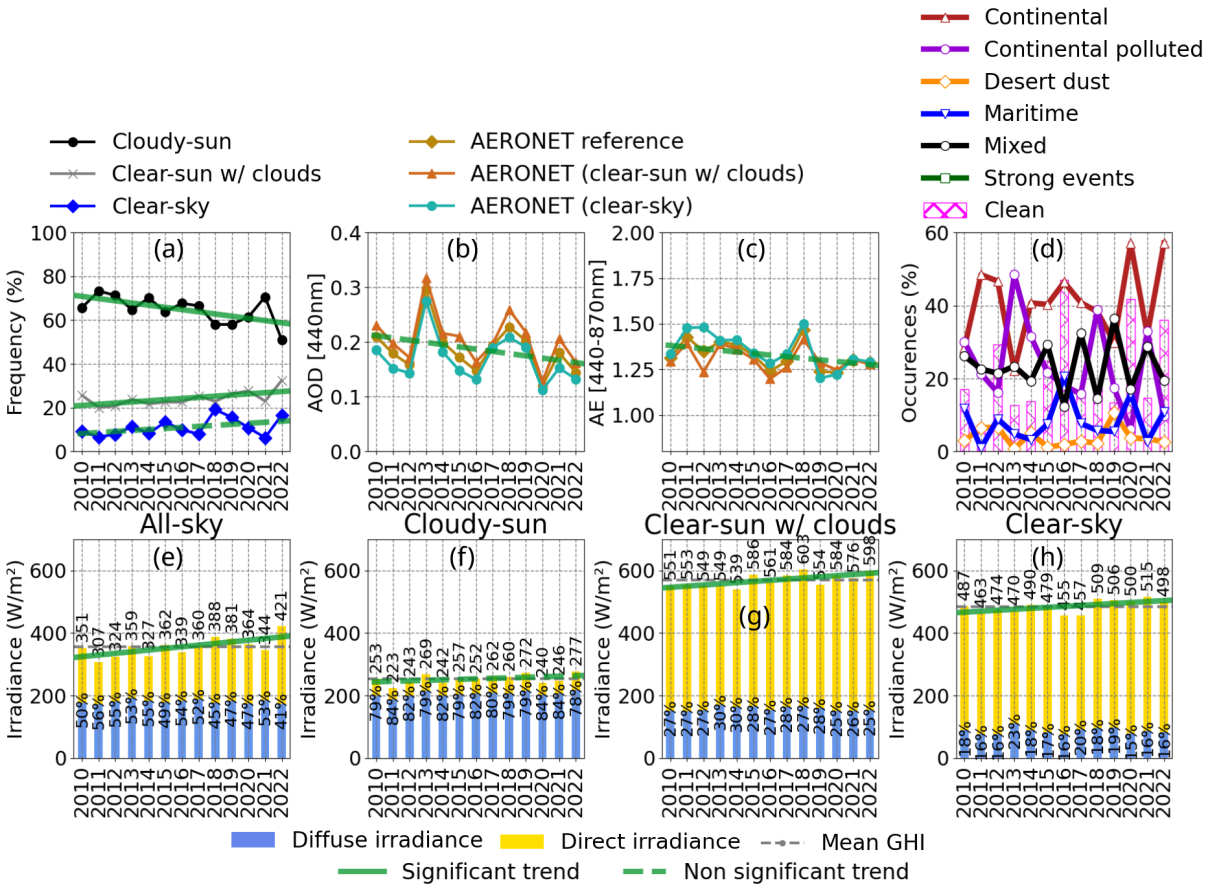

Figure 6. Same as Figure 5 but for summer. This figure has been changed due to an error in the code that showed a solid green line in AE despite a non-significant trend.

Lille, a~~n~~ high average global irradiance under all-sky conditions was observed in spring of 2020 (389 W/m^2), representing the maximum GHI over the whole period 2010-2022 for the spring season (Figure 5e). T~~In particular, t~~his remarkable value is 55 W/m^2 ~~(16%)~~ higher (+16%) than the spring average observed over the period 2010-2022 (334 W/m^2). Additionally, the ~~relatively~~ low contribution of the DHI (36%), similar to that measured in Cabauw, is notably lower than the ~~usual~~ seasonal averages observed in spring in Lille, the other years of 2010-2022 ranging between 43 and 60% ~~between 2010 and 2022~~. A detailed analysis of the contribution of the variability of the aerosol content and occurrences of sky conditions to the maximum solar radiation in the spring of 2020 is presented in Section 3.2.1.

Figures 5b-d and 6b-d represent the variations of the yearly-averaged aerosol content and properties in Lille over the period 2010-2022 in spring and summer respectively. For both seasons, strong fluctuations of AOD_{440} are observed (Figures 5b and 6b) when considering all reference AERONET measurements (i.e. clear-sun measurements, brown line) as well as only those coincident to clear-sun with clouds (orange line) and clear-sky (green line) observations. In spring, our measurements show a

	2010-2022 mean (%)/ [trend ± standard-deviation] (% per year)	
Proportion of	**Spring**	**Summer**
Cloudy-sun	62%/[-0.98 ± 0.60]	65%/**[-0.92 ± 0.40]**
Clear-sun w/ clouds	23%/[0.42 ± 0.26]	24%/**[0.48 ± 0.20]**
Clear-sky	15%/[0.56 ± 0.49]	11%/[0.44 ± 0.28]

(a) Frequency of sky conditions

	Trend ± standard deviation	
AOD [440nm] (unit per year)	**Spring**	**Summer**
Clear-sun	**(-0.008 ± 0.002)**	(-0.004 ± 0.003)
Clear-sun with clouds	**(-0.011 ± 0.003)**	(-0.004 ± 0.003)
Clear-sky	**(-0.006 ± 0.002)**	(-0.003 ± 0.003)
Frequency of occurrence (% per year)		
Continental Clear-sun with clouds/Clear-sky	**(+2.2 ± 0.6)/(+1.7 ± 0.5)**	(+1.2 ± 0.6)/(+0.4 ± 1.0)
Continental polluted Clear-sun with clouds/Clear-sky	**(-1.8 ± 0.7)/(-0.9 ± 0.8)**	(-1.0 ± 0.6)/(-1.5 ± 0.9)

(b) AOD and frequency of occurrence of continental and continental polluted aerosol classes

	Trend in GHI/BHI/DHI (W/m^2/year) ± standard deviation	
	Spring	**Summer**
All-sky	**(3.95 ± 1.90)/(4.36 ± 2.30)**/(-0.41 ± 0.77)	**(4.21 ± 1.85)/(4.66 ± 1.89)**/(-0.45 ± 0.46)
Cloudy-sun	(0.27 ± 1.31)/(-0.45 ± 0.65)/(0.72 ± 0.79)	(0.63 ± 1.16)/(0.09 ± 0.61)/(0.54 ± 0.59)
Clear-sun with clouds	(3.34 ± 1.43)/**(3.70 ± 1.07)**/(-0.36 ± 0.61)	**(3.73 ± 1.19)/(3.84 ± 1.21)**/(-0.11 ± 0.55)
Clear-sky	(1.35 ± 1.99)/(2.27 ± 2.08)/**(-0.92 ± 0.29)**	**(3.08 ± 1.26)/(3.08 ± 1.33)**/(0.002 ± 0.76)

(c) Surface solar irradiances

Table 4. Trends per year in frequency of sky conditions (a), aerosols (b), and SSI (c) recorded in Lille in spring and summer over the period 2010-2022. Only parameters with at least one statistically significant trend (Mann-Kendall test, highlighted in bold text) in spring or summer are reported. Note that other parameters such as the solar zenith angle, precipitable water vapor content and Angström exponent were also investigated, however, no significant trends were observed.

significant decreasing trend in AOD_{440} over the period 2010-2022 (-0.008 $\pm$ 0.002 per year) from a yearly mean value of 0.26 in 2010 to around 0.20 in 2022. By comparison, the observed negative trend in summer (-0.004 $\pm$ 0.003 per year) appears to be much lower and statistically non-significant (Table 4b). This decrease in AOD recorded in Lille agrees with the analysis of Ningombam et al. (2019) who identified a generalized decreasing trend in AOD for several European AERONET stations since 1995. The yearly mean Angström Exponent appears to be relatively stable for both seasons (Figures 5c and 6c) with overall mean values of 1.27 and 1.33 respectively in spring and summer. Interestingly, in spring, the stable AE and decrease in AOD translates in balancing trends in the occurrences of the Continental (+1.9 $\pm$ 0.4 % per year) and Continental polluted classes (-1.2 $\pm$ 0.7 % per year), while in summer no trends in the occurrences of these two aerosol classes are~~is~~ statistically significant (Figures 5d and 6d).

Figures 5e-h and 6e-h depict the annual variations, for the different sky conditions, of the solar irradiance (colored columns) incident at the surface in Lille, and the partition between direct flux (yellow component) and diffuse flux (blue component) over the period 2010-2022 in spring and summer, respectively. Under all-sky conditions, significant fluctuations of both the global irradiance and its direct component are observed, while the contribution of the diffuse flux remains relatively stable for both seasons (Figures 5e and 6e). In summer, measurements show in particular a difference of ~~approximately~~ 115 W/m^2 between the minimum of 2011 (307 W/m^2) and the maximum of 2022 (421 W/m^2). In spring, a similar gap of around 105 W/m^2 is also identified between the recorded minimum of 2013 (285 W/m^2) and the maximum of 2020 (389 W/m^2) mentioned earlier. These significant variations, which appear to be strongly linked to the year-to-year variability of meteorological conditions, suggest an increasing trend in all-sky solar irradiance incident at the surface in Lille in both spring and summer. Seasonal Mann-Kendall trend tests support this hypothesis, as similar increasing trends are indeed observed for both seasons, with a magnitude of approximately +4 $\pm$ 2 W/m^2/year over the period 2010-2022 (Table 4c). As the observed trends in diffuse irradiance are relatively uncertain, the overall increase in global irradiance appears to be primarily linked to a rise of the direct component, which also displays significant trends in both spring (~~+~~4.4 $\pm$ 2.3 W/m^2/year) and summer (~~+~~4.7 $\pm$ 1.9 W/m^2/year).

Our findings are consistent with the conclusions of other studies (Boers et al., 2017; Mateos et al., 2014; Sanchez-Lorenzo et al., 2013), which also observed increasing trends in surface solar irradiance for various European measurement sites, both in the presence and absence of clouds. It is also coherent with the general increase in SSI and sunshine duration observed over Europe since 1991 based on CM SAF SARAH-3 data (C3S, 2024). However, it should be noted that trends of increasing all-sky surface solar irradiance reported in the literature, which often cover longer periods (several decades) or earlier periods, are less pronounced than those highlighted in this study in Lille over the past 13 years. Apart from differences related to geographic position of the measurement sites and periods considered in each study, a possible explanation for these discrepancies is the time range used for our analysis. As mentioned~~in Section~~ previously, our analysis is based exclusively on daytime measurements, performed between [sunrise + 30 minutes; sunset - 30 minutes]. In contrast, studies from the literature usually ~~include nighttime measurements as they~~ consider irradiance measurements over a 24-hour period, which include~~. Since~~ nighttime measurements that are characterized by an absence of incident solar radiation. The~~, the~~ average over 24 hours is thus lower than when considering only daytime measurements. To put our results into perspective, we applied seasonal Mann-Kendall trend tests to the year-to-year means over the period 2010-2022 with the addition of nighttime measurements in our datasets. In this

configuration, an increasing trend in all-sky GHI is statistically significant for all seasons (even in winter), with maximum magnitudes in summer (+2.8 ± 1.1 W/m^2/year) and spring (+2.3 ± 1.0 W/m^2/year). Thus, on an annual average, a trend of about +1.5 W/m^2/year is observed, which is more in line with trends reported in the literature.

In Lille, significant increasing trends of both global and direct irradiances are also observed under CSWCclear-sun with clouds (+3.8 ± 1.2 W/m^2/year for both components) and CSKYclear-sky (+3.1 ± 1.3 W/m^2/year for both components) situations in summer (Table 4c). In spring, the trends are more uncertain, apart from a significant increase in BHI under CSWC clear-sun with clouds conditions of about +3.7 ± 1.1 W/m^2/year. Our results also highlight a significant decreasing trend in diffuse irradiance for CSKYclear-sky situations of around -0.9 ± 0.3 W/m^2/year.

The results of Heerwaarden et al. (2021), regarding spring 2020 in Cabauw, showed a significant influence of sky conditions on the variability of the measured all-sky global irradiance. It is alsothus very likely that the GHI maximum of spring 2020 in Lille, as well as the increasing trends in both spring and summer, observed in Lille under all-sky conditions, are strongly associated with the decrease of the frequency of CLOScloudy-sun conditions in favor of CSWCclear-sun with clouds and CSKYclear-sky situations, which exhibit higher radiation values, especially for the direct component of the flux. Under clear-sun with clouds and clear-sky conditions, the observed trends in irradiances could be partly related to the observed declining trends in AOD_{440}, especially the decrease of clear-sky DHI in spring. It could also be related to the evolution of water vapor content, ozone, or even simply the solar zenith angle under clear-sun conditions, which is influenced by the frequency of occurrence of the sky conditions. However, an analysis of the inter-annual variability of these various atmospheric parameters (not shown) reveals no significant trends over the period 2010-2022, neither in spring nor summer, apart from the negative trend in springtime AOD mentioned previously.

To isolate the contribution of the different parameters (occurrences of sky conditions, AOD, SZA, PWV, etc.) to the observed variabilities of the SSItrends under the different sky conditions, a more detailed analysis was conducted using irradiance measurements from ATOLL and radiative transfer simulations from SOLARTDECO, based on the methodology of the multivariate analysis presented in Section 2.4.decomposition of observed irradiance according to the classifications of the sky conditions and aerosol content introduced earlier. As presented in Section 3.2, this methodology allows for the study of trends over the period 2010-2022 and the year-to-year variability. It is worth noting that it could also be applied at other temporal resolutions, including monthly and intra-daily scales. An analysis of the direct radiative effect (DRE) of aerosols is also presented in Section 4 with a distinction of situations among clear-sun conditions.

3.2 Investigating main factors of SSI variabilityMultivariate analysis of the variability of the solar environment

TIn this section presents the results of the multivariate analysis of the variability of surface solar irradiance over the period 2010-2022, following the methodology introduced in Section 2.4. , we undertake a multivariate analysis of the variability of surface solar irradiance over the period 2010-2022. The objective is to disentangle the contributions of the change in sky's conditions (presence or absence of clouds, aerosol class and loading, atmospheric parameters) and geometrical conditions to the observed variabilities. Our analysis focuses on the specific trends and annual extrema observed over the period 2010-2022 in spring and summer, as these seasons are the most significant in terms of surface solar energy, exhibiting robust trends and

substantial yearly variations of SSI over the 13-year period. First, results of the multivariate analysis of the all-sky irradiance record of spring 2020 are presented in Section 3.2.1. Then, the analysis of the observed irradiance temporal trends in spring and summer is presented in Section 3.2.2.~~The methodology is described in Section 3.2.1. Section 3.2.2 presents the sensitivity study of the SSI to input parameters that is used to perform the multivariate analysis of the year-to-year variability of the SSI, with a focus on the all-sky irradiance record of spring 2020 presented in Section 3.2.3, and the analysis of the observed irradiance temporal trends in spring and summer presented in Section 3.2.4.~~

3.2.1 Multivariate analysis of spring 2020

The brown columns, representing SZA contributions in Figures 7, 8 and 9, were changed from hatched to plain style.

As aforementioned, the approach presented in Section 2.4.1 can be applied to the analysis of the year-to-year variability of the solar irradiance measured at the surface for all seasons, as well as to the study of the observed seasonal trends in irradiances presented in Section 3.1.2.

W~~As an example, w~~e analyze here the record-high mean GHI value of spring 2020 measured at the ATOLL platform. Spring 2020, in connection with the very particular conditions linked to COVID-19 and the associated confinement period, has ~~also~~ been the subject of numerous studies about anthropogenic pollution and air quality in France and around the world (Ordóñez et al., 2020; Reifenberg et al., 2022; Voigt et al., 2022; Cuesta et al., 2022; Petit et al., 2021; Fu et al., 2020; Velders et al., 2021), as well as about the possible impact of the reduction in anthropogenic emissions on incident solar radiation (Shuvalova et al., 2022; Reifenberg et al., 2022; Heerwaarden et al., 2021). In particular, the study of Heerwaarden et al. (2021) showed similarly high values of all-sky global irradiance in Cabauw (Netherlands), a site about 250 km north-east of Lille, who experienced the same large scale high pressure meteorological situation. The mean GHI for that spring was of 389 W/m^2, 55 W/m^2 (i.e. 16%) higher than the average springtime GHI observed in Lille over the 2010-2022 period.

Figures 7a and 7b illustrate the results obtained from our methodology for spring 2020 in Lille. Figure 7a presents the results of the decomposition of all-sky irradiance measurements in terms of sky conditions, using Equation 3, for all irradiance components. Figure 7b presents the additional decomposition of the direct irradiance component under clear-sun with clouds (ΔF_{CSWC}) and clear-sky (ΔF_{CSKY}) conditions in terms of changes in aerosol class' partition and changes in scene's parameters, as in Equations 6 and 8.

Overall, the decomposition of all-sky irradiances based on the different sky condition categories (cloudy-sun, clear-sun with clouds, and clear-sky), satisfactorily reproduces the measured differences in irradiances between the mean values of spring 2020 and the overall averages over the period 2010-2022 for all components (Figure 7a). Indeed, our approach estimates a variation of +65, +89, and -25 W/m^2 for GHI, BHI and DHI, respectively, against the measured +55, +81 and -25 W/m^2. As discussed in Section 3.1.2, spring 2020 was characterized in Lille by an exceptionally low frequency of cloudy-sun conditions (44% compared to an average of 60% in spring over 2010-2022, Figure 5a). In contrast, clear-sky conditions were more than two times more frequent, representing 34% of situations in spring 2020 compared to the spring average of 15%. This change in sky conditions lead, as shown in Figure 7a, to an increase in BHI of 74 W/m^2 (+83% of the total increase in BHI) and a decrease in DHI of -16 W/m^2 (-64% of the total change in DHI). It did result in an increase in GHI of +58 W/m^2, which represents 89 %

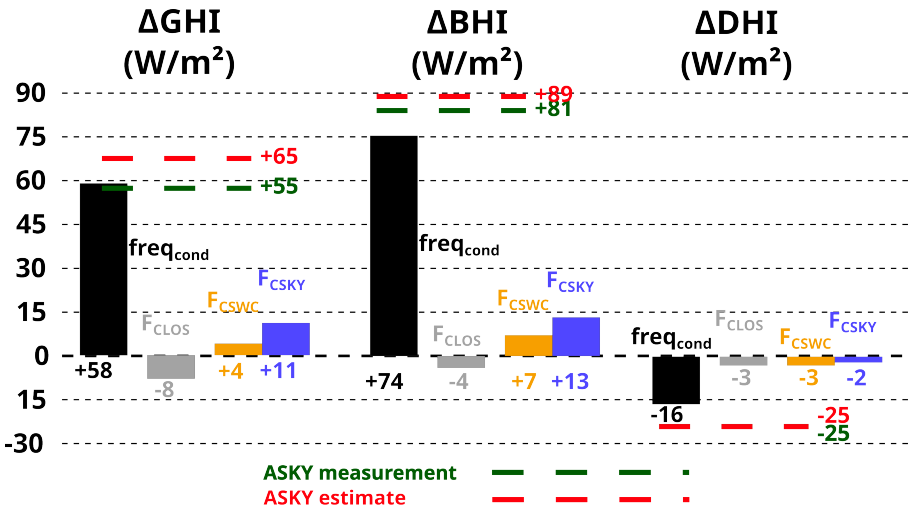

(a)

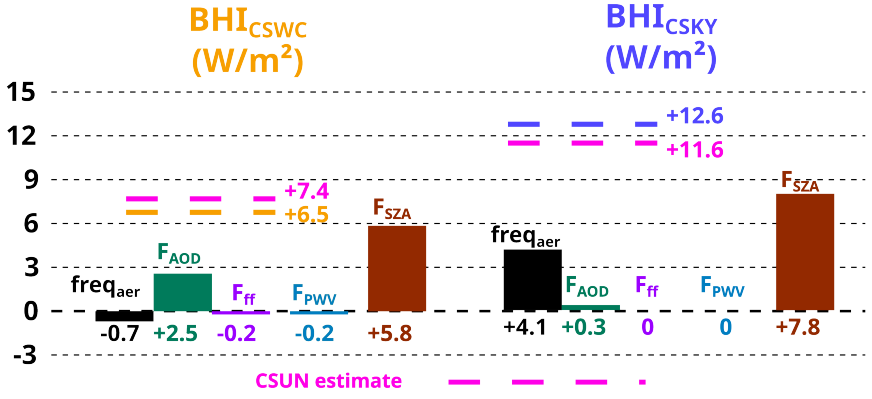

(b)

Figure 7. Illustration of the decomposition for spring 2020 : (a) of the all-sky SSI components~~irradiances~~ (GHI, BHI, and DHI), and (b) of the direct component (BHI) in clear-sun with clouds and clear-sky conditions. In Figure (a), the green dashed lines represent the observed deviation from the 2010-2022 spring average for spring 2020. The red dashed lines correspond to the deviation derived from the decomposition based on the sky conditions. The decomposition is represented by the black, gray, orange, and blue colored columns, which respectively correspond to the contributions of the variability in the frequency of occurrence of sky conditions ($freq_{cond}$) and the intrinsic variability of the irradiances in CLOS (F_{CLOS}), CSWC (F_{CSWC}), and CSKY (F_{CSKY}) conditions. The additional decomposition of BHI_{CSWC} and BHI_{CSKY} with respect to the scene's parameters is illustrated in panel (b). The orange and blue columns from panel (a), which represent the intrinsic variability of the BHI under CSWC and CSKY conditions, respectively, are represented as dashed lines of the same color in panel (b)~~The orange and blue dashed lines represent the intrinsic variability of the BHI under CSWC (orange column from panel (a)) and CSKY (blue column from panel (a)) conditions, respectively, derived from the decomposition based on the sky conditions~~. The pink dashed lines represent the values estimated from the decomposition of the BHI according to the scene's parameters as in Equation 6. The latter decomposition is also illustrated by the colored columns, which represent the contributions of the variability in the frequency of occurrence of aerosol classes ($freq_{aer}$, black column), as well as the variability of the AOD (green column), ff (violet column), PWV (blue column), and SZA (brown column).

of the total increase of GHI. Our approach also estimates that the remaining contribution (of only +7 W/m^2, +11% of GHI's change) comes mostly from changes in BHI resulting from partially opposite in sign effects, with fewer cloudy-sun situations being less bright at the surface ($F_{CLOS} = -8$ W/m^2), more clear-sky situations being brighter ($F_{CSKY} = +11$ W/m^2), and clear-sun with clouds being slightly brighter (F_{CSWC}=+4 W/m^2).

The results of the decomposition of the changes in BHI under clear sun situations (CSUN, i.e. the sum of CSWC and CSKY) related to changes in aerosol classes and scene's parameters, illustrated in Figure 7b, provide more insight into the remaining +17 % increase of BHI beside the effects of the change in sky situations. They suggest that most of the increase due to change in scene's parameters is due to a decrease in SZA for CSUN situations (-1.5° and -0.9° in CSKY and CSWC situations respectively), that by itself causes an increase of around +14.6 W/m^2, which represents 71 % of the overall increase in BHI under clear-sun conditions. The remaining 29 % comes mostly from a change in aerosol properties. In CSWC situations, increase of BHI due to SZA is three times higher than the increase due to a change in aerosol properties (linked with an average AOD of 0.16 in 2020 compared to the 2010-2022 average of 0.22). In CSKY situation, the modification of aerosol class frequencies (significant decrease in the occurrence of the Continental Polluted class in favor of the Continental class, see Figure 5d) is the main aerosol-related effect that results in a contribution of +4.1 W/m^2, which is around slightly more than half of that due to changes in SZA (+7.88 W/m^2).

Our estimates are consistent with the results of Heerwaarden et al. (2021) that analysed that the observed irradiance record of spring 2020 in Cabauw is primarily due to the exceptionally low cloud fraction that year (contribution of approximately 89%) with modest additional contributions of changes in AOD (6%) and water vapor content (5%). Indeed, our analysis attributes a 89% increase of all-sky GHI to the change in sky condition occurrences, which are also responsible for 83% of the BHI increase and 64% of the DHI increase. In addition, our results emphasize the predominant role of the SZA compared to aerosol changes for that season. We did not evaluate CLOS situations in the present study, that show a slight decrease of GHI, BHI and DHI. However, we observe a slight increase of the SZA under CLOS situations, which might contribute to this general decrease of SSI in CLOS situations.~~Note that the variability of the mean SZA under clear-sun conditions could partly explain the decrease in both direct and diffuse irradiances estimated for cloudy-sun situations. Indeed, a decrease in SZA for CSUN situations implies an increase in SZA for opposing situations (i.e. CLOS conditions), potentially resulting in lower irradiance values for cloudy-sun conditions of spring 2020 compared to the average observed in spring over the period 2010-2022. It is important to emphasize that all parameters considered here also play a role in cloudy-sun conditions. Since these situations have not been evaluated in the present study, the results presented here may underestimate (or overestimate) the overall impact of each parameter. Nonetheless our estimates are consistent with the results of Heerwaarden et al. (2021), which suggests that the observed irradiance record of spring 2020 in Cabauw is primarily due to the exceptionally low cloud fraction that year (contribution of approximately also 89%) with modest additional contributions of changes in AOD (6%) and water vapor content (5%).~~

Our methodology was also used to explain the variability of irradiances for other years in spring and summer. Our analysis highlighted again the primary influence of the variability of the sky conditions, which also explain, for example, 69% and 84% of the variability of the all-sky GHI observed during the summer of 2022 (maximum of 421 W/m^2) and spring 2013

(minimum of 285 W/m^2), respectively. It showed also ~~again~~ the primary importance of SZA, associated with the variations of the occurrences of the sky conditions, which plays a key role in the variability of the irradiances for other years, while the influence of the variability of both aerosol and water vapor contents are relatively limited. These results are consistent with the order of importance of the parameters determined by the sensitivity analysis in Section 2.4.2.

3.2.2 Multivariate analysis of spring and summer trends

As stated in Section 3.1.2 and Table 4c, all-sky GHI irradiances show significant positive trends in spring and summer with respective magnitudes of +4.0 $\pm$ 1.9 W/m^2/year and +4.2 $\pm$ 1.9 W/m^2/year, due to an important increase of the direct component, with magnitudes of +4.4 $\pm$ 2.3 and +4.7 $\pm$ 1.9 W/m^2/year in spring and summer, respectively. Figures 8a and 8b illustrate the results of these trends' decomposition obtained from Equation 4.

The decomposition of the trends shows similar features in spring and summer. The observed upward trends in all-sky GHI and BHI are largely linked to the trends in the occurrence of sky conditions, with contributions in spring of approximately +2.7 (71%) and +3.3 (79%) W/m^2/year for the global and direct components, respectively, and +2.6 (62%) and +3.4 (74%) W/m^2/year in summer. These results are consistent with the negative trends in the frequencies of CLOS~~cloudy-sun~~ situations observed for both seasons, in almost equal favor of CSWC~~clear-sun with clouds~~ and CSKY~~clear-sky~~ situations (Table 4c). The remaining contributions in the GHI and BHI upward trends arise from almost only positive irradiance trends observed under the various sky conditions. The most important contribution ~~among irradiance trends~~ comes from CSWC conditions (approx. +0.8-0.9 W/m^2/year for both components), which align with the significant positive trends observed for these situations (Table 4c) and their relatively high seasonal frequencies ~~associated~~ (25% in spring, 22% in summer). The statistical significance of these trends and the similarities between observed and derived all-sky GHI and BHI trends further validate these conclusions.

We further analyze the BHI variability in CSWC and CSKY conditions, for spring and summer, decomposing their trends following Equations 7 and 9. Note that apart from the CSKY BHI trend in summer (where no parameter trends are significant), the computed trends generally yield results similar to the observed trends, with magnitudes within the uncertainty of the observations ($\pm\sigma$). The significant trends observed for CSWC BHI in spring (+3.7 $\pm$ 1.7 W/m^2/year) and summer (+3.8 $\pm$ 1.2 W/m^2/year), that contribute to the all-sky BHI trends by +0.85 and +0.91 W/m^2/year, can be decomposed as in Figures 9a and 9b. It shows that the main contribution to these trends in spring are related to changes in aerosol loading, through variations in aerosol class' frequencies (+0.21 W/m^2) and increase of AOD (+0.35 W/m^2) that explain 87 % of the CSWC BHI trend, while changes in SZA for those situations account for around 14 % of the CSWC BHI trend. These results align with the significant trends observed for both AOD and aerosol class frequencies in spring (Table 4b). In summer, the contribution of~~due to~~ aerosol properties is smaller, 49 %, while the contribution from changes in SZA does reach 44 %. Hence, although the trends in BHI in CSWC situations are very close in magnitude in spring and summer, the contribution of the different parameters are quite different for both seasons. It results from a decrease of AOD more than two times larger in spring compared to summer (see Table 4b), and a decrease in SZA three time smaller in spring (-0.03 $\pm$ 0.09 degrees/year, confidence of 62 %) than in summer (-0.094 $\pm$ 0.09 degrees/year, confidence of 80 %). The contribution of the SZA variability is thus not to be neglected. Beside its effects on CSWC BHI, it also explains the limited CSKY BHI trend in spring, as the effects of the AOD decrease is

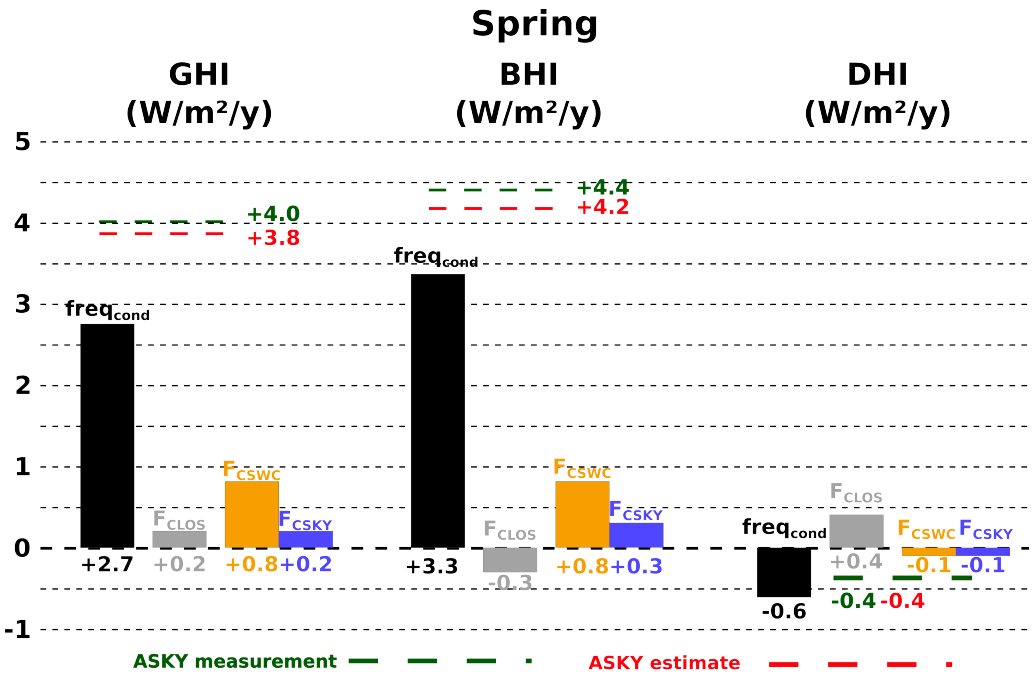

(a)

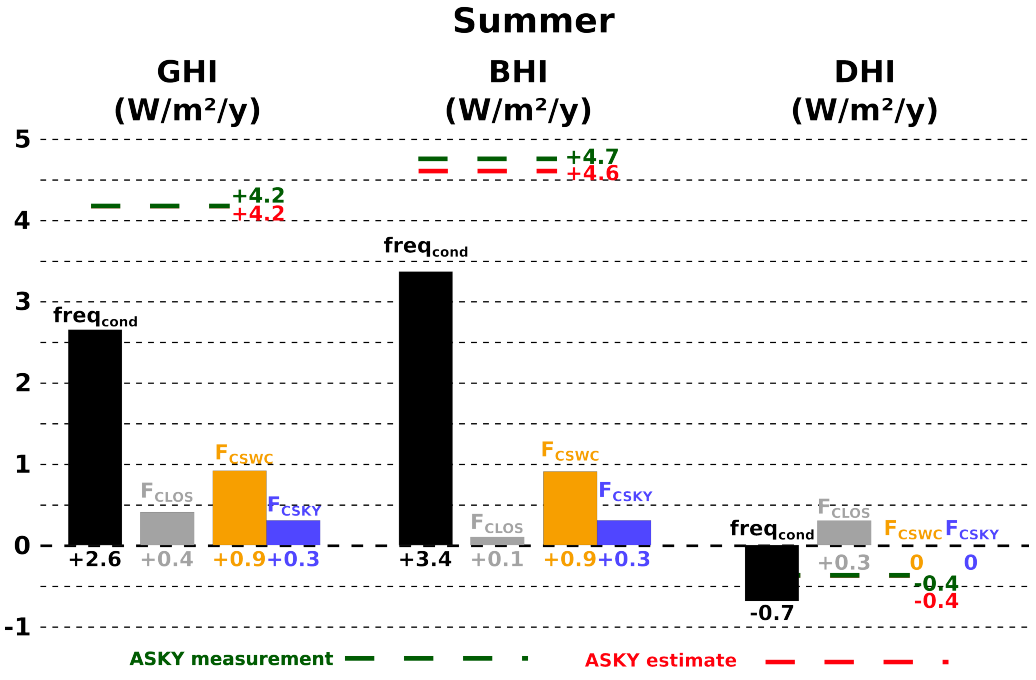

(b)

Figure 8. Decomposition of the observed trends in all-sky SSI components (from left to right, global, direct, and diffuse)~~irradiances~~ (a) in spring and (b) in summer. The meaning of the colored lines and columns is similar to that described in Figure 7a.

compensated by an increase in SZA (+0.04 ± 0.14 degrees/year, confidence of 52 %). Furthermore, changes in SZA (-0.1 ± 0.09 degrees/year, confidence of 80 %) represent almost the sole contribution to the CSKY BHI trend in summer (Figure 9).

Finally, it is worth noting that the influence of the other atmospheric parameters remains relatively limited, even for the water vapor content whose contribution is maximum for both seasons in clear-sun with clouds conditions, but is limited to +3% and +6% in spring and summer, respectively.

4 Radiative effects of atmospheric components on SSI~~Direct radiative effects (DRE) in Lille over 2010 - 2022~~

~~In this section, we study the radiative impact of atmospheric components in the solar domain over the period 2010-2022, focusing on clear sun situations. The objective here is to compute the direct radiative impact of aerosols in clear sky situations, and to analyse the overall effects of atmospheric components in clear-sun-with cloud situations.~~

In this section~~Here~~, we ~~chose instead to~~ assess atmospheric components', especially aerosols, ~~the direct (non-net)~~ radiative effects ~~of aerosols~~ on the downwelling surface solar irradiances ~~incident at the surface~~ (called RE_d for **R**adiative **E**ffect on the **d**ownwelling SSI), consistently with our ground-based dataset, and in relevance for surface related applications (such as photovoltaic solar systems) and surface processes (e.g. photosynthesis). Note that only a few studies have assessed the direct radiative impact of aerosols specifically on downward surface solar radiation, as for example done in Papadimas et al. (2012) over the Mediterranean basin. Furthermore, our approach encompasses the shortwave radiative effects of atmospheric particles on both global (GHI), direct (BHI) and diffuse (DHI) components of the downwelling SSI, as in Witthuhn et al. (2021). ~~It is consistent as our study is based on measurement of the downwelling surface irradiance and it allows a direct assessment of the aerosols and clouds' direct impact on the solar source exploited by surface processes (e.g. photosynthesis) and solar applications (thermal or photovoltaic solar systems). Numerous studies in the literature have assessed the direct radiative impact of aerosols, both globally (Yu et al., 2006; Bellouin et al., 2013; Thorsen et al., 2020; Kinne, 2019; Zhou et al., 2005) and regionally (Papadimas et al., 2012; Nabat et al., 2014; Witthuhn et al., 2021; Bartók, 2017; Neher et al., 2019). Most of these studies focus on the net radiative impact of aerosols, which is the difference between net radiation incident at the surface (i.e. the difference between downwelling and upwelling solar flux) in the presence and absence of aerosols. It is to be noticed that compared to most existing studies about the surface DRE of aerosols, we analyze here the effect of aerosols on both the direct and diffuse components of the solar irradiance.~~ I~~Our analysis of the direct radiative effects is initiated i~~n Section 4.1 our analysis of the RE_d focuses~~with a focus~~ on clear-sky conditions, through a statistical investigation of the aerosol ~~mean~~ radiative~~direct~~ effects on all downwelling SSI components (GHI, BHI, DHI) over the whole period 2010-2022 ~~(Section 4.1.1)~~. ~~It is complemented with an additional analysis of specific case studies (Section 4.1.2) that provides more insight on invariant and distinctive aerosol effects.~~ In addition, Section 4.2 provides an analysis of aerosols and clouds' radiative effects in CSWC conditions. This approach relies on two sets of pristine (i.e. aerosol-and-cloud free) and cloud-free simulations, which by comparison with ground-based measurements that include the effect of clouds on SSI, allow the quantification of aerosols and clouds' RE_d in CSWC conditions. Finally, the respective and cumulative RE_d of clouds (on DHI) and aerosols (on DHI and BHI) can be quantified over all CSUN (CSKY and CSWC) situations, that represent on average 33% of sky conditions in

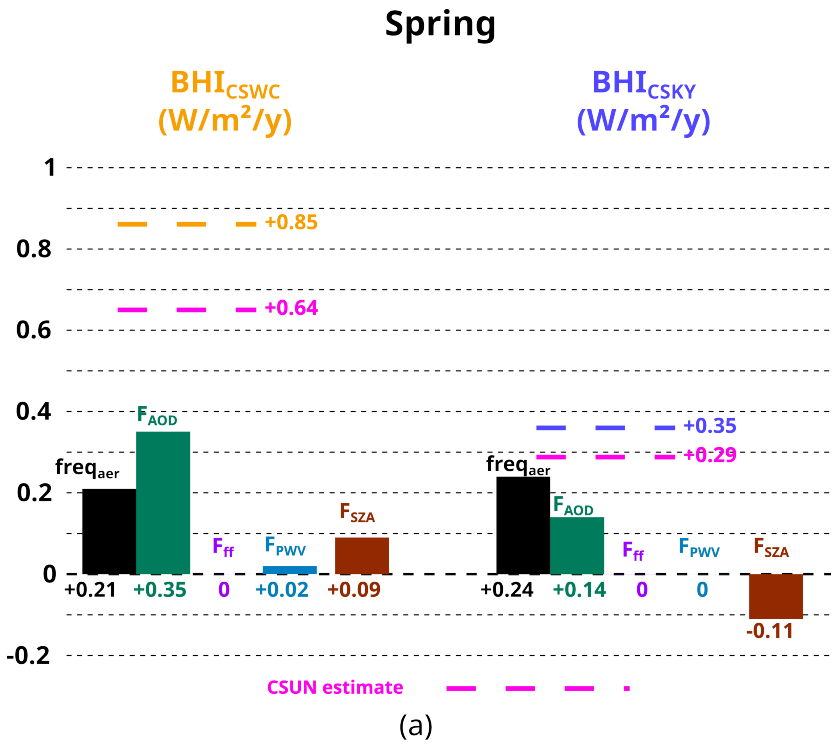

(a)

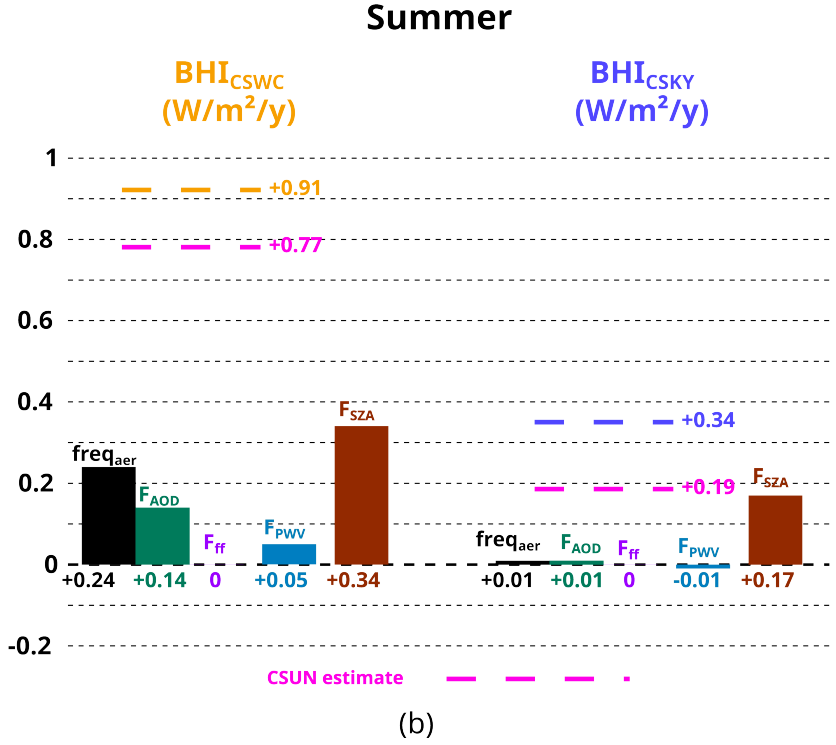

(b)

Figure 9. Illustration of the decomposition of observed trends in the direct component of SSI (BHI) under clear-sun with clouds and clear-sky conditions (a) in spring and (b) in summer. The meaning of the colored lines and columns is similar to that described in Figure 7b.

Lille.~~where both aerosols and clouds acts on the diffuse component of SSI. These situations are particularly interesting as their occurrence is important (twice the occurrence of clear sky situations), and as on average, irradiance levels are strong with both a high direct irradiance and an exceptional level of diffuse irradiance. In addition to the masks allowing their identification, the radiative transfer simulations in aerosol-and-cloud free and in cloud-free situations allow a statistical analysis of the direct radiative effects of atmospheric particles and their cumulative effects.~~

4.1 Clear-sky conditions~~Aerosol DRE in clear-sky conditions~~

In clear-sky conditions, t~~T~~he ~~direct~~ radiative effect on the downwelling SSI (RE_d)~~(DRE)~~ of aerosols is defined as:

$$\mathrm{RE}_{d,\ aer,\ CSKY} = F_{meas} - F_{pristine} \tag{12}$$

or in relative terms :

$$\mathrm{rRE}_{d,\ aer,\ CSKY} = \frac{F_{meas} - F_{pristine}}{F_{pristine}} \tag{13}$$

where $F_{pristine}$ and F_{meas} correspond respectively to the pristine (aerosol-and-cloud free) simulations of~~by~~ SOLARTDECO and to the ATOLL measurements of the downwelling solar irradiance components (GHI, BHI or DHI) in clear-sky conditions. The radiative effect efficiency of aerosols on the downwelling SSI (REE_d)~~Direct Radiative Effect Efficiency (DREE) of aerosol~~ under clear-sky conditions, defined as :

$$\mathrm{REE}_{d,\ aer,\ CSKY} = \frac{\mathrm{RE}_{d,\ aer,\ CSKY}}{\mathrm{AOD}_{440}} \tag{14}$$

is also investigated in this section, as it allows the comparison of the RE_d~~DRE~~ for different aerosol loads (see for example Kok et al. (2017)). Furthermore, as~~As~~ the RE_d~~DRE~~ is approximately linear with AOD (Satheesh and Ramanathan, 2000), REE_d ~~DREE~~ provides the sensitivity of RE_d~~DRE~~ to AOD. ~~An additional analysis of the direct radiative effect of aerosols is carried out in Section 4.1.2 for some case studies that are typically observed in Lille, to better appreciate the variations of the direct radiative effects of natural and anthropogenic particulate pollution.~~

The mean ~~direct~~ radiative effect of aerosols in Lille is investigated over the whole period 2010 - 2022. Results are analyzed by season, by aerosol class, and also by distinguishing clean ($\mathrm{AOD}_{440} \leq 0.1$) and polluted ($\mathrm{AOD}_{440} > 0.1$) situations. Table 5 provides the mean absolute and relative RE_d~~DRE~~ of aerosols along with the corresponding REE_d~~DREE~~ for all coincident CSKY measurements, and for the three components of the ~~surface solar irradiance (~~SSI~~)~~.

Our results show that, in Lille, over the period 2010-2022, the overall yearly-averaged radiative impact of aerosols constitute a loss of around -61 W/m^2 (-18%) of direct irradiance, and a gain of roughly +42 W/m^2 (+92%) of diffuse radiation, compared to pristine conditions. This leads to an important modification of the DHI contribution with a twofold (+105 %) increase of the average DHI/GHI ratio from 12 % in pristine conditions to an average of 24 % in CSKY conditions. The opposite-in-sign aerosol effects on BHI and DHI leads to a reduced effect of GHI, evidently always negative, which is on average reduced by about 20 W/m^2 (-5.5 %). During polluted CSKY situations, which happen 73 % of the time, the aerosol RE_d~~DRE~~ exceeds -20 % and +100% for BHI and DHI, and -6 % for GHI. Inversely, for clean situations, that mostly happen~~d~~ in fall and winter, the

aerosol RE_d~~DRE~~ is weaker and smaller in magnitude than -10 % and +50% for BHI and DHI, and -3 % for GHI, i.e. two time smaller than~~t~~ in polluted situations. The compensation mechanism between the RE_d~~DRE~~ on direct and diffuse irradiances shows, through the values of REE_d~~DREE~~, some aerosol-independent feature, with direct and diffuse components that are respectively about~~more or less~~ three ~~times~~ and two times ~~respectively~~more sensitive to the AOD than the GHI.

RE_d**~~DRE~~ of aerosols in CSKY conditions in Lille (2010- 2022)** (W/m^2) [%] <$\frac{W/m^2}{unit\ of\ AOD_{440}}$>			
	GHI	**BHI**	**DHI**
Total	(-19.7) [-5.5] <-125>	(-61.4) [-17.5] <-379>	(41.7) [91.7] <254>
Winter	(-15.6) [-6.4] <-158>	(-37.9) [-18.3] <-386>	(22.3) [59.8] <227>
Spring	(-21.4) [-5.9] <-116>	(-68.3) [-19.1] <-377>	(46.8) [101.7] <261>
Summer	(-18.8) [-4.8] <-120>	(-62.7) [-16.4] <-376>	(43.9) [93.5] <256>
Autumn	(-19.2) [-5.5] <-139>	(-53.7) [-15.9] <-385>	(34.5) [80.2] <245>
Continental	(-15.0) [-4.0] <-129>	(-43.2) [-11.7] <-362>	(28.2) [61.5] <233>
Continental polluted	(-31.6) [-8.7] <-105>	(-98.6) [-27.5] <-326>	(67.0) [144.4] <221>
Mixed	(-22.3) [-6.2] <-120>	(-73.8) [-21.2] <-396>	(51.5) [112.6] <276>
Maritime	(-11.5) [-4.2] <-152>	(-36.2) [-14.7] <-463>	(24.7) [61.3] <311>
Desert dusts	(-25.4) [-6.2] <-126>	(-92.1) [-21.2] <-456>	(66.7) [149.3] <330>
Clean	(-10.5) [-2.9] <-144>	(-30.1) [-9.2] <-403>	(19.6) [45.8] <259>
Polluted	(-23.2) [-6.4] <-118>	(-73.5) [-20.7] <-369>	(50.2) [109.5] <252>

Table 5. Mean (absolute) and [relative] aerosol RE_d~~Direct Radiative Effects (DRE)~~ and associated absolute efficiencies (REE_d~~DREE~~) on SSI in clear-sky conditions in Lille over the period 2010 - 2022 for coincident AERONET measurements only. The instantaneous values were computed using ATOLL irradiance measurements and SOLARTDECO pristine simulations for all irradiance components. The "total" mean corresponds to the overall mean RE_d~~DRE~~ and REE_d~~DREE~~ for all coincident measurements in clear-sky conditions over the period 2010 - 2022. Similar averages were made for each season as well as for the different classes and for clean ($AOD_{440} \leq 0.1$) and polluted conditions.

The analysis of the RE_d~~DRE~~ indicates that the maximum ~~direct~~ radiative impact happens both in absolute (-21/-68/+47 W/m^2) and relative (-6/-19/+102 %) terms in spring, with slightly higher values compared to summer (-19/-63/+44 W/m^2; -5/-16/+94 %), and also for continental polluted aerosols (-32/-99/+67 W/m^2, -9/-28/144 %). This result is consistent with our analysis of the seasonal variability of the solar environment in Lille, which shows higher values of AOD in spring than in summer (Figure 4b), and a high proportion of continental polluted aerosol in spring. The minimum ~~direct~~ radiative impact occurs in absolute values in winter (-16/-38/+22 W/m^2) and for maritime aerosols (-12/-36/+25 W/m^2). This result is also consistent with the observed lower values of AOD in winter and higher proportion of maritime aerosols during this season. It can also be related to higher ~~lower~~ solar zenith angles~~SZA~~ that lead to overall lower surface irradiances in winter, and thus lower aerosol RE_d in absolute values.

The RE_d~~DRE~~ efficiency (REE_d~~DREE~~) is higher in magnitude for Maritime and Desert Dust aerosols, with values above -450 W/m^2 and +310 W/m^2 for BHI and DHI, respectively. These results align with the conclusions of the sensitivity analysis (Section 2.4.2), which shows higher sensitivities of the direct and diffuse components to Maritime and Desert dust aerosols. As already hypothesized, this result may be linked to the differences in the size of the particles, as lower absolute value of Angström exponent for large particles imply higher extinction properties over the whole solar spectrum. Note that, on average, the radiative impact of the Maritime and Desert dust classes remains however relatively limited over the course of the year, as these two classes represent only 14% and 5% of observed situations, respectively. Moreover, although the Maritime class exhibits large REE_d~~DREE~~, the corresponding RE_d~~DRE~~ values remain relatively small due to low corresponding aerosol optical depths. Therefore, the radiative impact of aerosols in clear-sky conditions is largely dominated by the Continental, Continental polluted, and Mixed classes, which represent 38%, 20%, and 22% of situations in Lille, respectively.

Section 4.1.2 was removed.

4.2 Clear-sun with clouds conditions~~DRE in clear-sun-with-cloud conditions~~

In clear-sun with cloud conditions, the overall particles RE_d~~DRE~~ on the direct SSI component is only related to aerosols. On the contrary, due to the presence of clouds off the sun's direction, their effects on the diffuse component is more complex, with contributions of both aerosols and clouds.

Their respective effects on the SSI's diffuse component can generally not be separated. They are scene-dependent, and vary significantly with the cloud cover, notably the cloud fraction and the cloud opacities, even with the angular distance of the cloud cells to the sun direction or the vertical profile of aerosols relative to clouds. Undoubtedly, aerosol RE_d~~DRE~~ on the diffuse SSI is minimal (resp. maximal) when the cloud fraction is high (resp. low). It is in any case out of the scope of the current study to ambition a complete distinction or disentangling of aerosols versus clouds RE_d~~DRE~~ in CSWC situations.
The radiative effects of all atmospheric particles, hydrometeors and aerosols, lead to an overall RE_d~~DRE~~ ($RE_{d,\ all}$) that can be decomposed as:

$$RE_{d,\ all} = F_{meas} - F_{pristine} = F_{meas} - F_{csky} + F_{csky} - F_{pristine} \tag{15}$$

$F_{meas} - F_{csky}$ is by definition the cloud's RE_d~~DRE~~, i.e. the difference between the downwelling solar irradiance actually measured and due to the overall effects of all atmospheric components (gas, aerosol and clouds), and the incoming radiation in the same conditions without clouds (i.e. clear-sky). In the solar direction, $F_{csky} - F_{pristine}$ equals the aerosol RE_d~~DRE~~. However it is not the case concerning the diffuse SSI component. $F_{csky} - F_{pristine}$ is rather the radiation one would have compared to the pristine case if no clouds were present. Yet, in the rest of this section, $F_{csky} - F_{pristine}$ is named as in section 4.1 aerosol RE_d~~DRE~~, and is written as $F_{aer} - F_{pristine}$. Due the presence of clouds, F_{aer} is obtained from SOLARTDECO clear-sky simulations.

The motivation to analyse $F_{aer} - F_{pristine}$ is to appreciate the difference in aerosol RE_d~~DRE~~ between CSKY and CSWC situations, and the radiative "compensation" between cloud and aerosol RE_d~~DRE~~ in CSWC situations. Table 6 provides the

mean absolute and relative values of $F_{aer} - F_{pristine}$ in CSWC situations over the period 2010-2022. Values of RE_d~~DRE~~ are 15 to 20 % higher than in CSKY given in Table 5. This discrepancy is related to the slightly higher AOD_{440} values observed in CSWC conditions (0.19) compared to CSKY conditions (0.17), as well as to slightly lower SZA values (60° on average in CSWC against 62° in CSKY conditions), which lead to higher irradiance values, and thus greater absolute radiative effects. Note that REE_ds~~DREEs~~ are slightly greater than under clear-sky conditions, by about 30 W/m^2/unit of AOD for all irradiance components. This result is consistent with the effects of lower solar zenith angles and with the observation that aerosol Ångström exponent are on average slightly lower (by 0.06) in CSWC situations compared with CSKY cases, leading to a higher RE_d~~DRE~~ efficiency ~~as illustrated on Figure 10f~~. Note that the study of CSWC situations allows us to analyze conditions characterized by the Strong events class (see Table 2), which were not identified as clear-sky either because of the presence of clouds or because of their high AOD values, as the clear-sky filter used in this study tends to erroneously misidentify CSKY conditions when the AOD is high (Liu et al., 2021). The aerosol RE_d~~DRE~~ for the Strong events class appears very substantial for both direct (-260 W/m^2, i.e. -50%) and diffuse (+190 W/m^2, i.e. +381%) components, leading to a relatively important reduction of the GHI of about -70 W/m^2 (-13%) on average. The climatological impact of the Strong events class is however

RE_d~~DRE~~ of aerosols in CSWC conditions in Lille (2010- 2022) (W/m^2) [%] <$\frac{W/m^2}{unit\ of\ AOD_{440}}$>			
	GHI	**BHI**	**DHI**
Total	(-21.2) [-6.0] <-126>	(-71.6) [-20.0] <-411>	(50.4) [108.1] <285>
Winter	(-17.2) [-6.5] <-158>	(-45.4) [-19.3] <-413>	(28.1) [71.7] <254>
Spring	(-24.2) [-6.2] <-121>	(-84.1) [-21.4] <-414>	(59.8) [125.4] <293>
Summer	(-20.6) [-5.1] <-110>	(-76.9) [-18.4] <-405>	(56.3) [115.0] <296>
Autumn	(-20.3) [-6.6] <-139>	(-62.2) [-21.2] <-417>	(41.9) [96.0] <277>
Continental	(-14.5) [-4.1] <-121>	(-45.4) [-12.9] <-372>	(30.9) [66.7] <252>
Continental polluted	(-31.3) [-8.0] <-91>	(-111.6) [-27.6] <-328>	(80.3) [165.8] <237>
Mixed	(-22.1) [-6.3] <-110>	(-78.4) [-21.9] <-395>	(56.3) [120.6] <284>
Maritime	(-16.5) [-5.5] <-198>	(-48.2) [-17.2] <-582>	(31.7) [74.5] <383>
Desert dusts	(-28.8) [-8.5] <-145>	(-103.1) [-30.6] <-517>	(74.3) [163.2] <372>
Strong events	(-70.2) [-12.8] <-76>	(-260.3) [-50.5] <-284>	(190.2) [381.1] <208>
Clean	(-12.3) [-4.0] <-163>	(-36.7) [-12.4] <-484>	(24.4) [56.2] <321>
Polluted	(-24.3) [-6.7] <-113>	(-83.8) [-22.7] <-386>	(59.5) [126.3] <273>

Table 6. Mean (absolute) and [relative] aerosol RE_d~~'DRE'~~, and REE_d~~DREE~~, on SSI over the period 2010 - 2022 in Lille under clear-sun with clouds conditions. Due to the presence of clouds in the sky, the instantaneous values are not based on ATOLL irradiance measurements but rather computed using SOLARTDECO clear-sky simulations with as inputs aerosol properties issued from AERONET measurements.

relatively limited as these situations only represent about 0.3% of the situations observed in Lille over the period 2010-2022.

As mentioned previously~~above~~, the overall ~~direct~~ radiative effect of atmospheric components in CSWC conditions is obtained from the difference between measurements and pristine-like simulations, and is the result~~s of~~~~from~~ combined and compensating effects of both aerosols and clouds. Calculations of mean $F_{aer} - F_{pristine}$, $\mathrm{RE}_{d,\ cloud,\ CSWC}$, and $\mathrm{RE}_{d,\ all\ CSWC}$ over 2010-2022, per season and aerosol situations are synthesized in Figure 10. The ~~direct~~ radiative effects of all atmospheric

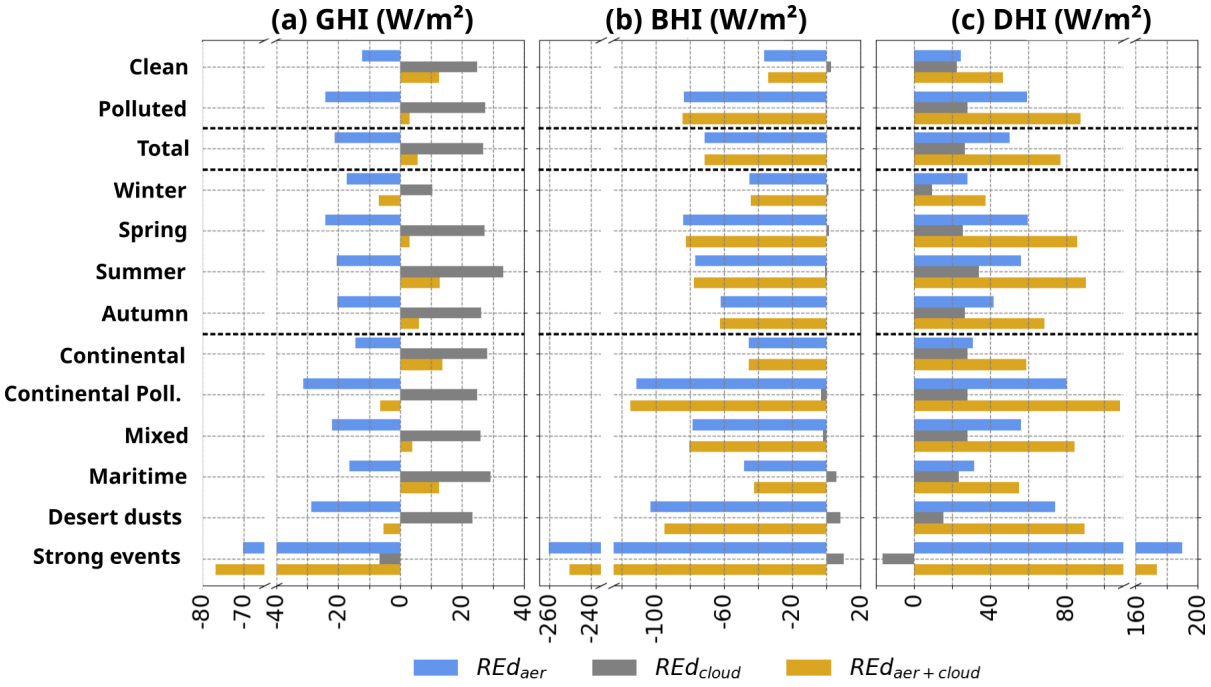

Figure 10. Mean RE_d on SSI~~Direct radiative effects~~, under CSWC conditions, of aerosols and clouds combined (yellow), clouds (gray), and cloud free RE_d~~DRE~~ of aerosols (blue), on SSI for (a) the global (GHI)~~irradiance~~, (b) the direct (BHI)~~irradiance~~, and (c) the diffuse (DHI) components~~irradiance~~ over the period 2010-2022. Points considered as the ones coincident AERONET measurements. Instantaneous values are calculated using ATOLL SSI~~irradiance~~ measurements and SOLARTDECO clear-sky simulations with and without aerosols. As in Table 5, the "total" averages correspond to the overall mean RE_d~~DRE~~ over the period 2010-2022.

particles (aerosols and clouds) are represented in yellow in Figure 10, and those of clouds only are in grey. The RE_d~~DRE~~ of aerosols one would have in cloud-free situations is in blue and corresponds to the values in Table 6.

As expected, $\mathrm{RE}_{d,\ cloud,\ CSWC}$ for the direct SSI component is close to zero (with an accuracy of $\pm 1\,\mathrm{W.m^{-2}}$), which is coherent with the absence of clouds in the sun's direction. This result further validates the performance of both the CSWC filtering and our clear sky radiative transfer simulations (for most of the cases except for desert dust and strong event situations where small residuals exist).

In the case of clean situations (AOD < 0.1), clouds contribute to an increase in DHI of around +22 W/m^2 (gray column, Figure 10c), comparable to the contribution of aerosols alone (+24 W/m^2, blue column). In these conditions, the decrease in BHI due to aerosols (-37 W/m^2, Figure 10b) is overcompensated by the cumulative impact of both aerosols and clouds on the DHI, leading to GHI values greater by about +13 W/m^2 (yellow column, Figure 10a) than under ~~quasi-~~pristine-like conditions (without aerosols and clouds). For polluted situations characterized by higher aerosol loads (AOD $\geq$ 0.1), which are more frequent, the cumulative effect of clouds and aerosols result in a GHI greater by +3 W/m^2 to the pristine situations. The cloud contribution on DHI, +28 W/m^2, is slightly higher than for clean situations while the aerosol "cloud-free" contribution on BHI and DHI is significantly higher. If one consider all CSWC situations, clouds add on average 25 W/m^2 compared to cloud-free atmospheres, i.e. half of the aerosol cloud-free RE_d~~DRE~~ on the diffuse component. Cloud RE_d~~DRE~~ is even higher than 50 W/m^2 twenty percents of the time. As a consequence, the mean observed GHI in CSWC situations is close to pristine conditions, or even slightly above by +4 W/m^2 (Figure 10a). The corresponding proportions of direct and diffuse irradiances are however in this case very different, with an average decrease of about -20% in BHI and an increase of +164% in DHI compared to pristine-like conditions. The DHI proportion in the presence of clouds and aerosols under CSWC conditions (25%) is thus on average much~~27%~~ higher than under pristine conditions (10%, i.e. cloud-free and aerosol-free).

The seasonal distinction reveals that the global RE_d~~DRE~~ of particles is maximal in absolute values (resp. relative) in summer (resp. autumn) with +12.7 W/m^2 (resp. +0.9%) above the pristine level. In spring, the global RE_d~~DRE~~ is lower due to higher aerosol RE_d~~DRE~~, but remains positive (+3 W/m^2). In contrast, despite a weaker radiative impact of aerosols in winter, the corresponding effect of clouds is so small (+10 W/m^2, i.e., three times less than the effect of aerosols, Figure 10c) that the reduction of the BHI by aerosols is not fully compensated, with average GHI values lower than under pristine-like conditions by about -7 W/m^2 (Figure 10a). Similar results are observed for the Continental polluted, Desert dust, and Strong events classes, with a decrease in GHI compared to pristine-like conditions of about -6, -5, and -77 W/m^2, respectively. In contrast, for maritime and continental conditions, characterized by lower aerosol loads, the combined RE_d~~DRE~~ of aerosols and clouds remains positive. ~~It should be noted that for conditions identified as CSWC at times where AERONET's algorithm fails to deliver information about aerosols, certainly due to the presence of some thin clouds or varying-in-time conditions, the overall GHI is again on the same order as for pristine conditions and the cloud RE_d on GHI is of around 20 W/m^2, but it results from compensating effects of clouds on the direct irradiance (-25 W/m^2, i.e. -7%), and on the diffuse irradiance (+45 W/m^2, +44%).~~ In summary, these results highlight the importance of clouds in CSWC situations that cause a significant enhancement effect on the diffuse irradiance field. For these situations that occur 22% of the time, the mean GHI level is comparable to pristine-like conditions (difference is +4 W/m^2). The SSI is even higher than in pristine conditions during clean, summer, or continental-aerosol moments with an average increase in solar radiation of up to 13 W/m^2. Clouds add on average between 20 and 30 W/m^2, depending on the situations, and overall on average around 25 W/m^2 compared with atmospheres that would be cloud-free. Hence, they not only substantially increase the level of GHI but also modify the direct/diffuse partition of the SSI, increasing by +4% (21 to 25%) the diffuse proportion compared to the cloud-free atmosphere. Overall, the combined effects of aerosols and clouds leads to an increase of the DHI proportion of~~, and by~~ +15% ~~(10 to 25%)~~ compared to the pristine atmosphere (from

10 to 25%).

Finally, m~~M~~ean ~~direct~~ radiative effects can also be computed considering all~~over~~ clear-sun situations, i.e. the sum of CSKY and CSWC situations, that represent on average 33 % of the situations per year over 2010-2022. These RE_ds~~DREs~~ write as the sum of the RE_d~~DRE~~ per sky conditions weighted by their respective occurrences, keeping in mind that the RE_d~~DRE~~ of aerosols in CSWC conditions is equal to $F_{aer} - F_{pristine}$, while it is rather, as already said, the RE_d~~DRE~~ aerosols would have in the absence of clouds. Overall, the yearly clear-sun aerosol RE_d~~DRE~~, for measurements coincident with AERONET retrievals, is around -20 W/m^2 (-66.5 and +46.6 on the direct and diffuse components, respectively), and the cloud RE_d~~DRE~~ around +10 W/m^2. As clouds act only on the diffuse component, the resulting mean measured CSUN GHI is about 10 W/m^2 lower than under pristine conditions (no aerosols nor clouds), but still 10 W/m^2 above the cloud-free level. ~~It is to be noticed that for all situations classified as clear-sun with cloud, including those where AERONET's retrieval fails, the conclusion about the importance of cloud enhancement effects which set SSI levels close to the ones in pristine conditions is still very valid: the level of GHI is close to the pristine one, with a difference of -0.8 W/m^2. At the scale of all situations identified as clear-sun, the level of GHI is 8 W/m^2 lower than under pristine conditions and 12 W/m^2 above the cloud-free level.~~

5 Conclusions

We perform in this study an analysis of the variabilities of global horizontal irradiance (GHI), its direct (BHI) and diffuse (DHI) components measured routinely at 1 min resolution over the period 2010-2022, as well as coincident aerosol optical properties measured by AERONET, with ground-based measurements from the ATOLL platform (Villeneuve d'Ascq, France), in a region marked with extensive variabilities of sky conditions and aerosol loadings.

As the amount and property of the SSI is quite different depending on sky situations, as well as its sensitivity to atmospheric parameters, we distinguish sky conditions by applying adapted filters based on irradiance's components that lead to three categories: clear-sky (CSKY), clear-sun with cloud (CSWC) and cloudy-sun (CLOS) situations. Over 2010-2022, these sky condition's occurrences represent 11, 22 and 67 % of the situations. The performances of this automatic filtering were validated with visual analysis of around 12000 sky-imager's observations. The risk of misinterpretation is 5 and 12 % for clear sky and clear sun (sum of CSKY and CSWC) situations, respectively, and higher for strong aerosol-load situations, which are rare in our case. Climatologies of SSI and its components were obtained for these three situations, between sunrise plus 30 minutes and sunset minus 30 minutes in order to minimize bias. CSWC situations, generally marked by irradiance enhancement effects due to clouds (Gueymard, 2017; Mol et al., 2023), are particularly interesting with on monthly-average 13 % more GHI than in CSKY situations (between +4 to +21 %) and diffuse proportions in CSWC situations on average 10 % above the mean proportion in CSKY situations (31 against 21 %).

A second classification of sky's condition concerns the atmospheric column loading of aerosols. A six-class categorization of aerosols, inspired by the work of Toledano et al. (2007), and based on photometric measurements of the aerosol optical depth (AOD), serves a climatological purpose and allows the definition of new models of aerosol optical properties, based on AERONET almucantar inversions. With this modelling, we perform radiative transfer simulations under cloud-free and aerosol-and-cloud-free («pristine») assumptions that allow the computation of the ~~direct~~ radiative impact on the downwelling SSI (RE_d)~~(DRE)~~ of aerosols and clouds in Lille over 2010-2022, as well as a sensitivity analysis of the solar irradiance to various input parameters, such as the aerosol's optical depth and Ångström exponent, PWV (Precipitable Water Vapor content) or even SZA (Solar Zenith Angle). The computed sensitivities are used in conjunction with the above classifications to refine an analysis of the variabilities of irradiance components observed in clear-sun conditions.

We focus on spring and summer seasons and analyse the coincident year-to-year variabilities over the period 2010-2022 of solar irradiances and sky conditions. The application of Mann-Kendall trend tests reveals for those seasons (significance's threshold of 5%) statistically significant trends both for the occurrences of clear and cloudy conditions and AOD, and for the global and direct components of the solar irradiance. Indeed, the average proportion of CLOS moments shows a decreasing trend of around -1 % per year for both seasons, in favor of a +0.5 % increased frequency of both CSWC and CSKY conditions. In addition, photometric measurements show a decrease in AOD over the period 2010-2022 for both seasons, particularly in spring, with an average trend of -0.008 per year. Finally, measurements of the incident solar radiation indicate significant upward trends in all-sky GHI for both seasons of around +4 $\pm$ 2 W/m^2 per year, which are mainly driven by a rise in BHI of around +4.4 $\pm$ 2.3 and +4.7 $\pm$ 1.9 W/m^2/year, respectively in spring and summer. Additionally, in summer, significant positive trends are also observed for both GHI and BHI for clear-sky situations (+3.1 W/m^2/year), as well as under clear-sun-with-cloud situations (+3.7 and +3.8 W/m^2/year, respectively for GHI and BHI). Note that although the statistical robustness of our trends may be affected by the performance of our classification of sky conditions and the length of the study period (13 years), they appear consistent, especially under all-sky conditions, with longer-term results in Europe (C3S, 2024; Ningombam et al., 2019; Boers et al., 2017).

We conducted a multivariate analysis of the irradiance variabilities in order to quantify the different contributions to the variabilities. It is first employed to analyze the particular case of spring 2020, which exhibited record values for both clear-sky and clear-sun frequency (34 and 57 % compared to the spring average of 15 % and 37 %) and radiation (389 W/m^2 compared to the average of 334 W/m^2). The analysis indicates that nearly 89 and 83 % of the record increases in GHI and BHI, respectively, are attributable to exceptional sunlight conditions. This conclusion aligns with the results of Heerwaarden et al. (2021) that also identified the peak in spring 2020 irradiance in Cabauw (Netherlands) as primarily driven (also a 89 % contribution) by a lower cloud fraction. Our analysis reveals in addition that most of the increase, 71 %, in BHI observed in spring 2020 in clear-sun conditions is due to a decrease in the SZA (-1.5° and -0.9° in CSKY and CSWC situations respectively), rather than the yet observed change in aerosol properties (decrease by 0.06 of AOD and decrease of continental polluted class, in CSWC and CSKY situations respectively). These findings are consistent with the results of the sensitivity analysis~~case studies~~

~~and sensitivity analyses~~, which show that in the absence of clouds (clear-sky conditions), the SZA has the most impact on the global irradiance, followed by the AOD and PWV. The multivariate analysis of the temporal trends in global and direct irradiances reveals that the variability of sky conditions significantly influences the observed all-sky increases in spring and summer, with seasonal contributions for GHI of 71 and 62 % and 79 and 74 % for BHI, respectively. Our analysis also indicates a significant contribution in all-sky seasonal BHI (around 20 %) from the variability of the BHI in CSWC conditions for both seasons. The sensitivity analysis of BHI to atmospheric parameters indicates that while the increase in spring is mainly linked to the variability of the aerosol content (+88 %), and most notably to a decrease in AOD (-0.011 per year), it relates in summer to comparable contributions from the solar zenith angle (44 %) and aerosol content (49 %) variabilities.

With radiative transfer simulations of aerosol-and-cloud-free (pristine) conditions and of cloud-free conditions, the study of the ~~direct~~ radiative effects (RE_d~~DRE~~) of aerosol and clouds is~~are~~ possible in clear-sun situations. The quantification of the aerosol RE_d~~DRE~~ in CSKY situations shows for our site an ~~relatively modest~~ average effect on GHI of -20 W/m^2 (-6 %), that results from an expected compensation between a negative effect on the direct (decrease three time larger: -61 W/m^2; -18 %) component and a positive forcing on the diffuse (increase two time larger: +42 W/m^2;+92%) irradiance. The influence of aerosols on the solar environment is significant in CSKY situations as the proportion of diffuse irradiance is on average two times larger (24%) in the presence of aerosols than under pristine-like conditions (12%). The statistical results~~, as well as case studies,~~ show that the radiative impact of aerosols on irradiances is mainly driven by the AOD, so lower aerosol RE_d~~DRE~~ are found in winter and during clean situations, and conversely higher aerosol RE_d~~DRE~~ values are found in spring and for continental-polluted situations. It translates into RE_d~~DRE~~ efficiencies (REE_d~~DREE~~) that are more case-independent than the RE_d~~DRE~~. In addition, results show that the REE_d~~DREE~~ is larger for coarser particles, particularly on the diffuse irradiance.

The identification of CSWC situations that represent 22 % of the cases, offers the opportunity to quantify important compensation mechanisms between the effects of aerosols (unambiguously on BHI) that tend to reduce the SSI, and the effects of clouds (unambiguously on DHI) that tend to increase it. Our analysis reveals that clouds increase on average the diffuse, and thus the global irradiances, by about +27 W/m^2 (6%). This cloud enhancement effect compensates, or even overcompensates, especially in clean, summer or continental situations, the overall radiative impact of aerosols, resulting in GHI values comparable or even higher than in pristine conditions (+13 W/m^2 and +4 W/m^2 in clean and polluted situations), with a much higher diffuse proportion (25 % against 21 in cloud-free situations, 10 % with the pristine hypothesis).

We present in this work a methodology and its potential for analyzing the contribution of the variability of cloudy and clear sky conditions to changes in incident surface solar irradiances. A multivariate analysis reveals that the overall variability of the surface solar irradiance is influenced by a combination of factors whose impacts can sometimes accumulate (e.g. increase in clear-sun occurrence, reduction of aerosol loading and decrease of SZA) or compensate, and that simple geometrical effects are not to be neglected. Further investigations would concern clear-sun with clouds and cloudy-sun conditions, which are prevalent

in Lille, in order to analyze the variability of the surface solar irradiance as a function of cloud cover parameters, including the fraction of the sky covered by clouds and the cloud type~~, the cloud optical depth and type~~.

Code and data availability. Python code to analyze data and generate figures is available from the first author upon request. The AERONET datasets were downloaded from the NASA AERONET website https://aeronet.gsfc.nasa.gov/. The ARTDECO original radiative transfer code was obtained from the ICARE Data Center in Lille, France (https://www.icare.univ-lille.fr/artdeco/). The dataset exploited in this study issued from ground measurements from the ATOLL (Atmospheric Observations in LiLLE, https://www.loa.univ-lille.fr/observations/plateformes.html?p=lille) platform in Villeneuve-d'Ascq, north of France, over the period 2010-2022, and containing both irradiance measurements, aerosol and gas column properties, obtained clear-sky and clear-sun flags, is freely available from an Easy System Data Repository in Chesnoiu et al. (2024).

Appendix A: Description of the cloud-screening methods

A1 Clear-sun detection

The method of Batlles et al. (2000) is a fairly straightforward method based on two criteria : (i) the clearness index ($K = \frac{GHI}{\mu_0 I_0}$) which represents the transmittance of the atmosphere relative to the incoming extraterrestrial solar irradiance (I_0), should be larger than a threshold value, K_{lim}; while (ii) the fraction of diffuse radiation ($D_f = \frac{DHI}{GHI}$) should be smaller than a maximum value $D_{f,lim}$. Note that both thresholds vary with the sun elevation angle $h = 90 - \text{SZA}$ as defined in Equations A1 and A2:

$$K_{lim} = -0.3262 - 0.0032h + 0.6843log_{10}(h) \quad \text{(A1)}$$

$$D_{f,lim} = 1.0827 - 0.3893log_{10}(h) \quad \text{(A2)}$$

A2 Clear-sky detection

The method of García et al. (2014) is based on the algorithm originally presented in Long and Ackerman (2000), which relies on a series of four tests based on GHI and DHI measurements of high frequency (3 minutes or less). The first two tests remove obvious cloudy moments characterized by extreme values of the normalized GHI (test 1) and measured diffuse irradiance (test 2) through the definition of threshold values of both quantities. The third and fourth tests are more elaborate allowing the more subtle detection of cloud covers through the analysis of the temporal variability of the global irradiance and the normalized diffuse irradiance ratio, respectively. The normalization of the GHI and DHI in the first and fourth tests is based on a power law of the cosine of the solar zenith angle as in Equation A3:

$$F_N = \frac{F}{\mu_0^{b_F}} \quad \text{(A3)}$$

where F correspond to the measured global irradiance (GHI) or diffuse irradiance ratio (D_f) and the coefficient «b_F» represents the variations of the associated clear-sky quantities with the cosine of the solar zenith angle μ_0. The subscript «N» represents the normalized quantities.

The four tests are applied in an iterative process to provide each time a new set of clear-sky moments, which are then used to calculate coefficients for the first and fourth tests for days with enough clear-sky observations by fitting the GHI and D_f 1-minute measurements with respect to μ_0, as in Equations A4 and A5 :

$$GHI = a_{GHI,\,day}\mu_0^{b_{GHI,\,day}} \tag{A4}$$

$$D_f = a_{D_f,\,day}\mu_0^{b_{D_f,\,day}} \tag{A5}$$

where GHI and D_f are the observed global irradiance and diffuse ratio, the parameters «a» represent the associated clear-sky quantities for a solar zenith angle of 0°. The coefficients «b» correspond to the parameters used for the normalization of the GHI and D_f as in Equation A3. A new set of parameters is then derived as the mean of the daily values and the iteration process continues until convergence is achieved within a tolerance of 5%. This method is thus quite versatile and can theoretically be applied to any observational site equipped with measurements of both global and diffuse irradiances.

In their work, García et al. (2014) showed that for the particular conditions of the Izaña Observatory, a high-elevation arid site located in the Canary Islands, the parameters «a» and «b» from Equations A4 and A5 could be expressed as functions of the daily AOD at 500 nm. This possibly reduces the method's versatility as it requires collocated aerosol optical properties. However, in this study, thanks to the availability of coincident photometric measurements, this method was selected as it gives more satisfactory results than the original algorithm of Long and Ackerman (2000), as shown in Section 2.2.1.

In the present study, as described in (Elias et al., 2024), the variability of the parameters "a_{GHI}", "b_{DHI}" and "b_{GHI}" with the AOD at 500 nm was adapted in order to better represent the conditions observed in Lille as they are quite different from those observed at the Izaña Observatory.

Appendix B: Definition of the models of aerosol optical properties

For the present study, new models of aerosol optical properties were defined using the available AERONET inversions of the aerosol volume size distribution and complex refractive index in Lille over the period 2010 - 2020. As mentioned Section 2.3.1, the goal is to create a look-up table of pre-computed aerosol optical properties (extinction coefficients, single scattering albedo, components of the phase function), which can be used as inputs by SOLARTDECO. Overall, the look-up table includes around 120 models of aerosol optical properties, which are divided between a fine and a coarse mode, the six aerosol classes from Section 2.2.2 and ten bins of surface relative humidity. The properties of each model are obtained through Mie calculations based on average aerosol normalized number size distributions of each mode and refractive indexes derived from AERONET inversions in Lille over the period 2010-2020. This methodology allows us to limit the use of Mie calculations and to compute specific aerosol optical properties at the resolution of AERONET direct-sun measurements by mixing pre-computed aerosol optical properties of the fine and coarse modes as follows:

– First, the appropriate pair of modes is selected from the look-up table using the measured values of AOD_{440}, $\mathrm{AE}_{440-870}$ and surface relative humidity.

– Then, a system of two equations with two unknowns based on the measured AOD_{440} and $\mathrm{AE}_{440-870}$ values is solved to compute two coefficients, namely the fine (*ff*) and coarse (*cf*) mode fractions (Eqs. B1 and B2) :

$$\mathrm{AOD}_{440,meas} = ff \times \mathrm{AOD}_{440,fine} + cf \times \mathrm{AOD}_{440,coarse} \tag{B1}$$

$$\mathrm{AE}_{440-870,meas} = ff \times \mathrm{AE}_{440-870,fine} + cf \times \mathrm{AE}_{440-870,coarse} \tag{B2}$$

with $\mathrm{AOD}_{440,fine}$, $\mathrm{AOD}_{440,coarse}$, $\mathrm{AE}_{440-870,fine}$ and $\mathrm{AE}_{440-870,coarse}$ the respective AOD values at 440 nm and AE between 440 and 870 nm of the fine and coarse modes. To determine the latter quantities, we assume that the observed aerosol layer corresponds to a mixture of two distinct observations, one characterized exclusively of fine mode aerosols and the other one only of coarse mode aerosols. Following this hypothesis, the measured aerosol optical depth at 550 nm ($\mathrm{AOD}_{550,meas}$) can be considered in each case as the AOD at 550 nm of the corresponding mode. This allows us to determine the AOD of each mode (either fine or coarse) at 440 nm from the measurement at 550 nm, using the pre-computed extinction coefficients ($Cext_{\lambda,mode}$) simulated by the Mie code at the wavelength λ (here, 440 and 550 nm), as in the following equation :

$$\begin{aligned}\mathrm{AOD}_{440,mode} &= \mathrm{AOD}_{550,meas} \times \left(\frac{440}{550}\right)^{-AE_{440-550,mode}} \\ &= \mathrm{AOD}_{550,meas} \times \frac{Cext_{440,mode}}{Cext_{550,mode}}\end{aligned} \tag{B3}$$

Note that the Angstrom coefficients between 440 and 870 nm of each mode are computed directly from the associated extinction coefficients, using Equation B4 :

$$\mathrm{AE}_{mode} = -\frac{log(\frac{Cext_{440,mode}}{Cext_{870,mode}})}{log(\frac{440}{870})} \tag{B4}$$

– The fractions *ff* and *cf* derived from the above system are then used, in conjunction with mean number concentrations NC_{fine} and NC_{coarse} defined for each mode based on AERONET inversions, to estimate new mixing ratios specific to the simulation, R_{fine} and R_{coarse}, through Equations B5 and B6 :

$$R_{fine} = \frac{ff \times NC_{fine}}{(ff \times NC_{fine} + cf \times NC_{coarse})} \tag{B5}$$

$$R_{coarse} = \frac{cf \times NC_{coarse}}{(ff \times NC_{fine} + cf \times NC_{coarse})} \tag{B6}$$

– Finally, these mixing ratios are used to compute, without additional Mie calculations, new mixed aerosol optical properties specific to the simulation by combination of the properties of each mode at each wavelengths, using Equations B7 to B10:

$$Cext_{\lambda,mix} = Cext_{\lambda,fine} \times R_{fine} + Cext_{\lambda,coarse} \times R_{coarse} \tag{B7}$$

$$Csca_{\lambda,mix} = Csca_{\lambda,fine} \times R_{fine} + Csca_{\lambda,coarse} \times R_{coarse} \tag{B8}$$

$$SSA_{\lambda,mix} = \frac{Csca_{\lambda,mix}}{Cext_{\lambda,mix}} \tag{B9}$$

$$P_{\lambda,mix} = \frac{P_{\lambda,fine} \times Csca_{\lambda,fine} \times R_{fine}}{Csca_{\lambda,mix}} + \frac{P_{\lambda,coarse} \times Csca_{\lambda,coarse} \times R_{coarse}}{Csca_{\lambda,mix}} \tag{B10}$$

where $Csca_{\lambda,mode} = Cext_{\lambda,mode} \times SSA_{\lambda,mode}$ is the scattering coefficient, $SSA_{\lambda,mode}$ the single scattering albedo and *P* represents the components of the phase function (P_{11}, P_{21}, P_{34} and P_{44}). The subscript «mix» stands for the new optical properties computed from the combination of the fine and coarse modes.

Author contributions. GC: formal analysis, methodology, data handling, writing (original draft preparation). NF and IC: conceptualization, funding acquisition, supervision, methodology, writing (review and editing). FA and DC and IJ: help to operate and maintain the radiative sensors and the sky imager. MC and TE: collaborate on the design of SOLARTDECO, the solar version of the radiative transfer code ARTDECO. All authors have contributed to the final manuscript.

Competing interests. The authors declare no competing interests.

Acknowledgements. The authors would like to thank Gérard Brogniez who initiated in 2008 at LOA the observational dataset of global, direct and diffuse solar irradiances at 1-min resolution and Colette Brogniez who initiated the automatic acquisition of full hemispheric pictures of the sky with a sky-imager in 2009. The authors would like to thank also Philippe Goloub, PI of AERONET site of Lille and the personnel of the PHOTONS observation station for their effort in establishing and maintaining the AERONET Lille site. We also appreciate the comments of the two anonymous reviewers that have helped us to improve the paper.

This study is issued from the work of G. Chesnoiu during his PhD thesis financed by the ADEME and Région Hauts-de-France. Additional funds were granted under the LEFE (Les Enveloppes Fluides et l'Environnement)/IMAGO (Interactions Multiples dans l'Atmosphère, la Glace, et l'Océan) CNRS-INSU program over the period 2021-2023.

References

Anderson, G., Clough, S., Kneizys, F., Chetwynd, J., and Shettle, E.: AFGL Atmospheric Constituent Profiles (0.120km), Tech. rep., Air Force Geophys. Lab., Hanscom Air Force Base, Bedford, Mass., 1986.

Batlles, F. J., Olmo, F. J., Tovar, J., and Alados-Arboledas, L.: Comparison of Cloudless Sky Parameterizations of Solar Irradianceat Various Spanish Midlatitude Locations, Theoretical and Applied Climatology, 66, 81–93, https://doi.org/10.1007/s007040070034, 2000.

Beck, H. E., Zimmermann, N. E., McVicar, T. R., Vergopolan, N., Berg, A., and Wood, E. F.: Present and future Köppen-Geiger climate classification maps at 1-km resolution, Scientific Data, 5, https://doi.org/10.1038/sdata.2018.214, 2018.

Blanc, P., Espinar, B., Geuder, N., Gueymard, C., Meyer, R., Pitz-Paal, R., Reinhardt, B., Renné, D., Sengupta, M., Wald, L., and Wilbert, S.: Direct normal irradiance related definitions and applications: The circumsolar issue, Solar Energy, 110, 561–577, https://doi.org/10.1016/j.solener.2014.10.001, 2014.

Boers, R., Brandsma, T., and Siebesma, A. P.: Impact of aerosols and clouds on decadal trends in all-sky solar radiation over the Netherlands (1966–2015), Atmospheric Chemistry and Physics, 17, 8081–8100, https://doi.org/10.5194/acp-17-8081-2017, 2017.

Boers, R., Bosveld, F., Baltink, H. K., Knap, W., van Meijgaard, E., and Wauben, W.: Observing and Modelling the Surface Radiative Budget and Cloud Radiative Forcing at the Cabauw Experimental Site for Atmospheric Research (CESAR), the Netherlands, 2009–17, Journal of Climate, 32, 7209 – 7225, https://doi.org/10.1175/JCLI-D-18-0828.1, 2019.

C3S: European State of the Climate 2023, Full report, https://climate.copernicus.eu/esotc/2023, (Last accessed on 2024-07-03), 2024.

Chesnoiu, G., Ferlay, N., and Chiapello, I.: Ground measurements of surface solar irradiance, aerosol optical properties and sky conditions estimates in Lille (North of France) over the period 2010-2022., https://doi.org/10.57932/ca9c74c0-83f4-43f1-86c8-7f3ce517b03c, 2024.

Cuesta, J., Costantino, L., Beekmann, M., Siour, G., Menut, L., Bessagnet, B., Landi, T. C., Dufour, G., and Eremenko, M.: Ozone pollution during the COVID-19 lockdown in the spring of 2020 over Europe, analysed from satellite observations, in situ measurements, and models, Atmospheric Chemistry and Physics, 22, 4471–4489, https://doi.org/10.5194/acp-22-4471-2022, 2022.

Derimian, Y., Léon, J.-F., Dubovik, O., Chiapello, I., Tanré, D., Sinyuk, A., Auriol, F., Podvin, T., Brogniez, G., and Holben, B. N.: Radiative properties of aerosol mixture observed during the dry season 2006 over M'Bour, Senegal (African Monsoon Multidisciplinary Analysis campaign), Journal of Geophysical Research, 113, https://doi.org/10.1029/2008jd009904, 2008.

Derimian, Y., Dubovik, O., Tanre, D., Goloub, P., Lapyonok, T., and Mortier, A.: Optical properties and radiative forcing of the Eyjafjallajökull volcanic ash layer observed over Lille, France, in 2010, Journal of Geophysical Research: Atmospheres, 117, https://doi.org/10.1029/2011JD016815, 2012.

Drugé, T., Nabat, P., Mallet, M., and Somot, S.: Future evolution of aerosols and implications for climate change in the Euro-Mediterranean region using the CNRM-ALADIN63 regional climate model, Atmospheric Chemistry and Physics, 21, 7639–7669, https://doi.org/10.5194/acp-21-7639-2021, 2021.

Dubovik, O. and King, M. D.: A flexible inversion algorithm for retrieval of aerosol optical properties from Sun and sky radiance measurements, Journal of Geophysical Research: Atmospheres, 105, 20 673–20 696, https://doi.org/10.1029/2000JD900282, 2000.

Dubovik, O., Smirnov, A., Holben, B. N., King, M. D., Kaufman, Y. J., Eck, T. F., and Slutsker, I.: Accuracy assessments of aerosol optical properties retrieved from Aerosol Robotic Network (AERONET) Sun and sky radiance measurements, Journal of Geophysical Research: Atmospheres, 105, 9791–9806, https://doi.org/10.1029/2000JD900040, 2000.

Dubovik, O., Holben, B., Eck, T. F., Smirnov, A., Kaufman, Y. J., King, M. D., Tanré, D., and Slutsker, I.: Variability of Absorption and Optical Properties of Key Aerosol Types Observed in Worldwide Locations, Journal of the Atmospheric Sciences, 59, 590 – 608, https://doi.org/10.1175/1520-0469(2002)059<0590:VOAAOP>2.0.CO;2, 2002.

Dubuisson, P., Labonnote, L., Riedi, J., Compiègne, M., and Winiarek, V.: ARTDECO : Atmospheric Radiative Transfer Database for Earth and Climate Observation, in: International Radiation Symposium (IRS), 2016.

Elias, T., Ferlay, N., Chesnoiu, G., Chiapello, I., and Moulana, M.: Regional validation of the solar irradiance tool SolaRes in clear-sky conditions, with a focus on the aerosol module, Atmospheric Measurement Techniques, 17, 4041–4063, https://doi.org/10.5194/amt-17-4041-2024, 2024.

Favez, O., Weber, S., Petit, J.-E., Alleman, L. Y., Albinet, A., Riffault, V., Chazeau, B., Amodeo, T., Salameh, D., Zhang, Y., Srivastava, D., Samaké, A., Aujay-Plouzeau, R., Papin, A., Bonnaire, N., Boullanger, C., Chatain, M., Chevrier, F., Detournay, A., Dominik-Sègue, M., Falhun, R., Garbin, C., Ghersi, V., Grignion, G., Levigoureux, G., Pontet, S., Rangognio, J., Zhang, S., Besombes, J.-L., Conil, S., Uzu, G., Savarino, J., Marchand, N., Gros, V., Marchand, C., Jaffrezo, J.-L., and Leoz-Garziandia, E.: Overview of the French Operational Network for In Situ Observation of PM Chemical Composition and Sources in Urban Environments (CARA Program), Atmosphere, 12, 207, https://doi.org/10.3390/atmos12020207, 2021.

Fu, F., Purvis-Roberts, K. L., and Williams, B.: Impact of the COVID-19 Pandemic Lockdown on Air Pollution in 20 Major Cities around the World, Atmosphere, 11, https://doi.org/10.3390/atmos11111189, 2020.

García, R. D., García, O. E., Cuevas, E., Cachorro, V. E., Romero-Campos, P. M., Ramos, R., and de Frutos, A. M.: Solar radiation measurements compared to simulations at the BSRN Izaña station. Mineral dust radiative forcing and efficiency study, Journal of Geophysical Research: Atmospheres, 119, 179–194, https://doi.org/10.1002/2013JD020301, 2014.

Giles, D. M., Sinyuk, A., Sorokin, M. G., Schafer, J. S., Smirnov, A., Slutsker, I., Eck, T. F., Holben, B. N., Lewis, J. R., Campbell, J. R., Welton, E. J., Korkin, S. V., and Lyapustin, A. I.: Advancements in the Aerosol Robotic Network (AERONET) Version 3 database – automated near-real-time quality control algorithm with improved cloud screening for Sun photometer aerosol optical depth (AOD) measurements, Atmospheric Measurement Techniques, 12, 169–209, https://doi.org/10.5194/amt-12-169-2019, 2019.

Gueymard, C.: Parametrized transmittance model for direct beam and circumsolar spectral irradiance, Solar Energy, 71, 325–346, https://doi.org/10.1016/S0038-092X(01)00054-8, 2001.

Gueymard, C.: Spectral Circumsolar Radiation Contribution To CPV, AIP Conference Proceedings, 1277, 316–319, https://doi.org/10.1063/1.3509220, 2010.

Gueymard, C. A.: Cloud and albedo enhancement impacts on solar irradiance using high-frequency measurements from thermopile and photodiode radiometers. Part 1: Impacts on global horizontal irradiance., Solar Energy, 153, 755–765, https://doi.org/10.1016/j.solener.2017.05.004, 2017.

Gueymard, C. A., Bright, J. M., Lingfors, D., Habte, A., and Sengupta, M.: A posteriori clear-sky identification methods in solar irradiance time series: Review and preliminary validation using sky imagers, Renewable and Sustainable Energy Reviews, 109, 412–427, https://doi.org/10.1016/j.rser.2019.04.027, 2019.

Gutiérrez, C., Somot, S., Nabat, P., Mallet, M., Corre, L., van Meijgaard, E., Perpiñán, O., and Gaertner, M. Á.: Future evolution of surface solar radiation and photovoltaic potential in Europe: investigating the role of aerosols, Environmental Research Letters, 15, 034 035, https://doi.org/10.1088/1748-9326/ab6666, 2020.

Hahn, C. and Warren, S.: A Gridded Climatology of Clouds over Land (1971-1996) and Ocean (1954-2008) from Surface Observations Worldwide (NDP-026E)*, https://doi.org/10.3334/CDIAC/CLI.NDP026E, 2007.

Hauglustaine, D. A., Balkanski, Y., and Schulz, M.: A global model simulation of present and future nitrate aerosols and their direct radiative forcing of climate, Atmospheric Chemistry and Physics, 14, 11 031–11 063, https://doi.org/10.5194/acp-14-11031-2014, 2014.

Heerwaarden, van, C. C., Mol, W. B., Veerman, M. A., Benedict, I., Heusinkveld, B. G., Knap, W. H., Kazadzis, S., Kouremeti, N., and Fiedlerq, S.: Record high solar irradiance in Western Europe during first COVID-19 lockdown largely due to unusual weather, Communications Earth & Environment, 2, 37, https://doi.org/10.1038/s43247-021-00110-0, 2021.

Holben, B. N., Tanré, D., Smirnov, A., Eck, T. F., Slutsker, I., Abuhassan, N., Newcomb, W. W., Schafer, J. S., Chatenet, B., Lavenu, F., Kaufman, Y. J., Castle, J. V., Setzer, A., Markham, B., Clark, D., Frouin, R., Halthore, R., Karneli, A., O'Neill, N. T., Pietras, C., Pinker, R. T., Voss, K., and Zibordi, G.: An emerging ground-based aerosol climatology: Aerosol optical depth from AERONET, Journal of Geophysical Research: Atmospheres, 106, 12 067–12 097, https://doi.org/10.1029/2001JD900014, 2001.

Hou, X., Wild, M., Folini, D., Kazadzis, S., and Wohland, J.: Climate change impacts on solar power generation and its spatial variability in Europe based on CMIP6, Earth System Dynamics, 12, 1099–1113, https://doi.org/10.5194/esd-12-1099-2021, 2021.

Jerez, S., Tobin, I., Vautard, R., Montávez, J. P., López-Romero, J. M., Thais, F., Bartok, B., Christensen, O. B., Colette, A., Déqué, M., Nikulin, G., Kotlarski, S., van Meijgaard, E., Teichmann, C., and Wild, M.: The impact of climate change on photovoltaic power generation in Europe, Nature Communications, 6, https://doi.org/10.1038/ncomms10014, 2015.

Kato, S., Ackerman, T. P., Mather, J. H., and Clothiaux, E. E.: The k-distribution method and correlated-k approximation for a shortwave radiative transfer model, Journal of Quantitative Spectroscopy and Radiative Transfer, 62, 109–121, https://doi.org/10.1016/S0022-4073(98)00075-2, 1999.

Kendall, M.: Rank correlation methods, E. Arnold Oxford University Press, London New York, NY, ISBN 9780195208375, 1990.

Kirn, B., Brecl, K., and Topic, M.: A new PV module performance model based on separation of diffuse and direct light, Solar Energy, 113, 212–220, https://doi.org/10.1016/j.solener.2014.12.029, 2015.

Kok, J. F., Ridley, D. A., Zhou, Q., Miller, R. L., Zhao, C., Heald, C. L., Ward, D. S., Albani, S., and Haustein, K.: Smaller desert dust cooling effect estimated from analysis of dust size and abundance, Nature Geoscience, 10, 274–278, 2017.

Lacis, A. A. and Oinas, V.: A description of the correlated k distribution method for modeling nongray gaseous absorption, thermal emission, and multiple scattering in vertically inhomogeneous atmospheres, Journal of Geophysical Research, 96, 9027, https://doi.org/10.1029/90jd01945, 1991.

Liepert, B. and Tegen, I.: Multidecadal solar radiation trends in the United States and Germany and direct tropospheric aerosol forcing, Journal of Geophysical Research: Atmospheres, 107, AAC 7–1–AAC 7–15, https://doi.org/10.1029/2001JD000760, 2002.

Liepert, B. G.: Observed reductions of surface solar radiation at sites in the United States and worldwide from 1961 to 1990, Geophysical Research Letters, 29, 61–1–61–4, https://doi.org/10.1029/2002GL014910, 2002.

Lindsay, N., Libois, Q., Badosa, J., Migan-Dubois, A., and Bourdin, V.: Errors in PV power modelling due to the lack of spectral and angular details of solar irradiance inputs, Solar Energy, 197, 266–278, https://doi.org/10.1016/j.solener.2019.12.042, 2020.

Liu, M., Zhang, J., and Xia, X.: Evaluation of multiple surface irradiance-based clear sky detection methods at Xianghe—A heavy polluted site on the North China Plain., Atmospheric and Oceanic Science Letters, 14, 100 016, https://doi.org/10.1016/j.aosl.2020.100016, 2021.

Long, C. N. and Ackerman, T. P.: Identification of clear skies from broadband pyranometer measurements and calculation of downwelling shortwave cloud effects, Journal of Geophysical Research: Atmospheres, 105, 15 609–15 626, https://doi.org/10.1029/2000JD900077, 2000.

Manara, V., Brunetti, M., Celozzi, A., Maugeri, M., Sanchez-Lorenzo, A., and Wild, M.: Detection of dimming/brightening in Italy from homogenized all-sky and clear-sky surface solar radiation records and underlying causes (1959–2013), Atmospheric Chemistry and Physics, 16, 11 145–11 161, https://doi.org/10.5194/acp-16-11145-2016, 2016.

Mann, H. B.: Nonparametric Tests Against Trend, Econometrica, 13, 245, https://doi.org/10.2307/1907187, 1945.

Mateos, D., Sanchez-Lorenzo, A., Antón, M., Cachorro, V. E., Calbó, J., Costa, M. J., Torres, B., and Wild, M.: Quantifying the respective roles of aerosols and clouds in the strong brightening since the early 2000s over the Iberian Peninsula, Journal of Geophysical Research: Atmospheres, 119, 10,382–10,393, https://doi.org/10.1002/2014JD022076, 2014.

Meteorological Organization, W.: WMO Guide To Meteorological Instruments And Methods Of Observation, vol. 8, p. 681, Meteorological Organization, World, 7 edn., ISBN 978-92-63-100085, 2008.

Michalsky, J., Dutton, E., Rubes, M., Nelson, D., Stoffel, T., Wesley, M., Splitt, M., and DeLuisi, J.: Optimal Measurement of Surface Shortwave Irradiance Using Current Instrumentation, Journal of Atmospheric and Oceanic Technology, 16, 55 – 69, https://doi.org/10.1175/1520-0426(1999)016<0055:OMOSSI>2.0.CO;2, 1999.

Mol, W. B., van Stratum, B. J. H., Knap, W. H., and van Heerwaarden, C.: Reconciling observations of solar irradiance variability with cloud size distributions, Journal of Geophysical Research: Atmospheres, 128, e2022JD037894, https://doi.org/10.1029/2022JD037894, 2023.

Moss, R. H., Edmonds, J. A., Hibbard, K. A., Manning, M. R., Rose, S. K., van Vuuren, D. P., Carter, T. R., Emori, S., Kainuma, M., Kram, T., Meehl, G. A., Mitchell, J. F. B., Nakicenovic, N., Riahi, K., Smith, S. J., Stouffer, R. J., Thomson, A. M., Weyant, J. P., and Wilbanks, T. J.: The next generation of scenarios for climate change research and assessment, Nature, 463, 747–756, https://doi.org/10.1038/nature08823, 2010.

Nakajima, T., Tanaka, M., and Yamauchi, T.: Retrieval of the optical properties of aerosols from aureole and extinction data, Appl. Opt., 22, 2951–2959, https://doi.org/10.1364/AO.22.002951, 1983.

Nakajima, T., Tonna, G., Rao, R., Boi, P., Kaufman, Y., and Holben, B.: Use of sky brightness measurements from ground for remote sensing of particulate polydispersions, Appl. Opt., 35, 2672–2686, https://doi.org/10.1364/AO.35.002672, 1996.

Ningombam, S. S., Larson, E., Dumka, U., Estellés, V., Campanelli, M., and Steve, C.: Long-term (1995–2018) aerosol optical depth derived using ground based AERONET and SKYNET measurements from aerosol aged-background sites, Atmospheric Pollution Research, 10, 608–620, https://doi.org/10.1016/j.apr.2018.10.008, 2019.

Norris, J. R. and Wild, M.: Trends in aerosol radiative effects over Europe inferred from observed cloud cover, solar "dimming," and solar "brightening", Journal of Geophysical Research: Atmospheres, 112, https://doi.org/10.1029/2006JD007794, 2007.

O'Neill, N. T., Eck, T. F., Smirnov, A., Holben, B. N., and Thulasiraman, S.: Spectral discrimination of coarse and fine mode optical depth, Journal of Geophysical Research: Atmospheres, 108, https://doi.org/10.1029/2002JD002975, 2003.

Ordóñez, C., Garrido-Perez, J. M., and García-Herrera, R.: Early spring near-surface ozone in Europe during the COVID-19 shutdown: Meteorological effects outweigh emission changes, Science of The Total Environment, 747, 141 322, https://doi.org/10.1016/j.scitotenv.2020.141322, 2020.

Papadimas, C. D., Hatzianastassiou, N., Matsoukas, C., Kanakidou, M., Mihalopoulos, N., and Vardavas, I.: The direct effect of aerosols on solar radiation over the broader Mediterranean basin, Atmospheric Chemistry and Physics, 12, 7165–7185, https://doi.org/10.5194/acp-12-7165-2012, 2012.

Pecenak, Z. K., Mejia, F. A., Kurtz, B., Evan, A., and Kleissl, J.: Simulating irradiance enhancement dependence on cloud optical depth and solar zenith angle, Solar Energy, 136, 675–681, https://doi.org/https://doi.org/10.1016/j.solener.2016.07.045, 2016.

Petit, J.-E., Dupont, J.-C., Favez, O., Gros, V., Zhang, Y., Sciare, J., Simon, L., Truong, F., Bonnaire, N., Amodeo, T., Vautard, R., and Haeffelin, M.: Response of atmospheric composition to COVID-19 lockdown measures during spring in the Paris region (France), Atmospheric Chemistry and Physics, 21, 17 167–17 183, https://doi.org/10.5194/acp-21-17167-2021, 2021.

Pfeifroth, U., Sanchez-Lorenzo, A., Manara, V., Trentmann, J., and Hollmann, R.: Trends and Variability of Surface Solar Radiation in Europe Based On Surface- and Satellite-Based Data Records, Journal of Geophysical Research: Atmospheres, 123, 1735–1754, https://doi.org/10.1002/2017JD027418, 2018.

Philipona, R., Behrens, K., and Ruckstuhl, C.: How declining aerosols and rising greenhouse gases forced rapid warming in Europe since the 1980s, Geophysical Research Letters, 36, https://doi.org/10.1029/2008GL036350, 2009.

Potier, E., Waked, A., Bourin, A., Minvielle, F., Péré, J., Perdrix, E., Michoud, V., Riffault, V., Alleman, L., and Sauvage, S.: Characterizing the regional contribution to PM10 pollution over northern France using two complementary approaches: Chemistry transport and trajectory-based receptor models, Atmospheric Research, 223, 1–14, https://doi.org/10.1016/j.atmosres.2019.03.002, 2019.

Putaud, J.-P., Van Dingenen, R., Alastuey, A., Bauer, H., Birmili, W., Cyrys, J., Flentje, H., Fuzzi, S., Gehrig, R., Hansson, H., Harrison, R., Herrmann, H., Hitzenberger, R., Hüglin, C., Jones, A., Kasper-Giebl, A., Kiss, G., Kousa, A., Kuhlbusch, T., Löschau, G., Maenhaut, W., Molnar, A., Moreno, T., Pekkanen, J., Perrino, C., Pitz, M., Puxbaum, H., Querol, X., Rodriguez, S., Salma, I., Schwarz, J., Smolik, J., Schneider, J., Spindler, G., ten Brink, H., Tursic, J., Viana, M., Wiedensohler, A., and Raes, F.: A European aerosol phenomenology – 3: Physical and chemical characteristics of particulate matter from 60 rural, urban, and kerbside sites across Europe, Atmospheric Environment, 44, 1308–1320, https://doi.org/10.1016/j.atmosenv.2009.12.011, 2010.

Pérez-Ramírez, D., Whiteman, D., Smirnov, A., Lyamani, H., Holben, B., Pinker, R., Andrade, M., and Arboledas, L.: Evaluation of AERONET precipitable water vapor versus microwave radiometry, GPS, and radiosondes at ARM sites, Journal of Geophysical Research: Atmospheres, 119, https://doi.org/10.1002/2014JD021730, 2014.

Reifenberg, S. F., Martin, A., Kohl, M., Bacer, S., Hamryszczak, Z., Tadic, I., Röder, L., Crowley, D. J., Fischer, H., Kaiser, K., Schneider, J., Dörich, R., Crowley, J. N., Tomsche, L., Marsing, A., Voigt, C., Zahn, A., Pöhlker, C., Holanda, B. A., Krüger, O., Pöschl, U., Pöhlker, M., Jöckel, P., Dorf, M., Schumann, U., Williams, J., Bohn, B., Curtius, J., Harder, H., Schlager, H., Lelieveld, J., and Pozzer, A.: Numerical simulation of the impact of COVID-19 lockdown on tropospheric composition and aerosol radiative forcing in Europe, Atmospheric Chemistry and Physics, 22, 10 901–10 917, https://doi.org/10.5194/acp-22-10901-2022, 2022.

Romanou, A., Liepert, B., Schmidt, G. A., Rossow, W. B., Ruedy, R. A., and Zhang, Y.: 20th century changes in surface solar irradiance in simulations and observations, Geophysical Research Letters, 34, https://doi.org/10.1029/2006GL028356, 2007.

Ruckstuhl, C. and Norris, J. R.: How do aerosol histories affect solar "dimming" and "brightening" over Europe?: IPCC-AR4 models versus observations, Journal of Geophysical Research: Atmospheres, 114, https://doi.org/10.1029/2008JD011066, 2009.

Ruckstuhl, C., Philipona, R., Behrens, K., Collaud Coen, M., Dürr, B., Heimo, A., Mätzler, C., Nyeki, S., Ohmura, A., Vuilleumier, L., Weller, M., Wehrli, C., and Zelenka, A.: Aerosol and cloud effects on solar brightening and the recent rapid warming, Geophysical Research Letters, 35, https://doi.org/10.1029/2008GL034228, 2008.

Sanchez-Lorenzo, A., Calbó, J., and Wild, M.: Global and diffuse solar radiation in Spain: Building a homogeneous dataset and assessing their trends, Global and Planetary Change, 100, 343–352, https://doi.org/10.1016/j.gloplacha.2012.11.010, 2013.

Satheesh, S. and Ramanathan, V.: Large differences in tropical aerosol forcing at the top of the atmosphere and Earth's surface, Nature, 405, 60–63, 2000.

Schwarz, M., Folini, D., Yang, S., Allan, R. P., and Wild, M.: Changes in atmospheric shortwave absorption as important driver of dimming and brightening, Nature Geoscience, 13, 110–115, https://doi.org/10.1038/s41561-019-0528-y, 2020.

Sengupta, M., Habte, A., Wilbert, S., Gueymard, C., and Remund, J.: Best Practices Handbook for the Collection and Use of Solar Resource Data for Solar Energy Applications: Third Edition, https://doi.org/10.2172/1778700, collaboration with the International Energy Agency, 2021.

Shuvalova, J., Chubarova, N., and Shatunova, M.: Impact of Cloud Condensation Nuclei Reduction on Cloud Characteristics and Solar Radiation during COVID-19 Lockdown 2020 in Moscow, Atmosphere, 13, https://doi.org/10.3390/atmos13101710, 2022.

Smirnov, A., Holben, B., Lyapustin, A., Slutsker, I., and Eck, T.: AERONET processing algorithms refinement, AERONET Workshop, 2004.

Sun, X., Bright, J., Gueymard, C., Acord, B., Wang, P., and Engerer, N.: Worldwide performance assessment of 75 global clear-sky irradiance models using Principal Component Analysis, Renewable and Sustainable Energy Reviews, 111, 550–570, https://doi.org/10.1016/j.rser.2019.04.006, 2019.

Sun, X., Bright, J. M., Gueymard, C. A., Bai, X., Acord, B., and Wang, P.: Worldwide performance assessment of 95 direct and diffuse clear-sky irradiance models using principal component analysis, Renewable and Sustainable Energy Reviews, 135, 110 087, https://doi.org/10.1016/j.rser.2020.110087, 2021.

Thorsen, T. J., Ferrare, R. A., Kato, S., and Winker, D. M.: Aerosol Direct Radiative Effect Sensitivity Analysis, Journal of Climate, 33, 6119 – 6139, https://doi.org/10.1175/JCLI-D-19-0669.1, 2020.

Tobin, I., Greuell, W., Jerez, S., Ludwig, F., Vautard, R., van Vliet, M. T. H., and Bréon, F.-M.: Vulnerabilities and resilience of European power generation to 1.5°C, 2°C and 3°C warming, Environmental Research Letters, 13, 044 024, https://doi.org/10.1088/1748-9326/aab211, 2018.

Toledano, C., Cachorro, V. E., Berjon, A., de Frutos, A. M., Sorribas, M., de la Morena, B. A., and Goloub, P.: Aerosol optical depth and Ångström exponent climatology at El Arenosillo AERONET site (Huelva, Spain), Quarterly Journal of the Royal Meteorological Society, 133, 795–807, https://doi.org/10.1002/qj.54, 2007.

Tsay, S.-C., Stamnes, K., Wiscombe, W., Laszlo, I., and Einaudi, F.: General Purpose Fortran Program for Discrete-Ordinate-Method Radiative Transfer in Scattering and Emitting Layered Media: An Update of DISORT, Tech. rep., NASA Goddard Space Flight Center, 2000.

Turnock, S. T., Spracklen, D. V., Carslaw, K. S., Mann, G. W., Woodhouse, M. T., Forster, P. M., Haywood, J., Johnson, C. E., Dalvi, M., Bellouin, N., and Sanchez-Lorenzo, A.: Modelled and observed changes in aerosols and surface solar radiation over Europe between 1960 and 2009, Atmospheric Chemistry and Physics, 15, 9477–9500, https://doi.org/10.5194/acp-15-9477-2015, 2015.

Velazquez-Garcia, A., Crumeyrolle, S., F. de Brito, J., Tison, E., Bourrianne, E., Chiapello, I., and Riffault, V.: Deriving composition-dependent aerosol absorption, scattering and extinction mass efficiencies from multi-annual high time resolution observations in Northern France, Atmospheric Environment, 298, 119 613, https://doi.org/10.1016/j.atmosenv.2023.119613, 2023.

Velders, G. J., Willers, S. M., Wesseling, J., van den Elshout, S., van der Swaluw, E., Mooibroek, D., and van Ratingen, S.: Improvements in air quality in the Netherlands during the corona lockdown based on observations and model simulations, Atmospheric Environment, 247, 118 158, https://doi.org/10.1016/j.atmosenv.2020.118158, 2021.

Voigt, C., Lelieveld, J., Schlager, H., Schneider, J., Curtius, J., Meerkötter, R., Sauer, D., Bugliaro, L., Bohn, B., Crowley, J. N., Erbertseder, T., Groß, S., Hahn, V., Li, Q., Mertens, M., Pöhlker, M. L., Pozzer, A., Schumann, U., Tomsche, L., Williams, J., Zahn, A., Andreae, M., Borrmann, S., Bräuer, T., Dörich, R., Dörnbrack, A., Edtbauer, A., Ernle, L., Fischer, H., Giez, A., Granzin, M., Grewe, V., Harder, H., Heinritzi, M., Holanda, B. A., Jöckel, P., Kaiser, K., Krüger, O. O., Lucke, J., Marsing, A., Martin, A., Matthes, S., Pöhlker, C., Pöschl, U., Reifenberg, S., Ringsdorf, A., Scheibe, M., Tadic, I., Zauner-Wieczorek, M., Henke, R., and Rapp, M.: Cleaner Skies during the COVID-19 Lockdown, Bulletin of the American Meteorological Society, 103, E1796 – E1827, https://doi.org/10.1175/BAMS-D-21-0012.1, 2022.

Vuilleumier, L., Hauser, M., Félix, C., Vignola, F., Blanc, P., Kazantzidis, A., and Calpini, B.: Accuracy of ground surface broadband shortwave radiation monitoring, Journal of Geophysical Research: Atmospheres, 119, 13,838–13,860, https://doi.org/10.1002/2014JD022335, 2014.

Warren, S., Eastman, R., and Hahn, C.: A Survey of Changes in Cloud Cover and Cloud Types over Land from Surface Observations, 1971 96, Journal of Climate - J CLIMATE, 20, https://doi.org/10.1175/JCLI4031.1, 2007.

Wild, M.: Global dimming and brightening: A review, Journal of Geophysical Research: Atmospheres, 114, https://doi.org/10.1029/2008JD011470, 2009.

Wild, M., Gilgen, H., Roesch, A., Ohmura, A., Long, C. N., Dutton, E. G., Forgan, B., Kallis, A., Russak, V., and Tsvetkov, A.: From Dimming to Brightening: Decadal Changes in Solar Radiation at Earth's Surface, Science, 308, 847–850, https://doi.org/10.1126/science.1103215, 2005.

Wild, M., Wacker, S., Yang, S., and Sanchez-Lorenzo, A.: Evidence for Clear-Sky Dimming and Brightening in Central Europe, Geophysical Research Letters, 48, e2020GL092 216, https://doi.org/10.1029/2020GL092216, 2021.

Witthuhn, J., Hünerbein, A., Filipitsch, F., Wacker, S., Meilinger, S., and Deneke, H.: Aerosol properties and aerosol–radiation interactions in clear-sky conditions over Germany, Atmospheric Chemistry and Physics, 21, 14 591–14 630, https://doi.org/10.5194/acp-21-14591-2021, 2021.

WMO: Manual on the Global Observing System, WMO ; no. 544, Secretariat of the World Meteorological Organization, Geneva, Switzerland, ISBN 9789263105448, 2003.

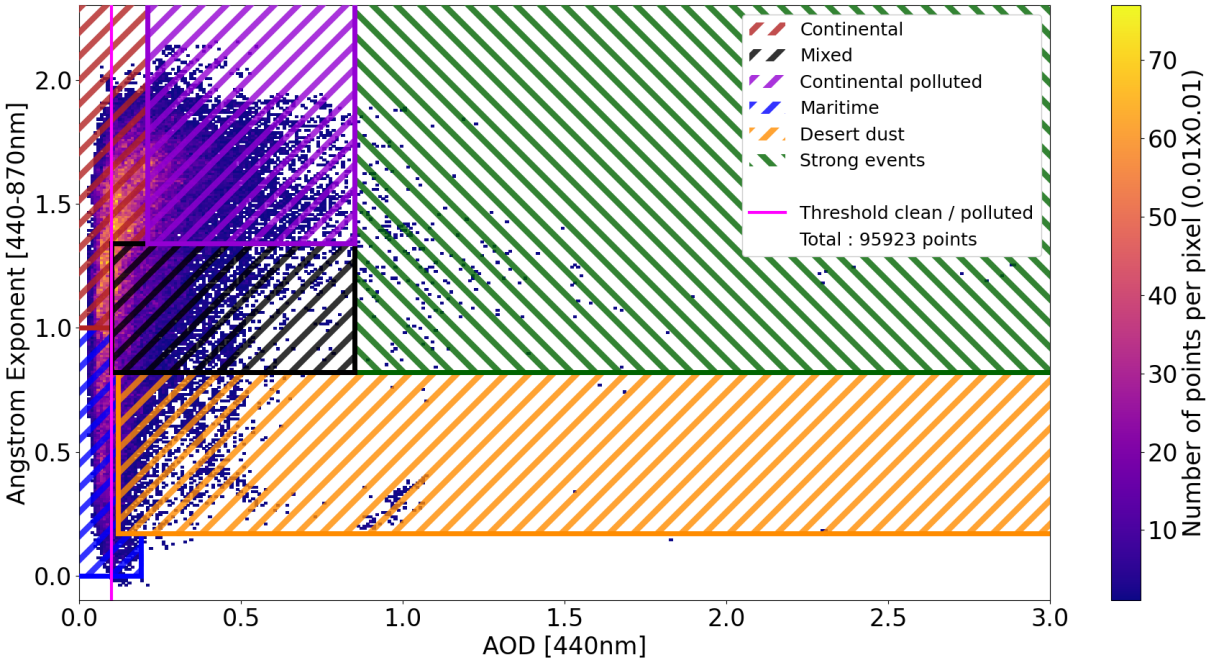

Figure S1. Scatter plot of AOD_{440} against $AE_{440-870}$ for all AERONET level 2.0 measurements in Lille from 2010 to 2022. Colored boxes represent the class thresholds from Table 2.

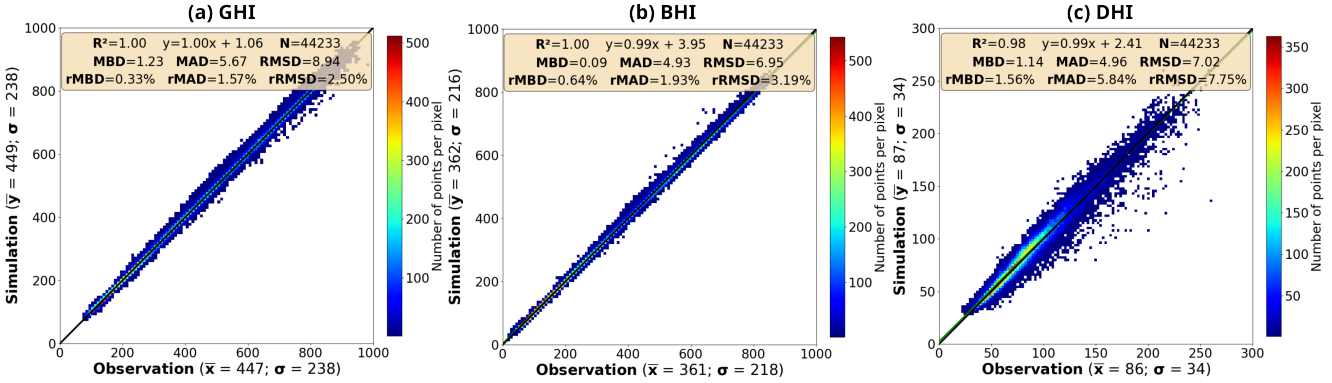

Figure S2. Scatter plot of SOLARTDECO simulations, based on level 2.0 AERONET inputs, against corresponding measurements of (a) GHI, (b) BHI and (c) DHI performed in Lille over the period 2010-2022. These results were obtained for SOLARTDECO simulations based on a different system of two equations, involving both AOD_{440} and AOD_{870}, instead of the original AOD_{440} and $AE_{440-870}$ system. The black line represents the 1:1 line. Mean irradiance values and associated standard deviations are shown for both simulations and observations on their respective axes. Absolute and relative values of MBD (Mean Bias Difference), MAD (Mean Absolute difference) and RMSD (Root Mean Square Difference) are also displayed in the beige box included in the different figures. Only observations that coincide with clear-sky flux measurements (identified by the algorithm presented in Section 2.2.1) and performed between sunrise plus 30 minutes and sunset minus 30 minutes are considered for these comparisons.

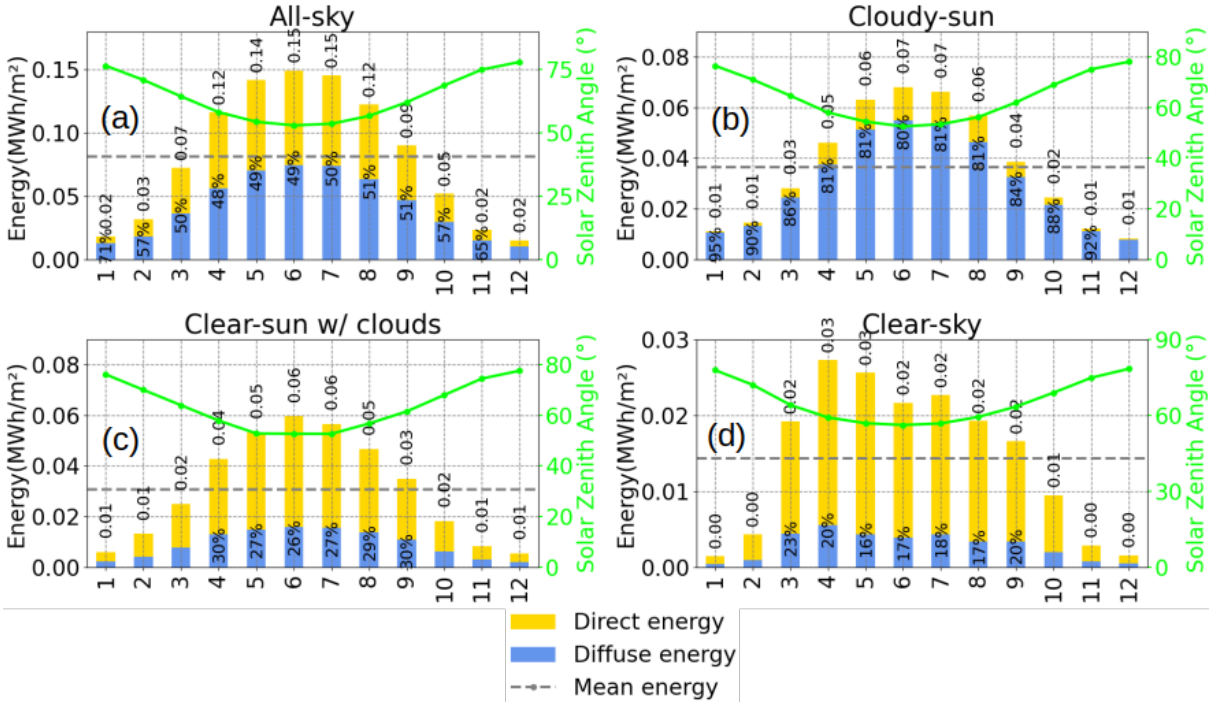

Figure S3. Multi-monthly variations over the period 2010-2022 of the solar zenith angle (green line) and cumulative yearly energies for different cloud cover states: (a) all-sky, (b) cloudy-sun, (c) clear-sun with clouds and (d) clear-sky. Only values during daytime between [sunrise + 30 minutes; sunset - 30 minutes] are considered. The global energy is represented as columns with the lower blue part corresponding to the diffuse energy and the upper yellow part to the direct energy. The grey dashed lines represent the yearly energy over 2010-2020. Note that the percentages reflect the diffuse fraction of the overall yearly energy which values are reported above each column.

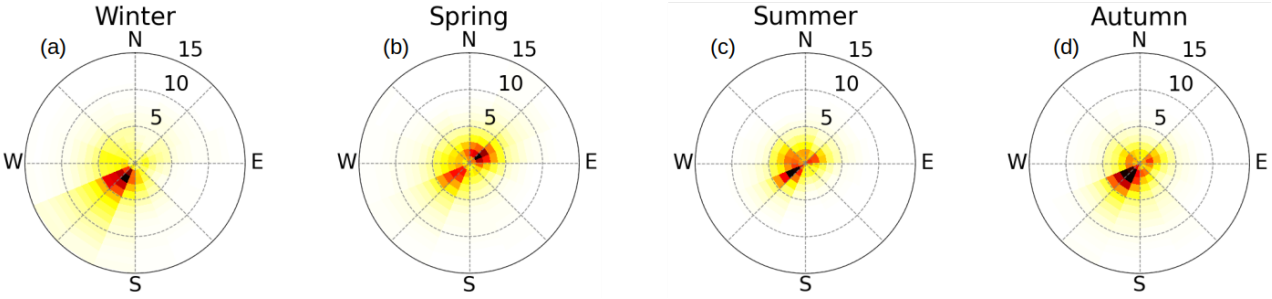

Figure S4. Seasonal wind roses based on additional ATOLL measurements over the period 2010-2022. Note that these wind roses correspond to clear-sun conditions as only observations coincident with AERONET measurements are considered here.

SZA (°)	$\mathrm{AOD_{550}}$	$\mathbf{SSA_{550}}$	**ff**	$\mathbf{H_{aer}}$ (km)	**RH (%)**	**PWV (cm)**	$\mathbf{O_3}$ (DU)	$\mathbf{O_2}$ (ppmv)	$\mathbf{CO_2}$ (ppmv)	α
61.71	0.13	0.93	0.72	2	55	1.46	341	209 000	407	0.15

Table S1. Mean values observed in clear-sky conditions over the period 2010-2022 of the input parameters used for the sensitivity analysis of Section 2.4.2 based on SOLARTDECO simulations.